INAUGURAL - DISSERTATION

submitted to the
Combined Faculties for the Natural Sciences and
for Mathematics
of the Ruperto-Carola University of Heidelberg,
Germany
for the degree of
Doctor of Natural Sciences

put forward by
Dipl.-Phys. Sebastian Domsch
born in Halle (Saale)

Oral Examination: 19th of June 2013

Functional Magnetic Resonance Imaging at High Spatiotemporal Resolution using EPI Combined with Different k-Space Undersampling Techniques at 3 Tesla

Referees: Prof. Dr. Lothar Rudi Schad

Prof. Dr. Wolfgang Schlegel

Funktionelle Magnetresonanztomographie bei Hoher Räumlicher und Zeitlicher Auflösung bei Verwendung von EPI Kombiniert mit Verschiedenen k-Raum Unterabtastungstechniken bei 3 Tesla

Große Nachteile der in der funktionellen Magnetresonanztomographie (fMRT) häufig verwendeten echoplanaren Bildgebungssequenz (EPI) sind die niedrige räumliche Spezifität aufgrund von Verschmierungsartefakten und Verzerrungen, sowie Signalauslöschungen in Bereichen hoher Suszeptibilitätssprünge wie z.B im Orbitofrontalen Cortex (OFC). Im Gegensatz dazu ermöglichen segmentierte EPI Techniken extrem hohe räumliche Auflösungen bei jedoch schlechter Zeitauflösung. In dieser Arbeit wurde eine optimierte EPI Sequenz mit schichtabhängiger Echozeit entwickelt, wodurch Signalauslöschungen im OFC in 50 % aller Probanden einer fMRT Studie (N = 12) im Vergleich zu einer standard EPI Sequenz vermieden wurden. Die durchschnittliche Anzahl von aktivierten Voxeln im OFC wurde dabei um den Faktor 6.3 erhöht. Desweiteren wurde zum ersten mal gezeigt, dass die räumliche Spezifität in EPI fMRT bei 3 T deutlich verbessert werden kann, indem die Matrixgröße in Kombination mit dem Beschleunigungsfaktor einer parallelen Bildgebungstechnik über konventionelle EPI Parametereinstellungen hinaus erhöht wird. Bei Verwendung des vorgestellten hochauflösenen imVergleich zu einem standard EPI Protokoll, zeigte die Gruppenanalyse einer Fingertapping-Studie (N = 6) und einer komplexen Motivations-Studie (N = 15) robuste und deutlich weniger verwischte Aktivierung im Sensomotorischen Kortex (SMC) bzw. im Nucleus Accumbens (NAcc). Die Anzahl der unterscheidbaren aktivierten Cluster im SMC und im Nacc wurden dabei um den Faktor 2.7 bzw. 1.4 erhöht. Um fMRT bei extrem hoher räumlicher und hoher zeitlicher Auflösung durchführen zu können, wurde eine segmentierte EPI Sequenz mithilfe der sog. UNFOLD Technik effektiv beschleunigt (R = 8). Durch Optimierung der Messsequenz und der Datennachverarbeitung konnte bei guter Volumenabdeckung robuste neuronale Aktivierung bei einer Auflösung von 0.7 x 0.7 mm^2 detektiert werden. Nicht zuletzt wird eine neue Filterstrategie vorgestellt, mit der zeitliche Kohärenzen in UNFOLD-Datensätzen minimiert, und so die Detektierbarkeit neuronaler Aktivierung verbessert werden kann. In einer fMRT Studie (N = 5) wurde durch Verwendung des vorgestellten Filters im Vergleich zu einem standard Filter die Anzahl der aktivierten Voxel im SMC um einen Faktor von bis zu 1.4 erhöht.

Functional Magnetic Resonance Imaging at High Spatiotemporal Resolution using EPI Combined with Different k-Space Undersampling Techniques at 3 Tesla

In functional magnetic resonance imaging (fMRI), major drawbacks of the commonly used echo-planar imaging (EPI) sequence are limited spatial specificity due to blurring and distortions as well as signal cancellation in areas affected by susceptibility gradients, such as the orbitofrontal cortex (OFC). In contrast, segmented EPI techniques facilitate ultra-high spatial but low temporal resolution. In this work, an EPI sequence with optimized slice-dependent echo time was developed avoiding signal drop outs in the OFC in 50 % of all subjects during fMRI (N = 12) compared to a standard EPI sequence. The average number of activated voxels detected in the OFC was thereby increased by a factor of 6.3. It was further shown for the first time that the spatial specificity in EPI fMRI at 3 T can be improved by increasing the matrix size in combination with the parallel imaging factor beyond conventional EPI parameter settings. By using the proposed high-resolution compared to a standard EPI protocol, the multi-subject analysis of a simple fingertapping task (N = 6) and a sophisticated motivation task (N = 15) showed robust and clearly less blurred activation in the sensorimotor cortex (SMC) and in the nucleus accumbens (NAcc), respectively. The number of separable clusters detected in the SMC and in the NAcc was thereby increased by a factor of 2.7 and 1.4, respectively. In order to perform fMRI at ultra-high spatial and high temporal resolution, a segmented EPI sequence was highly accelerated (R = 8) with the so-called UNFOLD technique. Both, the MR sequence and data post-processing were optimized facilitating the robust detection of neuronal activation at 0.7 x 0.7 mm^2 resolution and half-brain coverage. Last but not least, a novel filtering strategy is proposed minimizing temporal coherences in UNFOLD datasets and thus improving the detectability of neuronal activation. By using the proposed filter compared to a standard filter, the number of activated voxels detected in the SMC (N = 5) was increased up to a factor of 1.4.

To my father.

List of Abbreviations

ACF ..... Autocorrelation Function

AC-PC ..... Anterior and Posterior Commissure

AR(1) Model ..... Autoregressive Model of First Order

BOLD ..... Blood Oxygenation Level Dependent

BS ..... BOLD Sensitivity

EPI ..... Echo Planar Imaging

fMRI ..... Functional Magnetic Resonance Imaging

FOV ..... Field of View

GLM ..... General Linear Model

G_{sp} ..... Susceptibility Gradients in Phase Encoding Direction

G_{ss} ..... Susceptibility Gradients in Slice Direction

HRF ..... Hemodynamic Response Function

NAcc ..... Nucleus Accumbens

OFC ..... Orbitofrontal Cortex

PE ..... Phase Encoding

PI ..... Parallel Imaging

PSF ..... Point-Spread Function

RO ..... Read Out

SMC ..... Sensorimotor Cortex

TE ..... Echo Time

UNFOLD ..... Unaliasing by Fourier-Encoding the Overlaps using the Temp. Dimension

List of Figures

List of Tables

Introduction

In the past two decades, since the discovery of the blood-oxygenation level dependent (BOLD) effect (Ogawa et al., 1990a; Ogawa et al., 1990b) associated with changes of the magnetic property of blood, functional magnetic resonance imaging (fMRI) has become a widely-used non-invasive imaging technique capable of detecting neuronal activation and providing valuable insights into functionality of the human brain. FMRI enables studying the examination of the primary cortices or the analysis of complex cognitive processes. Today, fMRI is not only used in cognitive neurosciences but also in surgical therapy planning (Vlieger, et al. 2004) and preclinical studies (Marota, et al. 2000). A great advantage of fMRI in contrast to alternative functional imaging modalities such as positron-emission-tomography (PET) and single-photon emission-computed-tomography (SPECT) is that no hazardous radioactive isotopes are applied. Furthermore, fMRI provides higher spatial resolution than electro-encephalography (EEG) or magneto-encephalography (MEG) and higher temporal resolution than PET or SPECT allowing the measurement of fast signal fluctuations of neuronal responses.

Early fMRI focused on isolated brain areas such as the primary sensorimotor cortex (SMC) or the visual cortex which were activated using simple *blocked designed*[1] paradigms applying repetitive stimuli. Modern neurosciences also focus on complex brain networks as the reward-system involved in cognitive processes like decision-making and reward processing (Diekhof, et al. 2008) using sophisticated *event-related*[2] paradigms applying short random stimuli. The detection of fast signal modulations of neuronal activity evoked by short stimuli requires fast imaging techniques (Golay, et al. 2000). High spatial coverage is also required since brain networks as the reward-system extent over several slices (Benson, et al. 1999; Linke, et al. 2010; Muller, et al. 2002). A commonly used rapid imaging technique in fMRI that combines high temporal resolution with spatial coverage in 2-3 s per imaging volume is the single-shot gradient-echo echo planar imaging (EPI) technique (Mansfield 1977).

[1] In blocked design fMRI experiments, a task-related cognitive engagement is maintained during alternating conditions. Long stimuli of several seconds are presented periodically in time.

[2] In event-related fMRI experiments, short stimuli are presented randomly or periodically in time.

However, there are two major drawbacks using EPI. Firstly, EPI is prone to signal loss and image distortions in brain areas such as the orbitofrontal cortex (OFC) (Czervionke, et al. 1988) and the amygdale (Stocker, et al. 2006) as they are close to air/bone and air/tissue interfaces affected by macroscopic susceptibility gradients. Secondly, the comparably long signal read out leads to blurring and ghosting artifacts (Fellner, et al. 2009; Heiler, et al. 2010) limiting the spatial resolution to approximately 2-3 mm. Segmented EPI techniques with a sub-millimeter resolution have been developed (Barth, et al. 1999; Frahm, et al. 1993; Hoogenraad, et al. 1999; Hoogenraad, et al. 2000) to facilitate the investigation of fine scale retinotopic and somatotopic organization in the visual system and the sensorimotor system, respectively (Engel, et al. 1997; Grill-Spector, et al. 2004; Kleinschmidt, et al. 1997). Nevertheless, without modifications, the temporal resolution or spatial coverage of such segmented EPI techniques is too low to be applicable for sophisticated event-related fMRI studies.

The OFC is part of the above mentioned reward-system and is thus in the focus of modern neuroscience studies. In the first part of this thesis, a strategy was developed to reduce EPI signal loss and to increase the BOLD sensitivity in the OFC. Furthermore, the BOLD spatial specificity was considerably improved without sacrificing temporal resolution by using parallel imaging (Griswold, et al. 2002). In the second part of this work, a high-resolution segmented EPI sequence was developed and highly accelerated with the UNFOLD method (Madore, et al. 1999) to enable fMRI at sub-millimeter spatial and high temporal resolution. Finally, a novel temporal filtering strategy is proposed to remove autocorrelations inherent to the UNFOLD method and thus to improve statistical inference in fMRI.

Sophisticated strategies have been proposed to compensate for detrimental susceptibility effects in fMRI. These methods include z-shimming (Constable and Spencer 1999; Frahm, et al. 1988; Ordridge, et al. 1994), tailored excitation pulses (Cho and Ro 1992; Konstandin, et al. 2011; Stenger, et al. 2000) or spiral read out trajectories (Glover 1999a; Nagel, et al. 2009; Preston, et al. 2004) requiring either considerably modifications of the pulse sequences and post-processing routines or compromising spatial or temporal resolution. A practical alternative is the optimization of the echo time, since BOLD sensitivity depends critically on this sequence parameter particularly in subcortical brain areas such as the amygdale and the OFC affected by strong susceptibility gradients (Deichmann, et al. 2002). More robust activation in both brain areas has been observed in many previous whole-brain fMRI studies using an EPI sequence with a re-

duced echo time of 27 ms (Cools, et al. 2002; Evers, et al. 2005; Morawetz, et al. 2008). However, the OFC extends over several slices and each slice is affected by susceptibility gradients of different magnitude. At a field strength of 1.5 T, Stoecker and colleagues (2006) showed that an EPI sequence with slice-dependent echo times improved signal detection in the amygdale. By using slice-dependent echo times, the temporal resolution is unaffected, which is particularly important for event-related studies. In this work, a modified EPI sequence with slice-dependent echo times was developed to increase the BOLD sensitivity in the OFC and to translate the significant results to the clinical field strength of 3 T.

High spatial specificity is required to study small brain structures with a dimension of only a few millimeters such as the amygdala, which is composed of 13 different nuclei, or the nucleus accumbens (NAcc), a subregion of the ventral striatum, which can be divided into the NAcc shell and the NAcc core. Both brain areas are associated with reward-learning (Diekhof, et al. 2008; Knutson, et al. 2001) and drug addiction (Diekhof, et al. 2008; Vollstadt-Klein, et al. 2010) and are therefore of great importance for cognitive neuroscience. Segmented EPI techniques (Voit and Frahm 2005) use multiple radiofrequency (RF)-excitations during signal acquisition to keep the read out short and to facilitate improved spatial specificity and reduced artifacts at the expense of temporal resolution. Segmented EPI techniques have been successfully used to study fine-scale functional processing e.g. in the human SMC or in the visual system (Heiler, et al. 2010; Kleinschmidt, et al. 1997; Schweizer, et al. 2008). However, due to the lack of temporal resolution commonly used segmented EPI techniques are not capable of detecting transient BOLD signal modulations in event-related fMRI studies. Parallel imaging (PI) (Griswold, et al. 2002; Pruessmann, et al. 1999; Sodickson, et al. 1999; Sodickson and Manning 1997) was proposed to accelerate the image acquisition by exploiting spatial information of multiple receiver coils. This enables improved spatial resolution in EPI without compromising temporal resolution. Recently, it has been shown that the spatial specificity in fMRI can be improved by both, either increasing the PI-factor (R) to reduce blurring or by increasing the matrix size to reduce geometric distortions (Fellner, et al. 2009; Preibisch, et al. 2003). It is hypothesized that BOLD spatial specificity could be further improved by increasing both, the matrix size and the PI-factor simultaneously. However, small BOLD signal changes in the dimension of 5 % require a sufficient signal-to-noise ratio (*SNR*) for robust detection. Therefore, the decreased *SNR* caused by small voxel sizes and high PI-factors compromises BOLD sensitivity. To avoid insufficient *SNR* and thus low BOLD sensitivity, most fMRI studies using in-

creased EPI matrix sizes (e.g. 192 x 192) combined with high PI-factors (e.g. $R > 3$) have been performed only at ultra-high fields (> 3 T) (Moeller, et al. 2006; Moeller, et al. 2010; Speck, et al. 2008) yielding higher *SNR* and therefore improved PI performance (de Zwart, et al. 2004). However, the usage of large matrix sizes at commonly available 3 T scanners is not well established. In this work, the goal was to investigate the feasibility of fMRI at high spatial specificity using EPI with large matrix sizes in combination with high PI-factors.

Due to the natural trade-off between spatial and temporal resolution, a major challenge for fMRI at high spatial resolution is limited temporal resolution. However, high temporal resolution is required to detect transient BOLD signal modulations especially in event-related fMRI studies (Josephs, et al. 1997). The UNFOLD method (Madore, et al. 1999) has been proposed to accelerate image acquisition speed in cardiac imaging and fMRI. Recently, high-resolution fMRI at 1.5 x 1.5 mm^2 voxel size has been successfully performed using a 3D-spiral sequence accelerated with UNFOLD (Law and Glover 2009). In this work, rapid fMRI at sub-millimeter resolution is demonstrated by combining the UNFOLD method with a high-resolution segmented EPI sequence. The feasibility of this technique was validated in an event-related fingertapping experiment.

Using UNFOLD, the interleaved sampling of the so-called *k*-space (see Section 1.2.2) leads to spatial aliasing that creates disruptive peaks in the temporal signal power spectrum. The number of aliasing peaks increases with the UNFOLD acceleration factor. As long as these aliasing peaks are spectrally separable from the activation peaks, the fMRI signal can be regularly analyzed in the time domain after the aliasing peaks have been removed by temporal filtering. In many fMRI studies the time intervals between consecutive stimuli are fixed. In this case the signal energy of neuronal activation is captured in only very few spectral peaks (i.e. the basic frequency and the first and second harmonics) potentially allowing for high UNFOLD acceleration factors. The fact that the width of the aliasing peaks is not infinitely small naturally limits the acceleration capacity of the UNFOLD method. As proposed by Hu and colleagues (2011), the efficiency of UNFOLD can be increased by removing phase trends from the complex MR signal effectively narrowing the aliasing peak-width. Nonetheless, high UNFOLD acceleration requires numerous aliasing frequencies to be removed from the fMRI signal before statistical modeling can be carried out in the time domain. Previous papers have suggested either low-pass filtering (Afacan, et al. 2009; Hu and Glover 2009; Law and Glover 2009) or simple multiband filtering (Madore, et al. 1999) by setting the aliasing peaks to zero. Both strategies are inappropriate at higher UNFOLD factors. Low-pass

filtering significantly decreases temporal resolution and potentially removes signal contributions related to neuronal activation. Multiband filtering leads to autocorrelated (non-white) noise, that severely biases statistical modeling of fMRI data (Smith, et al. 2007). Common non-white noise sources are temperature changes, scanner drifts and aliased physiological fluctuations (e.g. cardiac pulsations, breathing) or unmodelled neuronal noise sources. In general, there are two different approaches dealing with the issue of non-white noise. The first approach, often referred to as “coloring”, replaces the intrinsic autocorrelation with the known autocorrelation introduced by band-pass filtering (Friston, et al. 1995; Worsley and Friston 1995). An alternative approach is to “prewhiten” the data before fitting the General Linear Model (GLM) parameters using a temporal smoothing filter (Woolrich, et al. 2001). To create this filter, an autoregressive model of first order (AR(1) model) (Bullmore, et al. 1996) or a 1/f model (Aguirre, et al. 1997; Zarahn, et al. 1997) is commonly employed. For both approaches to perform well, the noise must be dominated by low frequencies. However, this condition is met in most fMRI studies but not in UNFOLD datasets since the aliasing peaks are spread over the whole frequency range. In this work, a novel filtering technique was developed to overcome these drawbacks and to reduce auto-correlated noise in order to decrease false-positives and to improve statistical inference in UNFOLD fMRI.

1 Background

In 1891, Michelson discovered the hyperfine structure of atoms caused by the interaction between the magnetic moment of the nucleus and the orbital electrons. In 1938, Isidor Rabi verified the existence of a magnetic moment of atomic nuclei, which was the foundation for (*Nuclear*) *Magnetic Resonance* (NMR). The focus in this section is on the magnetic moment of protons, the only nucleus used for imaging throughout this work. A general description of the basics of NMR can be found in Abragam (1961).

1.1 Nuclear Spin and Magnetic Moment

Those nuclei with an odd number of protons and/or neutrons posses a non-zero spin I (Haken and Wolf 2003). In quantum mechanics, the nuclear spin can be expresses by the operator $\hat{I}$ satisfying the commutator relation

$$\left[\hat{I}_i, \hat{I}_j\right] = i\hbar\varepsilon_{ijk}\hat{I}_k \ , \qquad 1.1$$

where the indices *i*, *j*, *k* are the space coordinates and with ε_{ijk} being the *Levi-Civita* symbol. From Eq. 1.1 follows that the square angular momentum $\hat{I}^2$ commutes with $\hat{I}_z$ (i.e. *z*-component of $\hat{I}$). Therefore, $\hat{I}^2$ and $\hat{I}_z$ have the same eigenstates, $|I,m\rangle$, which form a complete basis and are uniquely determined by the spin quantum numbers I and m. The eigenequations for $\hat{I}^2$ and $\hat{I}_z$ are:

$$\hat{I}^2 \,|\, I,m\rangle = \hbar^2 \cdot I\left(I+1\right)|\, I,m\rangle \qquad \text{with } I = 0,\ 1/2,\ 1,\ 3/2,\ \ldots \qquad 1.2$$

$$\hat{I}_z \,|\, I,m\rangle = \hbar \cdot m \,|\, I,m\rangle \qquad \text{with } m = -I\ ,\ I+1,\ \ldots,\ I-1,\ I \qquad 1.3$$

The spin quantum number for the hydrogen atom ^{1}H is $I = ½$. For nuclei with a non-zero spin, the magnetic moment $\hat{\mu}$ associated with the spin $\hat{I}$ is:

$$\hat{\mu} = \gamma \cdot \hat{I} \qquad 1.4$$

For the hydrogen nucleus ^{1}H, the gyromagnetic ratio γ is 42.6 MHz/T.

1.1.1 Nuclear Spin in an External Magnetic Field

The magnetic spin Hamiltonian $\hat{H}^{mag}$, with

$$\hat{H}^{mag} = -\hat{\mu}\vec{B} = -\gamma\hat{I}\vec{B} \quad , \tag{1.5}$$

describes the interaction between a magnetic moment $\hat{\mu}$ with the external magnetic field $\vec{B}$. In case of a constant magnetic field oriented e.g. along the z-direction, $\vec{B} = (0, 0, B_0)$, Eq. 1.5 simplifies to:

$$\hat{H}^{mag} = -\gamma\hat{I}_z B_0 \tag{1.6}$$

The Hamiltonian $\hat{H}^{mag}$ commutes with $\hat{I}^2$ and $\hat{I}_z$ and has therefore the same eigenstates $|I, m\rangle$. The energy eigenvalues E_m can be calculated by the eigenequation Eq. 1.3:

$$\hat{H}^{mag} \,|\, I, m\rangle = E_m \,|\, I, m\rangle \tag{1.7}$$

$$E_m = -\gamma\hbar m B_0 \tag{1.8}$$

The external magnetic field causes a splitting of the energy levels which is called the Zeeman effect. The proton (I = ½, m = ± ½), has two eigenstates with the energy difference ΔE_m:

$$\Delta E_m = E_{-1/2} - E_{+1/2} = \gamma\hbar B_0 = \hbar\upsilon_0 \tag{1.9}$$

The frequency $\upsilon_0 = \gamma B_0$ is referred to as *Larmor frequency*. At a field strength of B_0 = 3 T, the *Larmor frequency* of a proton is $\upsilon_0 \approx 128$ MHz.

1.1.2 Macroscopic Magnetization

In NMR experiments, a sample is placed in an external magnetic field B_0. The observable magnetization is the coherent sum of the magnetic dipole moments of all spins in the sample. Assuming a fixed number of spins N and a constant temperature T, this thermodynamic system of fermions (particles with half-integral spin) can be considered as a *canonical ensemble* that can absorb and release energy from and, respectively, to the environment. At room temperature of $T = 293\ K$, the energy difference $\Delta E_m = \hbar\omega_0$ of the two different Zeeman states is much less than the thermal energy $k_B T$. Therefore, the *Fermi statistics*, which describes the occupation probability P_m of the different energy level E_m, can be approximated by the *Maxwell-Boltzmann statistics*:

$$P_m = \frac{e^{-E_m/k_B T}}{Z\left(T, N, B_0\right)} \tag{1.10}$$

Here, the total energy E_m is the sum of the respective energies ε_m^i of each particle and the partition function $Z\left(T, N, B_0\right)$ is defined as the sum over all micro states:

$$E_m = \sum_{i=1\ldots N} \varepsilon_m^i \tag{1.11}$$

$$Z(T, N, B_0) = \sum_{m_1} \cdot \sum_{m_2} \cdots \sum_{m_N} e^{-E_m/k_B T} \tag{1.12}$$

For protons, the effective magnetization M_0 is proportional to the number N of spins and is given by:

$$M_0 = N \sum_{m=\pm 1/2} P_m \left\langle I, m \left| \hat{\mu}_z \right| I, m \right\rangle \tag{1.13}$$

$$= N \cdot \mu_z \cdot \tanh\left(\frac{\hbar\omega_0}{2k_B T}\right) \tag{1.14}$$

At room temperature $\left(\hbar\omega_0 \ll k_B T\right)$, M_0 can be approximated by:

$$M_0 = \frac{N}{V} \frac{I(I+1)\gamma^2\hbar^2}{3k_B T} B_0 \propto \frac{B_0}{T} \tag{1.15}$$

Equation 1.15 shows that at room temperature and a magnetic field strength of $B_0 = 3$ T, only every hundred thousandth proton spin contributes to the magnetization. However, the magnetization can be measured because of the high proton density of $\rho_{1H} \approx 10^{19}/mm^3$ in water.

1.1.3 Bloch-Equations

In quantum mechanics, the dynamic of the magnetization of a spin system can be expressed by the following commutator relation:

$$\frac{d}{dt}\left\langle \hat{M} \right\rangle = \frac{d}{dt} \sum_{i=1\ldots N} \left\langle \hat{\mu}_i \right\rangle = -\frac{i}{\hbar} \sum_{i=1\ldots N} \left\langle \left[\hat{\mu}_i, \hat{H} \right] \right\rangle \tag{1.16}$$

Combining this relation with Eq. 1.1, Eq. 1.4, and Eq. 1.5 leads to:

$$\frac{d}{dt}\vec{M}(t) = \gamma\vec{M}(t)\times\vec{B} \qquad 1.17$$

Hence, if the magnetization $\vec{M}$ is not aligned with the magnetic field $\vec{B}$, then $\vec{M}$ precesses with the *Larmor frequency* $\omega_0 = \gamma B_0$. Neglecting the weak coupling between the nuclear spins with each other and with the surrounding matter, Eq. 1.17 can be derived classically by summing up the torque $\partial\vec{I}/\partial t = \vec{\mu}\times\vec{B}$ produced by the magnetic moment $\vec{\mu}$ and the magnetic field $\vec{B}$ acting on each spin. The Bloch equations were introduced by Bloch in 1949 and consider the interactions between the spins and the environment:

$$\frac{d}{dt}M_x = \gamma\left(\vec{M}\times\vec{B}\right)_x - \frac{M_x}{T_2} \qquad 1.18$$

$$\frac{d}{dt}M_y = \gamma\left(\vec{M}\times\vec{B}\right)_y - \frac{M_y}{T_2} \qquad 1.19$$

$$\frac{d}{dt}M_z = \gamma\left(\vec{M}\times\vec{B}\right)_z - \frac{M_0 - M_z}{T_1} \qquad 1.20$$

It can be seen that the Bloch equations are symmetrically in the *x* and *y*-component because the magnetic field points only along the *z*-direction. By using

$$\vec{M}_\perp(t) = M_x(t) + iM_y(t)\ , \qquad 1.21$$

the Bloch equations can be expressed in the more convenient and compact form:

$$\frac{d}{dt}\vec{M}(t) = \gamma\vec{M}(t)\times\vec{B} + \frac{1}{T_1}\left(M_0 - M_z\right)\vec{e}_z + \frac{1}{T_2}\vec{M}_\perp \qquad 1.22$$

The terms $1/T_1$ and $1/T_2$ describe the relaxation of the longitudinal and the transversal components M_z and $\vec{M}_\perp$, respectively, related to spin-lattice and spin-spin interactions, respectively (see Section 1.1.5).

1.1.4 Excitation of the Magnetization and Signal Acquisition

A sample placed inside the magnetic field B_0 can absorb energy from an alternating electromagnetic field or RF-pulse tipping the magnetization away from its equilibrium state parallel to the main magnetic field. Relaxation effects during the RF-excitation can be neglected because the RF-pulse is irradiated for only a few milliseconds much

shorter than the transversal and the longitudinal relaxation times T_2 and T_1, respectively. The B-field component of the RF-pulse with the frequency ω_1 may be perpendicular to the main magnetic field B_0:

$$\vec{B}_1 = \left(B_1 \cos(\omega_1 t), B_1 \sin(\omega_1 t), 0\right) \quad 1.23$$

The time dependence can be eliminated by a coordinate transformation into a rotating reference frame S':

$$x' = x\cos(\omega_1 t) + y\sin(\omega_1 t) \quad 1.24$$

$$y' = -x\sin(\omega_1 t) + y\cos(\omega_1 t) \quad 1.25$$

$$z' = z \quad 1.26$$

It may be assumed that the z-components of the static reference frame S and the rotating reference frame S' are aligned and that S' rotates synchronously with the B-field vector of the RF-pulse. Then the Bloch´s equation (Eq. 1.22) simplify to:

$$\frac{d}{dt}\vec{M}(t) = \gamma\vec{M}(t)\times\left(B_1, 0, B_0 - \frac{\omega_1}{\gamma}\right) \quad 1.27$$

The main magnetic field B_0 is some orders of magnitude larger than B_1 (i.e. $B_0 >> B_1$). If the RF-pulse is not in resonance (i.e. $\omega_1 \neq \omega_0$), the effective magnetic field $\vec{B}_{eff} = \vec{B}_0 + \vec{B}_1$ is not significantly different from $\vec{B}_0$. Hence, only if the RF-pulse is on-resonant (i.e. $\omega_1 = \omega_0$), then the z-component of $\vec{B}^z_{eff} = \left(B_0 - \omega_1/\gamma\right)$ is zero and the magnetization $\vec{M}(t)$ can be tipped away from its equilibrium position parallel to B_0 by precessing around the x'-axis (Figure 1.1).

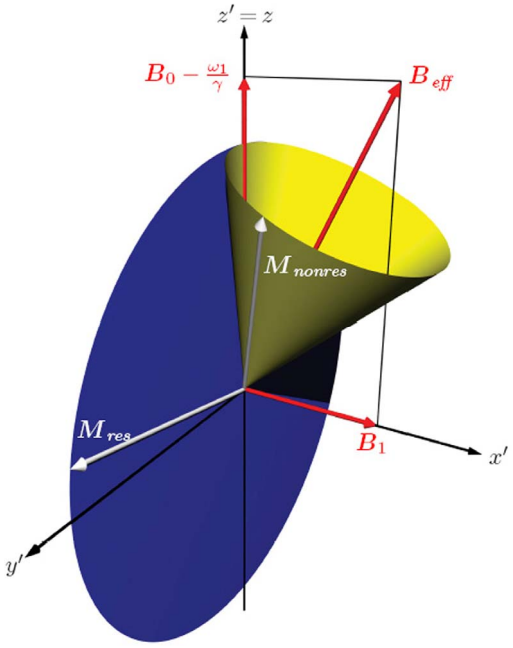

Figure 1.1 – Excitation of the Magnetization using a Temporally Varying Magnetic Field.
Temporal development of the magnetization vector (white) in the rotating reference frame. If the RF-pulse is on resonance (i.e. $\omega_1 = \omega_0$), then the magnetization rotates along the blue disc around B_1. In the non-resonance case, the magnetization vector rotates on the yellow cone around the effective magnetic field B_{eff}. Source: (Schmitter 2008)

In correspondence to the resonance absorption curve of a harmonic oscillator, the width $\Delta\omega$ of the absorption curve is given by $\Delta\omega = 1/T_2$. The rotation angle α is usually referred to as the *flip-angle* and depends on the amplitude B_1 and the duration τ of the RF-pulse:

$$\alpha(\tau) = \gamma \int_0^{\tau} B_1(t) dt \qquad 1.28$$

For signal acquisition, often a π/2-pulse is applied rotating the magnetization vector into the transversal plane. The surface normal of the receiver coil is oriented perpendicular to the static magnetic field B_0. According to Faraday`s law of induction, the precession of the tipped magnetization induces the voltage U_{ind} in the receiver coil:

$$U_{ind} = -\frac{1}{c}\frac{\partial}{\partial t}\int_F \vec{B}(\vec{x},t)d\vec{f} \qquad 1.29$$

The magnitude of the transversal component of the magnetization $M_\perp$ and its phase ϕ is given by the time response of the measuring signal $S(t) \propto U_{ind}$:

$$\Phi(\vec{x},t) \propto \int_0^t \left(\omega(\vec{x},t) - \omega_0\right) dt' \qquad 1.30$$

The signal $S(t)$ is a linear superposition of each spin package in consideration of the phase modulation $e^{i\omega t}$ and the local spin density, proportional to $M_\perp(\vec{x},t_0)$:

$$S(t) \propto e^{i\omega_0 t}\int_V M_\perp(\vec{x},t_0)e^{i\Phi(\vec{x},t)}dV \qquad 1.31$$

In a homogeneous magnetic field, every spin package rotates at the same frequency ω_0 and the frequency distribution of the spin packages $h(\omega)$ can be describes by a *Dirac-Delta function*. With an appropriate variable transformation, Eq. 1.30 can be transformed into an integral over the phases of the spin packages where the signal $S(t)$ is the *Fourier Transform* of the frequency distribution $h(\omega)$:

$$S(t) \propto e^{i\omega_0 t}\int h(\omega)e^{i\omega t}d\omega \qquad 1.32$$

At the boundaries of tissue/tissue and tissue/air interfaces, e.g. in the area of the frontal and the paranasal sinuses, the magnetic field can be extremely inhomogeneous. This severely compromises the signal acquisition in fMRI focussing on limbic and prefrontal brain areas such as the amygdala or the OFC.

1.1.5 Relaxation

According to the Bloch´s equation (Eq. 1.22), the relaxation of the longitudinal and the transversal components of the "excited" magnetization back to the thermal equilibrium state, characterized by the *Maxwell-Boltzmann statistics* (Eq. 1.10), is described by the relaxation rates $1/T_1$ and $1/T_2$, respectively. The relaxation of both components M_z and $M_\perp$ occurs independently.

1.1.5.1 Longitudinal Relaxation

The longitudinal relaxation of a spin system results from energy transfer between the spin system and the surrounding reservoir resulting in the state of minimal energy, the thermal equilibrium state. *Brownian motion* of the molecules produces magnetic field fluctuations which act like small RF-pulses with the spectral energy distribution $J(\omega)$. The spin-system can give energy to the reservoir most efficiently in the case of resonance (i.e. $\omega = \omega_0$). The transition rate and therefore also the T_1-relaxation time depends on the width of the distribution $J(\omega)$ at $\omega = \omega_0$. According to the Bloch equation (Eq. 1.22), the longitudinal relaxation of the inverted magnetization is given by

$$M_z(t) = M_0\left(1 - 2e^{-t/T_1}\right), \tag{1.33}$$

with $M_z(0) = -M_0$ (Figure 1.2 (a)).

1.1.5.2 Transversal Relaxation

After the magnetization has been deflected from its equilibrium state, the phases of all spin packages are initially in coherence, a state of minimal entropy. Dipole-dipole interactions between spins cause random field fluctuations, even if the main magnetic field B_0 is perfectly homogeneous. Hence, the spin packages precess at different rates, the phase coherence will be destroyed, and the entropy increases. The frequency distribution of the spin packages is in this case a *Lorentz distribution* (1961) and according to Eq. 1.32, the signal decays exponentially, referred to as T_2-decay (Figure 1.2 (b)):

$$M_\perp(t) = M_\perp(t_0)\, e^{i\omega_0 t} e^{-t/T_2} \tag{1.34}$$

According to Eq. 1.22, in the case of magnetic field inhomogeneities $\Delta B(\vec{x})$, the precession rate is given by:

$$\omega = \omega_0 + \gamma \Delta B(\vec{x}) \tag{1.35}$$

If the field strength changes on microscopic scales, then the frequency distribution of the spin packages are Lorentz distributed and an exponential T_2'-decay is superimposed on the T_2-decay, referred to as T_2*-decay. In the rotating reference frame, the transversal magnetization is thus given by:

$$M_{\perp}(t) = M_{\perp}(t_0) \cdot e^{-t/T_2^*} \tag{1.36}$$

The effective relaxation rate $1/T_2$* is given by

$$\frac{1}{T_2^*} = \frac{1}{T_2} + \frac{1}{T_2'} \tag{1.37}$$

and increases with the magnetic field inhomogeneities:

$$\frac{1}{T_2'} = \gamma \cdot \Delta B \tag{1.38}$$

The relaxation times T_1 and T_2 are tissue dependent (Table 1.1) and, for imaging, they can be used as contrast parameters.

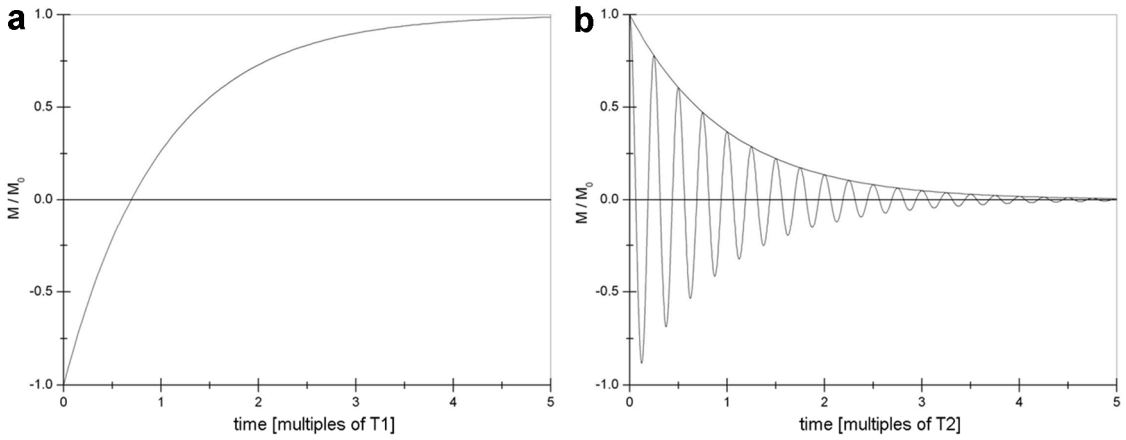

Figure 1.2 – Longitudinal and Transversal Relaxation.
*(**a**) Relaxation of the longitudinal magnetization component M_z in units of the relaxation time T_1. (**b**) Free induction decay (i.e. voltage induced in the receiver coil) showing the relaxation of the real part of the transversal magnetization component $M_{\perp}$ in units of the relaxation time T_2. In a perfect homogeneous main magnetic field, the envelope decays exponentially. Source: (Schmitter 2008)*

Tissue type	T_1 [ms]	T_2 [ms]	T_2/T_1
Gray matter	950	100	0,11
White matter	600	80	1,33
Blood	1200	100-200	0,09-0,17
Fat	250	60	0,24
Liquor	4500	2200	0,49
Muscle	900	50	0,06

Table 1.1 – T_1 and T_2-Relaxation Times of Different Tissue Types at 1.5 T.
Source: (Blueml, et al. 1993)

1.1.6 Spin Echo

If the magnetization is tipped into the transversal plane at time t_0, then the spin packages dephase in the course of time due to T_2*-decay. Those spin packages which only "see" the main magnetic field B_0 are resting with respect to the *x'*-axis of the reference frame *S'* rotating at the frequency ω_0 (see Section 1.1.4). All other spin packages affected by a field offset $\Delta B(\vec{x})$ (i.e. $B^{loc}(\vec{x}) = B_0 + \Delta B(\vec{x})$) are precessing faster or slower depending on the sign and the amplitude of the extra field (Figure 1.3). By applying a π-pulse or *refocusing pulse* at time *TE*/2, the magnetization vectors of the spin packages are mirrored at the *x'*-axis of the rotating reference system *S'*. Thus, the phases accumulated up to the moment of the refocusing pulse at *TE*/2 change their signs. In case the field offset $\Delta B(\vec{x})$ is stationary and the spin packages have not moved within the time span *TE*/2, then the precession frequencies remain constant. Accordingly, all spin packages are in phase at *TE* creating a so-called spin-echo (Hahn 1950). In areas compromises by magnetic field offsets due to strong susceptibility differences, the spin-echo technique enables the detection of NMR signals which are only affected by the T_2-decay. However, the application of refocusing pulses compromises temporal resolution and deposits energy in form of heat in the tissue.

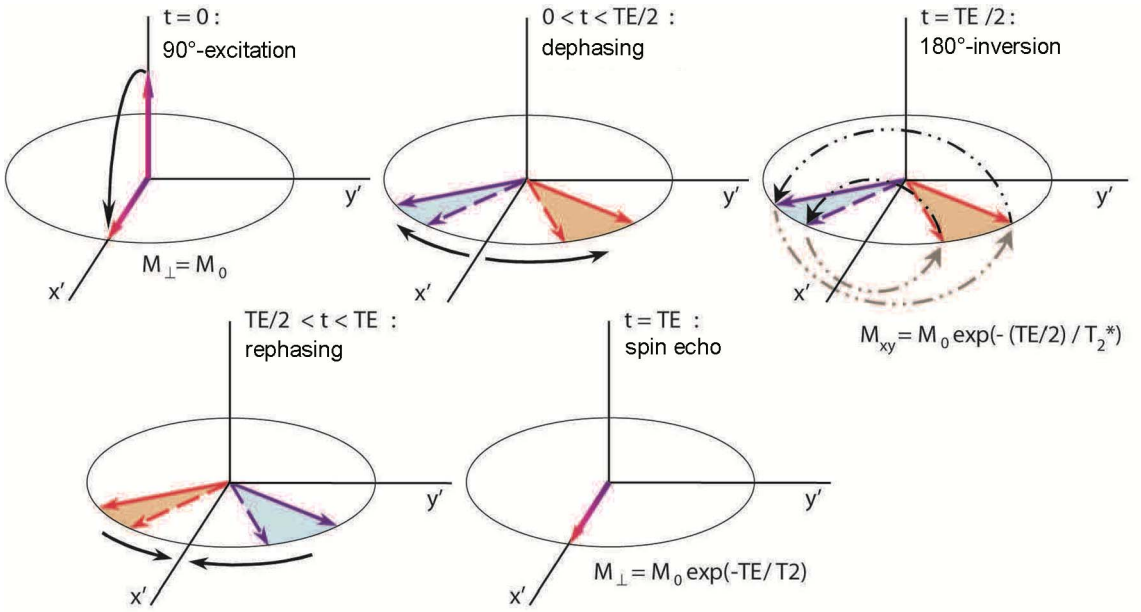

Figure 1.3 – Formation of a Spin-Echo using a 180°-Refocusing Pulse.
Adopted from (Schmitter 2008).

1.1.7 Gradient Echo

Without a refocusing pulse, a so-called gradient-echo can be generated using a combination of dephasing and rephasing gradients $\pm G_x$ (Figure 1.4). These gradients are usually constant and oriented, w.l.o.g., along the *x*-direction:

$$G_x = \frac{dB_z(x)}{dx} \equiv const \qquad 1.39$$

Applying such a dephasing gradient, the precession frequency of the spin packages depends on their *x*-position:

$$\omega(x) = \omega_0 + \gamma G_x x \qquad 1.40$$

After a time period of *TE*/2, the polarity of the dephasing gradient G_x is changed while the magnitude remains constant. Hence, after an additional time period of *TE*/2, the spin packages are refocused (i.e. $\Delta\Phi = 0$) at the time point *TE*:

$$\Delta\Phi(TE) = \gamma \cdot \int_0^{TE} G_x(t)dt = 0 \qquad 1.41$$

A gradient-echo can be generated much faster than a spin-echo because no additional refocusing pulse is applied. Therefore, gradient-echoes are used if fast imaging is required. However, the signal at the gradient-echo is weak compared to the spin echo signal particularly in areas affected by strong susceptibility differences with short T_2*.

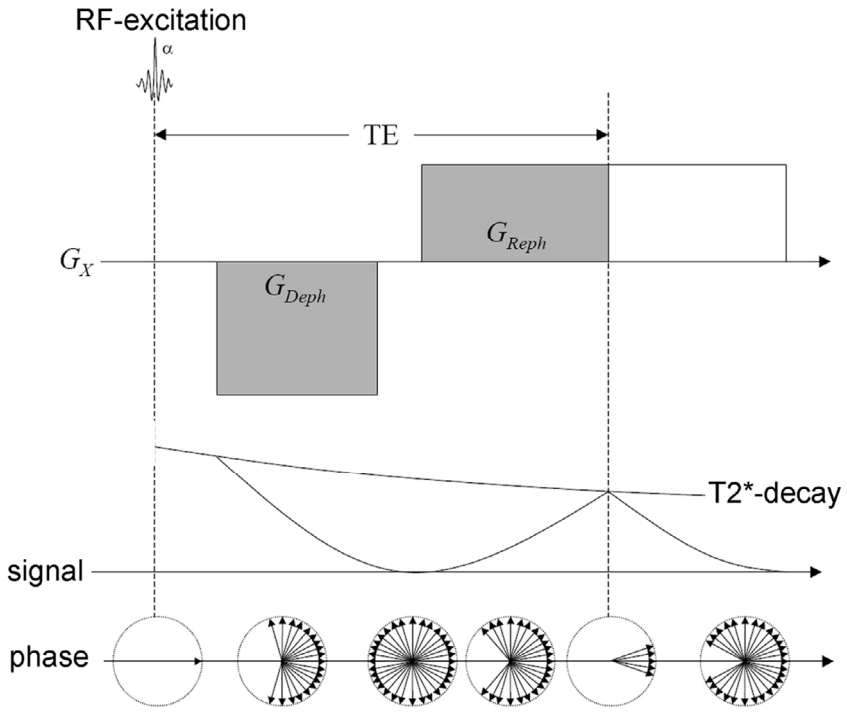

Figure 1.4 – Formation of a Gradient-Echo using Two Gradients with Opposite Polarity.
Adopted from (Kroll 2004).

1.2 Magnetic Resonance Imaging

The cornerstone of magnetic resonance imaging (MRI) was laid by Lauterbur and Mansfield (1973). Their technique used gradient fields for spatially encoding of the MR signal for which they received the Nobel Prize in Medicine in 2003. Using this technique, the spatial information of the spin magnetization can be recovered using a Fast

Fourier Transformation (*FFT*). Principally, imaging can be performed in 2D exciting single slices or in 3D exciting a whole slab of the sample volume.

1.2.1 Slice Selective Excitation

By superimposing an additional gradient field G_z, w.l.o.g. in *z*-direction, onto the main magnetic field B_0, the precession frequency of a spin package depends on the amplitude of the gradient field and on the *z*-coordinate:

$$\omega(z) = \gamma\left(B_0 + G_z z\right) \tag{1.42}$$

Thus, the RF-pulse $\vec{B}_1(t) = B_1 \cos(\omega_1 t)$ with frequency ω_1 excites only those spin packages at the location *z*, whose precession frequency $\omega(z)$ match the RF-pulse frequency ω_{RF}. According to the Bloch equations (Eq. 1.22), the slice profile at time T is the Fourier transform of the RF-excitation pulse $B_1(t)$:

$$M_\perp(z,T) = i\gamma M_0 e^{i\gamma G_z T} \int_0^T B_1(t) e^{i\gamma G_z z \cdot t} dt \tag{1.43}$$

This relation is valid only for small flip-angles, linear gradients G_z, and further neglects relaxation effects during the RF-excitation. From Eq. 1.43 can be seen that the slice profile is the Fourier transform of the RF-pulse. For the excitation of rectangular slices, ideally sinc-shaped RF-pulses of infinite duration would be required. However, due to limited pulse duration, the slice profiles are not perfectly rectangular. From Eq. 1.43 follows that the slice-thickness Δz decreases for stronger slice selecting gradients G_z and longer pulse durations τ:

$$\Delta z = \frac{4\pi}{\gamma G_z \tau} \tag{1.44}$$

1.2.2 Spatial Encoding and *k*-Space Concept

After the slice selective excitation, gradients G_x in *x*-direction (frequency encoding) and G_y in *y*-direction (phase encoding) are used to encode the remaining degrees of freedom. Every spin package has then a position dependent phase:

$$\Phi(x,y,t) = \gamma \int_0^t (B_0 + G_x x + G_y y) dt' \qquad 1.45$$

If the position of the spin packages is not time dependent (resting spins) and by defining a wave vector $\vec{k}$, with

$$\vec{k} = \gamma \int_o^{t^{acq}} \vec{G}(t) dt \quad , \qquad 1.46$$

then the signal intensity can be written as the Fourier transform of the local spin density $M_\perp(\vec{x})$, according to Eq. 1.31.

$$S(\vec{k}) \propto \int M_\perp(\vec{x}) \cdot e^{-i\cdot\vec{k}\cdot\vec{x}} dx^3 \qquad 1.47$$

Hence, the spin density $M_\perp(\vec{x})$ is the inverse Fourier transform of the measured signal intensity $S(\vec{k})$:

$$M_\perp(\vec{x}) \propto \int S(\vec{k}) \cdot e^{i\cdot\vec{k}\cdot\vec{x}} dk^3 \qquad 1.48$$

The wave vector $\vec{k}$ introduced in Eq. 1.46 defines the *k*-space, in which the raw data is acquired. In order to sample the *k*-space data, the gradient amplitude $|\vec{G}|$ is varied during data acquisition. The succession of gradient fields, RF-pulses, and data sampling is referred to as pulse sequence or imaging sequence. The entire *k*-space data points yield a hologram being convertible into a tomogram in position space by a *FFT*. The *FFT*-algorithm is much faster than the Fourier transform but requires that the collected *k*-space data points are equally spaced. During signal acquisition, the amplitude of the frequency encoding gradient G_x is usually fixed while the data is being acquired in constant time intervals. The amplitude of the phase encoding gradient G_y is thereby varied in usually equidistant steps while the duration of the gradient is fixed. Generally, the *k*-space can be sampled with arbitrary trajectories whereby this requires gridding of the *k*-space data onto a Cartesian grid before the *FFT* can be applied.

1.2.3 Data Sampling and Image Reconstruction

In MRI, the object $M_\perp(x)$ is sampled in *k*-space which is truncated and discretized due to finite sampling rates and measurement times. The *k*-space signal $m_\perp(k) = FFT(M_\perp(x))$ of the imaging object is sampled in N discrete steps with a step

size Δk. This can be described by multiplication of $m_{\perp}(k)$ with a sampling function $SF(k)$:

$$s_{\perp}(k) = m_{\perp}(k) \cdot SF(k) \tag{1.49}$$

The sampling function $SF(k)$ is given by the product of the Comb-Function (a.k.a. Shah-Function) $c(k)$ and a rectangular window $\text{rect}(k)$ expressing discrete sampling and truncation, respectively.

$$SF(k) = c(k) \cdot \text{rect}(k) \tag{1.50}$$

The Comb-Function $c(k)$ is defined as equidistant delta functions with amplitude one and the period Δk (Bracewell 1999):

$$c(k) \equiv \Delta k \sum_{-\infty}^{+\infty} \delta(k - n\Delta k) \tag{1.51}$$

The truncation can be described as a window function:

$$\text{rect}\left(\frac{k + 1/2 \cdot \Delta k}{N \cdot \Delta k}\right) = \begin{cases} 1 & \text{if } -N\Delta k/2 \le k \le N\Delta k/2 \\ 0 & \text{else} \end{cases} \tag{1.52}$$

In the image domain, the measured signal $S_{\perp}(x)$ of the "true" object $M_{\perp}(x)$ is the inverse Fourier transform of the measured *k*-space signal, $s_{\perp}(k)$. According to the convolution theorem, the displayed image $S_{\perp}(x)$ can be expressed as the convolution of the object $M_{\perp}(x)$ with the Fourier Transform of the Comb function and the Fourier Transform of the window function (Figure 1.5):

$$S_{\perp}(x) = M_{\perp}(x) \otimes C(x) \otimes N \cdot \Delta k \cdot \text{sinc}(\pi N \Delta k \cdot x) \tag{1.53}$$

The Fourier transform of the Comb function is also a Comb function:

$$C(x) = \Delta k \sum_{n=-\infty}^{n=+\infty} \int \delta(k - n\Delta k) e^{2\pi i \cdot k \cdot x} \quad 1.54$$

$$= \Delta k \sum_{n=-\infty}^{n=+\infty} e^{2\pi i \cdot n \cdot \Delta k \cdot x} \quad 1.55$$

$$= \sum_{n=-\infty}^{n=+\infty} \delta\left(x - \frac{n}{\Delta k} \right) , \quad 1.56$$

Hence, the object $M_{\perp}(x)$ is periodically replicated and the distance between corresponding voxels is given by $2\pi / \Delta k$, referred to as the field-of-view (*FOV*):

$$FOV \equiv 2\pi / \Delta k \quad 1.57$$

In case the dimension of the object is larger than the *FOV*, the image overlaps with itself. To avoid such aliasing artifacts, the *FOV* requires being larger than the object or the step size in *k*-space Δk must be small enough according to the *Nyquist sampling criterion*. According to Eq. 1.53, the object is also convoluted with a sinc-function due to truncation of *k*-space. The width of the main lobe of the sinc-function, which is exactly the pixel size Δx (i.e. $\Delta x = FOV / N$), is not infinitely small and thus the image is blurred (Figure 1.5 (b)). Nearby object edges, the side lobe of the sinc-function are responsible for streaking and ringing artifacts, referred to as *Gibbs-Ringing* or *Gibbs-Artifacts*.

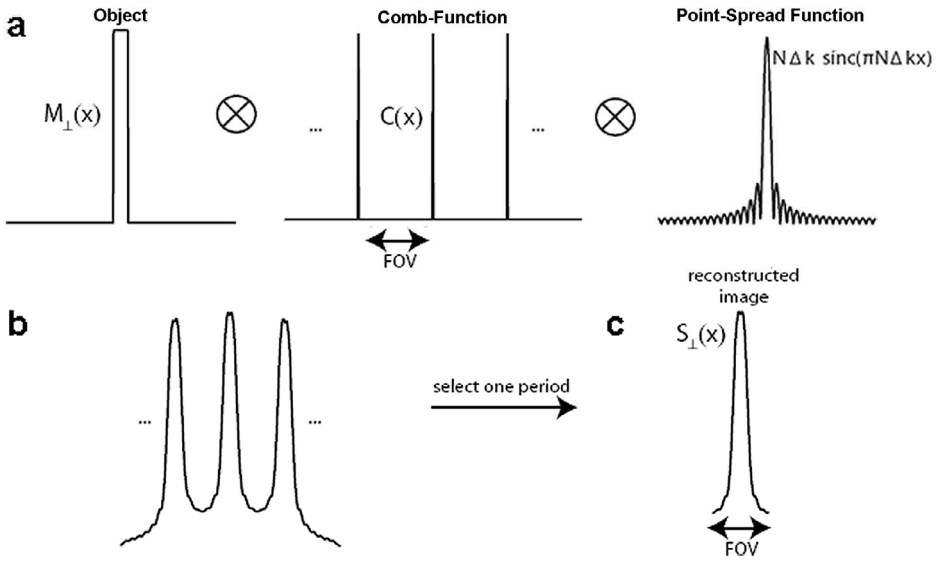

Figure 1.5 – Data Sampling and Image Reconstruction.
*(**a**) Convolution of the imaging object with a Comb-Function of periodicity FOV = 2π/Δk and a sinc-function (see Eq. 1.53). (**b**) Blurred replicas of the image (left). The final image (right) is obtained by the selection of one (arbitrary) replica. Adopted from (Heiler 2011).*

1.2.4 Point-Spread Function and Spatial Resolution

The spatial resolution Δx is physically limited by the largest wave number $k^{\max} = N \cdot \Delta k / 2$ in *k*-space:

$$\Delta x = \frac{2\pi}{k^{\max}} \tag{1.58}$$

Using typical matrix sizes in fMRI between 64 x 64 and 128 x 128 pixels, the nominal spatial resolutions vary between 1.5 mm and 3.0 mm. Among others, the effective spatial resolution is further compromised due to T_2*-decay during the signal read out. Hence, *k*-space is not only truncated but also weighted so that the sampling function in Eq. 1.50 must be modified to

$$SF(k) = c(k) \cdot \mathrm{rect}(k) \cdot w(k), \tag{1.59}$$

with the weighting function $w(k)$. Accordingly, Eq. 1.53 changes to

$$S_{\perp}(x) = M_{\perp}(x) \otimes C(x) \otimes FFT(\text{rect}(x)) \otimes W(x) \quad 1.60$$

$$= M_{\perp}(x) \otimes \text{PSF}(x), \quad 1.61$$

with $W(x)$ being the Fourier transform of the weighting function and $PSF(x) = C(x) \otimes FFT(\text{rect}(x)) \otimes W(x)$ being the Point-Spread Function (*PSF*). The *PSF* specifies how an idealized point like object is displayed. According to Eq. 1.60, the signal decay during read out causes additional blurring. Within the *FOV*, the *FWHM* of the main lobe of the *PSF* can be larger than the pixel size Δx, which depends on the matrix size, the read out bandwidth, and the relaxation rate. In this case, the effective spatial resolution is given by the *FWHM* of the *PSF*. Blurring due to T_2*-decay primarily occurs along the PE direction since the sampling rate in frequency encoding direction, also referred to as read out (RO) direction, is much faster than in PE direction.

1.2.4.1 Signal-to-Noise Ratio

A major goal in MRI is to increase both, spatial and temporal resolution. Unfortunately, this attempt is fundamentally limited by the *SNR*. For a given voxel volume Δx^3, a signal read out duration t_{acq}, N_{PE} phase encoding lines, and N_{avg} averages, the *SNR* is given by:

$$SNR \propto \Delta x^3 \sqrt{N_{PE} \cdot N_{avg} \cdot t_{acq}} \quad 1.62$$

Hence, increasing the spatial or the temporal resolution, both decreases the *SNR*. Since BOLD signal changes are in the order of 5 % of the baseline signal, sufficient *SNR* is essential to detect neuronal activation.

2D-Multislice versus 3D Imaging

In fMRI, typically large imaging volumes are acquired. In this case, the *SNR* can be significantly improved using 3D compared to 2D imaging sequences. For a gradient-echo imaging sequence with an echo time *TE* and a repetition time *TR* ($TR << T_1$), the steady state signal is given by

$$S = S_0 \frac{\left(1 - e^{-TR/T_1}\right) \cdot e^{-TE/T_2^*} \cdot \sin(\alpha)}{1 - \cos(\alpha) \cdot e^{-TR/T_1}} \tag{1.63}$$

For a given *TR* and T_1, the signal is maximal when the flip angle corresponds to the *Ernst-Angle* α_E (Ernst and Anderson 1966):

$$\alpha_E = \arccos\left(e^{-TR/T1}\right) \tag{1.64}$$

According to Eq. 1.63, Eq. 1.64, and further considering that the *SNR* is proportional to the square root of the signal read out t_{acq}, the *SNR* can be expressed as:

$$SNR = S_0 \frac{\left(1 - e^{-TR/T_1}\right) \cdot e^{-TE/T_2^*}}{TR \cdot \sqrt{1 - e^{2 \cdot TR/T_1}}} \sqrt{t_{acq}} \tag{1.65}$$

For the *SNR* comparison between 2D and a 3D imaging, the following assumptions are made: First, all imaging parameters are the same except that in the 2D case only one slice is excited at a time whereas in the 3D case the whole imaging volume is excited with each RF-pulse. Second, when the time interval between the excitations of a 2D imaging slice is *TR*, then the time interval between the excitations of a 3D imaging volume is *TR/N*, with *N* being the slice number.

$$TR^{2D} = TR\,;\; TR^{3D} = TR / N \tag{1.66}$$

Further, when N_y and N_z denote the number of phase encoding lines in *y* and *z* direction, respectively, then the 2D and 3D sequence time is given by:

$$T_{seq}^{2D} = N_y \cdot T_{RO} \tag{1.67}$$

$$T_{seq}^{3D} = N_y \cdot N_z \cdot T_{RO} \tag{1.68}$$

According to Eq. 1.65, 1.66, 1.67, and 1.68, the *SNR* ratio of a 3D and 2D sequence is given by:

$$\frac{SNR_{3D}}{SNR_{2D}} = \sqrt{N} \cdot \sqrt{\frac{1 - e^{-2 \cdot N \cdot T_{seq}/T_1}}{1 - e^{-2 \cdot T_{seq}/T_1}}} \cdot \frac{1 - e^{-T_{seq}/T_1}}{1 - e^{-N \cdot T_{seq}/T_1}} \tag{1.69}$$

Here, it was assumed that the same number of slices was acquired with both types of sequences ($N = N_z$). According to Eq. 1.69, the *SNR* gain using a 3D compared to a 2D sequence is expected to increase with the slice number *N*.

1.3 Physiological Background

The Blood-Oxygenation-Level-Dependent (BOLD) effect was discovered by Ogawa and colleagues (1990a; 1990b) and enables the detection of neuronal activation in the brain. This section gives a brief introduction to the physiological basics and mathematical models of the BOLD effect. For a more extensive presentation, it may be referred to (Buxton 2002; Buxton, et al. 1998) and (Jezzard, et al. 2001).

1.3.1 Blood Physiology

Blood constitutes between 6-8 % of the human body weight and is composed of the plasma consisting to approx. 90 % of water, and cellular properties consisting of white blood cells, cell fragments, and primarily of the red blood cells (erythrocytes). Each erythrocyte contains approximately $3 \cdot 10^8$ hemoglobin molecules transporting oxygen and carbon dioxide. The hemoglobin molecule is composed of 2 x 2 polypeptide chains each with one heme group able to reversely bind one oxygen molecule. Hence, each macromolecule can bind a maximum of four O_2-molecules. The heme molecule itself consists of four pyrrole rings, which are assembled to a porphyrin ring (Figure 1.6).

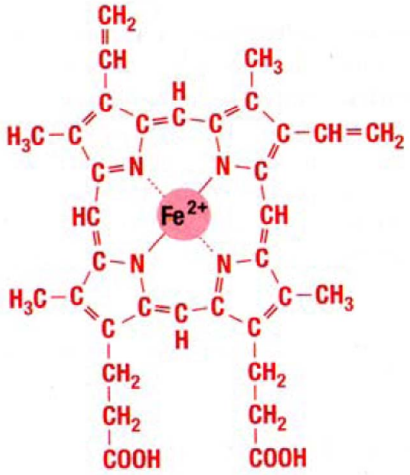

Figure 1.6 – Chemical Structure of the Hemoglobin Molecule.
Source: (Thews 1997)

The iron atom in the center of the molecule makes hemoglobin paramagnetic. Ligand bindings between the double charged iron atom can occur with the surrounding nitrogen atoms of the pyrrole rings, with the polypeptides, and with oxygen. The electric configuration of the free double charged $^{2+}$Fe-atom without ligands is [Ar]3d^6, in which the energy level of the 3d^6-electrons are degenerated. According to the Hund´s rule, two of the six electrons are paired and four electrons are unpaired, yielding a total spin of S = 2 (Figure 1.7). In hemoglobin, there is a weak ligand field and the degeneracy breaks up (Riedel 2004). Now three of the five orbital are energetically reduced and two are increased but the total spin is still S = 2. The binding of oxygen to the iron atom increases the ligand field and the energy level of the 3d^6-electrons split further up so that the electrons occupy only three of the five 3d orbital. Because all electrons are now paired, the total spin is reduced to zero (S = 0) and the oxygenated hemoglobin (i.e. oxyhemoglobin) is diamagnetic. The different magnetic properties of oxyhemoglobin and deoxygenated hemoglobin (i.e. deoxyhemoglobin) has been discovered by Pauling and Coryell (1936).

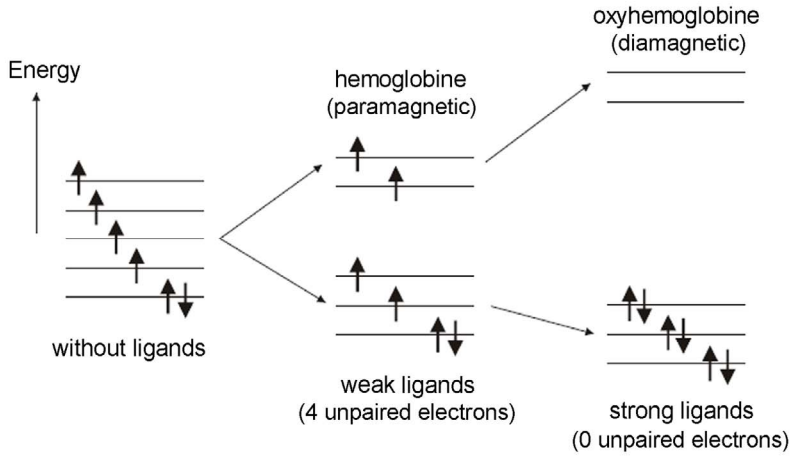

Figure 1.7 – Energy Splitting of the 3D-Electron Orbital of Iron in a Ligand Field.
Source: (Thulborn and Brady 1989)

1.3.2 BOLD Effect

In fMRI, the BOLD effect (Ogawa, et al. 1990a; Ogawa, et al. 1990b) causes blood oxygenation level dependent signal differences facilitating the indirect measurement of the local brain activity. For neuronal activity, the neurons require energy in form of oxygen and glucose being supplied by the blood. In animal studies, it has been shown that the deoxyhemoglobin content in the blood increases simultaneously with the neuronal activity (Malonek, et al. 1997). More paramagnetic deoxyhemoglobin leads to local field disturbances of the main magnetic field B_0 (Figure 1.8) affecting the local transversal relaxation times T_2 and T_2* (see Section 1.1.5.2). In more detail, the field inhomogeneities outside a paramagnetic blood vessel cause a frequency shift $\Delta\omega$ given by:

$$\Delta\omega = 2\pi\omega_0\Delta\chi\left(1-Y\right)\sin^2\left(\vartheta\right)\left(a/r\right)^2\cos\left(2\Phi\right) \qquad 1.70$$

Here, $\Delta\chi$ is the susceptibility difference between the vessel and the surrounding tissue, Y the blood oxygenation level, α the vessel (cylinder) radius, r the shortest distance between the position $\vec{r}$ of the observer and the cylinder axis, ϑ the angle between the B_0-field, and Φ the angle between $\vec{r}$ and the projection of B_0 onto the transversal plane spanned by $\vec{r}$. Due to neurovascular coupling (Villringer and Dirnagl 1995), the higher metabolic rate of the neurons when they are activated leads to an increase of the local

perfusion which by far exceeds the higher demand of oxygen (Fox and Raichle 1986). Hence, the paramagnetic deoxyhemoglobin content on the venous side of the tissue is actually decreased during neuronal activity effectively increasing local transversal relaxation times T_2 and T_2*, which can be detected with spin-echo or gradient-echo imaging sequences.

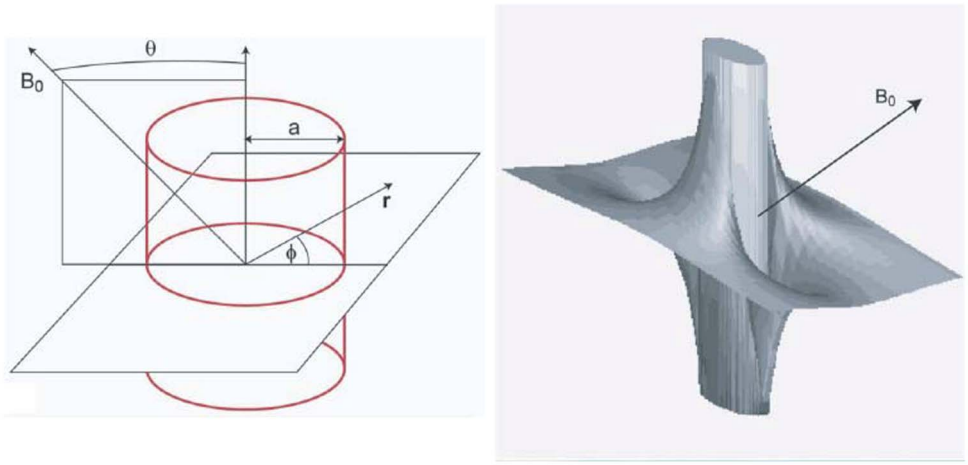

Figure 1.8 – Magnetic Field Created by a Paramagnetic Cylindrical Blood Vessel.
Source: (Norris 2006)

1.3.2.1 BOLD Model

This section briefly summarizes the BOLD model introduced by Hoge et al. (1999). The BOLD signal change in fMRI is caused by the interplay between the regional cerebral oxygen consumption ($rCMRO_2$), the blood flow ($rCBF$), and by the blood volume ($rCBV$). For an effective relaxation rate $R_2^* = 1/T_2^*$, the MR signal can be written as:

$$S = S_0 e^{-TE\cdot(R_2^{*(BOLD)} + R_2^{*(other)})} \qquad 1.71$$

The first term in the exponential describes the relaxation due to the BOLD effect and the second term is related to other sources. During neuronal activation, the transversal relaxation rate changes from $R_2^*(0)$ to $R_2^*(t)$, where $R_2^*(0)$ denotes the relaxation rate during resting state. In the following, ΔR_2^* expresses the change of the relaxation rate between activation and rest:

$$\Delta R_2^* = R_2^*(t) - R_2^*(0) \tag{1.72}$$

The BOLD signal change ΔS^{BOLD} is given by

$$\Delta S^{BOLD} = S(0)\left(e^{-TE\cdot\Delta R_2^*} - 1\right), \tag{1.73}$$

with $S(0)$ being the baseline signal (i.e. BOLD signal during rest). The connection between the physical parameter R_2^* and the physiological parameters $rCBV$ and dHb_V, the venous concentration of deoxyhemoglobin is given by the semi-empirical formula,

$$R_2^{*(BOLD)} = K \cdot rCBV \cdot dHb_V^{\beta}, \tag{1.74}$$

where the constant K is sample and field strength dependent and the constant β depends on the average blood volume in the tissue. Using this relationship, whose accuracy has been thoroughly validated using in vitro models (Boxerman, et al. 1995), then ΔR_2^*, defined in Eq. 1.72, can be written as:

$$\Delta R_2^* = K \cdot \left(rCBV \cdot (dHb_V)^{\beta} - rCBV(0) \cdot (dHb_V(0))^{\beta}\right) \tag{1.75}$$

Connecting this relation with Eq. 1.73, the BOLD signal change in dependence of physiological parameters can be expressed as:

$$\Delta S^{BOLD} \approx S(0) \cdot M \cdot \left(1 - \frac{rCBV}{rCBV(0)} \cdot \left(\frac{dHb_V}{dHb_V(0)}\right)^{\beta}\right) \tag{1.76}$$

with $M = TE \cdot K \cdot rCVBV(0) \cdot (dHB_V(0))^{\beta}$. This relationship was obtained by the linearization of Eq. 1.73, assuming small BOLD signal changes as they are observed in fMRI experiments. In PET measurements, it has been shown that a change of the cerebral blood flow $rCBF$ leads to a change of the cerebral blood volume $rCBV$, which is empirically given by:

$$\frac{rCBV}{rCBV(0)} = \left(\frac{rCBF}{rCBF(0)}\right)^{\alpha} \tag{1.77}$$

Based on this equation, the regional cerebral oxygen consumption $rCMRO_2$ is given by:

$$rCMRO_2 = 4 \cdot rCBF \cdot dHb_V \qquad 1.78$$

The factor 4 results from the fact that each hemoglobin molecule can bind four O_2-molecules. Combining Eq. 1.76, Eq. 1.77, and Eq. 1.78, the BOLD signal change can be expressed in a more convenient form:

$$\Delta S^{BOLD} = S(0) \cdot M \left(1 - \left(\frac{rCMRO_2}{rCMRO_2(0)} \right)^{\beta} \left(\frac{rCBF}{rCBF(0)} \right)^{\alpha - \beta} \right) \qquad 1.79$$

With the experimentally verified constants α = 0.38 (Grubb, et al. 1974) and β = 1.5 (Davis, et al. 1998), the experimentally observed monoton signal increase for increasing blood flow can be explained (Villringer and Dirnagl 1995). The typical BOLD response after a short stimulus is characterized by three different phases, the *initial-dip*, the main BOLD response, and the *post-stimulus undershoot* (Figure 1.9). Delayed perfusion increase after a stimulus (Malonek, et al. 1997) leading to increasing deoxyhemoglobin content on the venous side of the tissue should explain the *initial-dip* approx. 2 seconds after a stimulus. The main BOLD response, with a *FWHM* of approx. 4 seconds (de Zwart, et al. 2005), occurs after the high deoxyhemoglobin concentration is washed out by the increased perfusion, approximately 5 seconds after a stimulus. Up to date, there is no generally accepted theory for the *post-stimulus undershoot*, which refers to the decrease of the BOLD signal below the base line level which can last up to one minute (Frahm, et al. 1996). Possibly, there is a delayed decrease of the $rCBV$ (Buxton, et al. 1998) or an already decreasing $rCBF$ while the $rCMRO_2$ is still above the normal level.

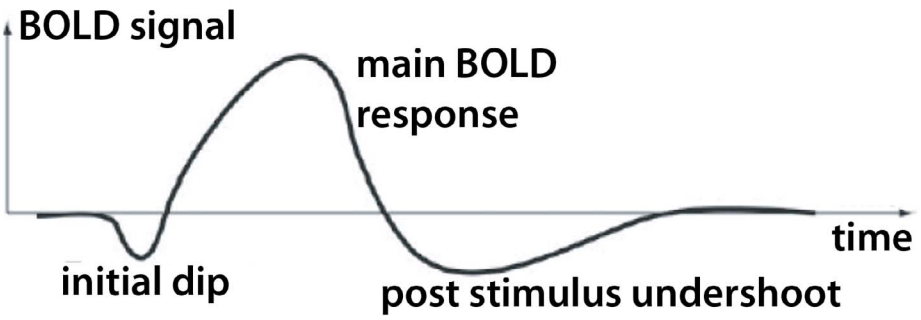

Figure 1.9 – Hemodynamic Response Function After a Short Stimulus.
Adopted from (Norris 2006).

2 Material and Methods

2.1 Hardware

All imaging was performed at a 3 T whole-body MR-system (Magnetom Trio, Siemens Healthcare, Erlangen, Germany) using a 12- and a 32-channel head coil. In this work, the standard 12-channel head coil, suitable for most fMRI setups including earphones and goggles, was used for most fMRI studies. The 32-channel coil with a reduced diameter compared to the 12-channel coil enables higher *SNR* and PI-performance (de Zwart, et al. 2004) and was used for the sophisticated motivation-task study (see Section 3.2.4). All studies were approved by the local ethics committee and written informed consent was obtained prior to examinations.

2.1.1 MR Tomograph

The 3 T scanner with a magnet of 213 cm length and a bore of 60 cm was developed and manufactured by Siemens and allows a maximal field-of-view of 40 cm sufficient for whole-body imaging applications. The main magnetic field is created without electrical resistance using wires made of a niobium-titanium composition with copper cable coating, superconducting at 12 K. Hence, energy is only required for the cooling of the magnet using liquid helium with the lowest boiling point of all elements at 4.2 K. Field homogeneity of 1 ppm within a spherical volume of 50 cm is guaranteed using so-called shim coils, located on a ring within the main coil creating an additional magnetic field compensating magnetic field inhomogeneities. Due to safety regulations, the maximum gradient strength perpendicular to B_0 (i.e. in *x/y*-direction) and parallel to B_0 (i.e. in *z*-direction) is limited to 40 mT/m and 45 mT/m, respectively. For the same reason, the gradient slew-rates in *x/y*- and *z*-direction are limited to 180 T/m/s and 220 T/m/s, respectively.

2.1.2 Radiofrequency Coils

The RF coils can be used in transmit and receive mode. In the transmit mode, the RF coil transfers energy to the spin system and thereby tips the magnetization vector from its thermal equilibrium alignment parallel to B_0 into the transversal plane. In the receive

mode, the RF coil must be sensitive to detect a current induced by the precessing magnetization of the excited spins (see Section 1.1.4). Generally the different coil setups used in MRI can be separated into so-called surface and volume coils. For large imaging volumes, volume coils yield more homogeneous B_1-fields facilitating better flip-angle excitation whereas for smaller imaging volumes they are less sensitive to detect signals from the excited spins compared to surface coils. With focus on the requirements in whole-brain fMRI, solely volume coils were used for all fMRI experiments presented in this work. The relation between the current in an electric conductor and the resulting magnetic field is described by the *Biot-Savart law*:

$$d\vec{B} = \frac{\mu_0 I}{4\pi r^3} \vec{r} \times d\vec{l} \qquad 2.1$$

Here, I denotes the electric current, $d\vec{l}$ the vector of the live conductor, and $\vec{r}$ the vector between the conductor and the position where the magnetic field is measured. It has to be noted that the *Biot-Savart law* holds only for continuous currents or if the dimension of the coil is large compared to wavelength of the current in the coil, which was true for the MR experiments in this work. A more extensive presentation of high-frequency MRI can be found in the publication (Robitaille and Berliner 2006).

2.2 Measurement Techniques

The measurement techniques applicable for fMRI can be separated into two categories, the spin-echo (SE) and the gradient-echo (GE) echo-planar imaging (EPI) sequences. The GE-EPI sequences are characterized by high temporal resolution and high BOLD sensitivity but suffer from signal drop outs and image distortions in areas affected by susceptibility gradients. In comparison, the SE-EPI sequences avoid potential signal loss caused by through-slice dephasing and are able to detect BOLD activation more precisely (i.e. closer to neuronal activity) compared to GE-EPI sequences (Boxerman, et al. 1995; Ogawa, et al. 1993). However, the SE-EPI is less sensitive to BOLD signal changes because static dephasing effects do not contribute. Furthermore, SE-EPI suffers from low temporal resolution and transfers more energy to the tissue in form of heat due to the 180°-refocusing pulses. GE-EPI is used more often compared to SE-EPI because today´s neuroscience studies often use event-related stimulus paradigms (see Section

2.4.1) requiring fast imaging strategies to detect transient signal modulations. Further, high BOLD sensitivity is necessary to compensate for the limited statistical power of such event-related study designs. In this work, two types of GE-EPI sequences were used for fMRI briefly described in the following sections.

2.2.1 Single-Shot EPI

Single-shot EPI (Mansfield 1977) allows the acquisition of one imaging slice in approximately 100 ms. EPI is used in most of today´s fMRI studies combining whole-brain coverage and high temporal resolution (i.e. 30-40 slices / 2-3 sec). The high temporal resolution of EPI is accomplished by acquiring the *k*-space data of each slice after a single RF-excitation. The trajectory in *k*-space is defined by the amplitudes and the temporal order of the readout gradients and the blips (see Section 1.2.2). From the sequence diagram of the single-shot EPI (Figure 2.1) can be seen that after the application of a slice-selective RF-pulse, the maximal *k*-space position (k_x^{max}, k_y^{max}) is reached by applying the frequency encoding gradient G_x and the phase encoding gradient G_y. The dephasing in *y*-direction is fully compensated until the time *TE* by successively applying so-called blip-gradients or "blips". Between blips, frequency gradients with opposite polarities are alternated to acquire the *k*-space data along the *x*-direction.

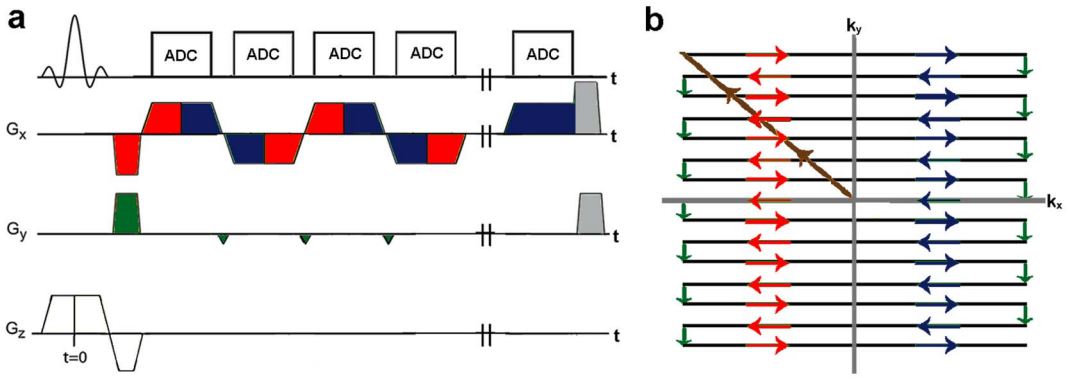

Figure 2.1 – Single-Shot EPI Sequence Diagram and Data Acquisition in k-Space.
*The single-shot EPI (**a**) acquires the whole k-space matrix after a single RF-excitation. K-space matrix lines (**b**) are acquired using frequency encoding gradients with different polarities (red, blue). The next line is reached applying a small phase encoding gradient "blip" (green). After the acquisition of the whole data matrix, the signal is dephased using spoiler gradients (grey) to avoid interactions of the remaining transversal magnetization and the next RF-pulse.*

2.2.1.1 BOLD Sensitivity

During neuronal activation, the BOLD effect alters microscopic background fields and thus the irreversible relaxation rate T_2^*. In order to detect local changes of neuronal activation, the signal has to be susceptible to small changes of T_2^*. The BOLD sensitivity (*BS*) is a measure of the local signal intensity change dI related to changes of local T_2^*-relaxation times dT_2^* and is proportional to the derivative of the signal intensity with respect to T_2^*, $BS \sim dI / dT_2^*$. Neglecting macroscopic background fields, the signal intensity is given by:

$$I = \rho \cdot e^{-TE/T_2^*} \qquad 2.2$$

The first-order Taylor expansion of the signal intensity (Eq. 2.2), evaluated at the T_2^*-value during the baseline state T_{2B}^*, can be written as

$$I = \rho \cdot e^{-TE/T_{2B}^*} \left(1 + \frac{TE}{T_{2B}^{*\,2}} \cdot \left(T_2^* - T_{2B}^* \right) \right), \qquad 2.3$$

where ρ is the local spin density. Equation 2.3 motivates the following definition for the BOLD sensitivity (Deichmann, et al. 2002):

$$BS \equiv T_{2B}^{*2} \left. \frac{dI}{dT_2^*} \right|_{T_2^* = T_{2B}^*} \qquad 2.4$$

Accordingly, the BOLD sensitivity is given by the simple expression

$$BS = TE \cdot I\,, \qquad 2.5$$

which has been experimentally verified (Lipschutz, et al. 2001). Maximal *BS* is reached when *TE* is equal to T_2^*, which is in accordance with literature results presented in the work of Gati and colleagues (1997). In the following, the effects of macroscopic field inhomogeneities on *BS* will be considered. Through-plane gradients in *z*-direction G_{ss} cause extra spin dephasing along the slice direction. Accordingly, the expression for the signal intensity given by Eq. 2.2 has to be modified to

$$I = \rho \cdot e^{-TE/T_2^*} \int P(z') e^{i \cdot \gamma \cdot G_{ss} \cdot z' \cdot TE} dz'\,, \qquad 2.6$$

where $P(z)$ denotes the slice profile and γ the gyromagnetic ratio. Assuming rectangular slice profiles, which were used for all measurements in this study, the integral in Eq. 2.6 can be analytically computed and is given by $\mathrm{sinc}\left(\gamma G_{ss} TE \Delta z / 2\right)$, where Δz *d*enotes

the slice thickness. As discussed in the work of Deichmann and colleagues (2002), macroscopic in-plane gradients G_{SP} parallel to the EPI phase encode direction alter the sampling rate and therefore also the signal intensity. They further shift the effective echo time TE^{eff} of the central gradient-echo of the EPI read out. Both effects can be described by the single variable Q, defined as

$$Q = 1 - \gamma \cdot \Delta t \cdot FOV \cdot G_{SP} / 2\pi \ , \qquad 2.7$$

where Δt denotes the time between consecutive gradient-echoes and FOV the field-of-view in PE direction. The parameter Q affects the signal and the echo time in the following way:

$$I = \frac{I_0}{Q} \text{ and } TE^{eff} = \frac{TE}{Q} \qquad 2.8$$

In Eq. 2.8, I_0 and TE denote the signal intensity and respectively the effective echo time in a perfectly homogeneous magnetic field (i.e. no susceptibility gradients). Eq. 2.7 shows that Q is equal to one if the field gradients G_{sp} are zero. Depending on the sign of the gradients, Q becomes smaller or greater than one. According to Eq. 2.8, the gradient-echo is shifted to smaller or to higher TE -values if the in-plane gradients are parallel or antiparallel to the EPI phase encoding direction. The signal intensity and thus BOLD sensitivity is completely lost if the gradient echo is shifted outside the EPI read out window of the duration TA:

$$\left| TE - \frac{TE}{Q} \right| > \frac{TA}{2} \qquad 2.9$$

Here, TA depends on the number of phase encoding steps and the bandwidth per pixel (Gati, et al. 1997). According to Eq. 2.6 and Eq. 2.8, the signal intensity in the presence of macroscopic field inhomogeneities along the EPI phase encoding and slice direction is given by:

$$I = \frac{\rho}{Q} e^{-TE/(Q \cdot T_2^*)} \int_{z'} P(z') \cdot e^{i\gamma G_{ss} z' TE} dz' \qquad 2.10$$

Considering macroscopic background fields and applying the definition for the BOLD sensitivity (see Eq. 2.4) to the 1st order Taylor expansion of Eq. 2.10 yields the following expression:

$$BS = \frac{TE}{Q^2} \cdot \rho \cdot e^{-\frac{TE}{QT_2^*}} \cdot \mathrm{sinc}\left(\gamma \cdot G_{ss} \cdot TE \cdot \Delta z / 2\right) \qquad 2.11$$

Since *BS* is proportional to $1/Q^2$, the maximal value of the *BS* increases for positive gradients ($Q < 1$) and decreases for negative gradients ($Q > 1$) (i.e. in-plane gradients are parallel or antiparallel to the EPI phase encoding direction). In the case of non-zero in-plane gradients ($G_{sp} \neq 0\,; G_{ss} = 0$) the optimal echo time is shifted to $TE = Q \cdot T_2^*$. Non-zero through-plane gradients ($G_{ss} \neq 0\,; G_{sp} = 0$) shift the *BS*-maximum to lower *TE*-values due to additional signal dephasing in slice direction.

2.2.2 Segmented EPI

Due to the long signal read out, the EPI is prone to blurring, signal loss, and image distortions in areas affected by susceptibility gradients compromising spatial specificity. Sacrificing temporal resolution, segmented EPI techniques have been proposed (Butts, et al. 1994; McKinnon 1993) to increase spatial accuracy by acquiring the *k*-space matrix after multiple RF-excitations (Figure 2.2). Accordingly, blurring artifacts are reduced because the signal read out duration after a single RF-pulse is much shorter compared to the read out of the whole *k*-space matrix using single-shot EPI. Moreover, the spin history is less affected by magnetic background fields manifesting in reduced image distortions. The spatial accuracy was further improved by Voit and Frahm (2005) shifting consecutive echo-trains by a few milliseconds in time to smooth the weighting of the *k*-space data allowing fMRI at sub-millimeter spatial resolution (Heiler, et al. 2010; Voit and Frahm 2005).

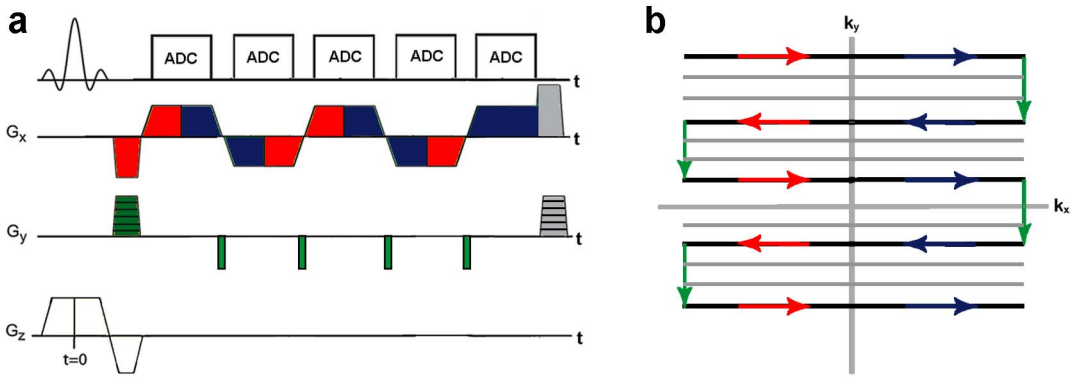

Figure 2.2 – Segmented EPI Sequence Diagram and Data Acquisition in k-Space.
*The segmented EPI (**a**) divides the k-space matrix into segments and acquires only a fraction of the whole k-space matrix after one RF-excitation. K-space matrix lines (**b**) are acquired using frequency encoding gradients with different polarities (red, blue). The blips (green) have the same duration as the blips of a single-shot EPI whereas the amplitude is increased in order to skip a predefined number of lines. With each RF-excitation, the set of k-space matrix lines is altered by varying the amplitude of the phase encoding gradient. After the read out, the signal is dephased by the spoiler gradients (grey) to avoid interactions of the transversal magnetization with the next RF-pulse. One single time frame is acquired applying multiple RF-excitations until all lines of the k-space matrix are acquired.*

2.3 Image Acceleration Techniques

The first part of this section describes the principles of parallel imaging (Griswold, et al. 2002; Pruessmann, et al. 1999; Sodickson, et al. 1999; Sodickson and Manning 1997), which today is the most commonly used image acceleration technique in the clinical routine. The second part explains the basic principles of the UNFOLD method (Madore, et al. 1999) particularly effective to increase the image acquisition speed in dynamic imaging modalities such as fMRI and cardiac imaging.

2.3.1 Parallel Imaging

Parallel imaging increases the image acquisition speed by using the spatial information of multiple receiver coils reducing the number of phase encoding steps required for image reconstruction. The idea of PI already evolved at the end of the 1980s (Carlson 1987; Hutchinson and Raff 1988; Kelton, et al. 1989) while SMASH (Sodickson and Manning 1997) was the first successful PI application achieved in 1997. Today, GRAPPA (Griswold, et al. 2002) and SENSE (Pruessmann, et al. 1999) are the mostly

used PI algorithms performing the image reconstruction in *k*-space and in image space, respectively. In this work, the GRAPPA algorithm was chosen because the image reconstruction is more robust (i.e. less artifacts) and less prone to noise particularly for EPI (Blaimer, et al. 2004; Preibisch, et al. 2008).

Grappa Algorithm

With PI, the FID signal is simultaneously measured with multiple spatially distant receiver coils (indexed with l). For a given coil sensitivity $C_l(\vec{r})$, the MR signal at the spatial coordinate $\vec{r}$ can be expressed as

$$S_{l,\kappa} \propto \int_V M_{xy}(\vec{r}) \cdot C_l(\vec{r}) e^{-i\vec{k}_\kappa \cdot \vec{r}} dV \,, \qquad 2.12$$

where κ numbers the according spatial frequency vectors $\vec{k}_x$. The challenge in PI is to obtain the transversal magnetization $M_{xy}(\vec{r})$, which cannot be obtained by a simple Fourier transformation of Eq. 2.12. A general approach to solving this problem is to express $M_{xy}(\vec{r})$ as a linear combination of the signal $S_{l,k}$ measured in each coil.

$$M_{xy}(\vec{r}) = \sum_{l,\kappa} F_{l,\kappa}(\vec{r}) S_{l,\kappa}(\vec{r}) \qquad 2.13$$

The reconstruction matrix $F_{l,\kappa}$ contains the weighting coefficients for the different signal contributions. Using GRAPPA, the image reconstruction is performed in *k*-space. With a PI reduction factor *R*, the signals of the missing phase encoding lines, $S_j(k_y - m \cdot \Delta k_y)$ ($m = 1, \ldots, R - 1$), of the coil j can be reconstructed from the undersampled signals S_l of the coil l:

$$S_j\left(k_y - m\Delta k_y\right) = \sum_{l=1}^{L} \sum_{b=0}^{N_b - 1} n(j,b,l,m) S_l(k_y - bR\Delta k_y) \qquad 2.14$$

The optimal weighting coefficients *n(j, b, l, m)* are determined by fitting Eq. 2.14 to the signals S_l of the undersampled *k*-space data and the signals of reference lines S_j. The reference lines in the vicinity of the *k*-space center are acquired once at the beginning of the measurement. Adjacently, the recovered *k*-space data of each channel *j* are Fourier transformed. The pixel intensities *P* of the final image are the combination of the pixel intensities p_j of the images of the single coils using sum-of-squares reconstruction,

$$P = \sum_{l=1}^{L} p_j^2 \,, \qquad 2.15$$

which is independent of the coil position and yielding high *SNR* (Roemer, et al. 1990).

2.3.2 UNFOLD Method

Madore and colleagues (1999) have shown that in some dynamic applications (e.g. cardiac imaging and fMRI) the temporal dimension of the image time series (i.e. *t*-axis) is not densely filled with information. They proposed a dynamic undersampling scheme to transfer information from the *k*-axes to the *t*-axis allowing a denser *kt*-space to be acquired leading to significant reductions in the acquisition time of single timeframes. Characteristic of the UNFOLD method is the interleaved sampling pattern (Figure 2.3). The example shows that *k*-space data in frequency encoding direction (i.e. k_x-direction) is densely sampled whereas every other phase encoding line in k_y-direction is skipped effectively reducing the read out duration for a single timeframe by a factor of two. Undersampling in *k*-space leads to spatial aliasing (see Section 1.2.3) which has to be removed before fMRI datasets acquired with UNFOLD can be statistically analyzed in the time domain using the GLM (see Section 2.4.3.1). The idea of UNFOLD is to temporally label the aliased signals with a known frequency and to remove such signals later during data post-processing.

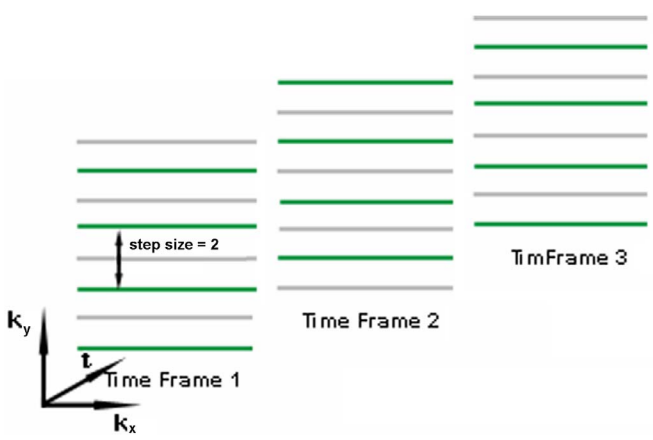

Figure 2.3 – UNFOLD Sampling Scheme in kt-Space.
Depicted are the sampling patterns for the three consecutive time frames of a time series. The green lines along the frequency direction k_x are densely sampled whereas the gray lines are skipped. The sampling pattern is shifted over the time.

Temporal Labelling of Spatial Signals

According to Eq. 1.61, in the image domain the object $O(x)$ is convolved with the spatial *PSF*.

$$I(x) = O(x) \otimes PSF(x) \qquad 2.16$$

The interleaved sampling pattern of UNFOLD can be described by alternately shifting the sampling function $SF(k)$ (see Eq. 1.50) by $\Delta k \cdot f$ in PE direction, with $f \in [0...1]$. Thus, according to the shift theorem, the phase of the *PSF* changes over time:

$$FFT(SF(k + \Delta k \cdot f)) = PSF(x) \cdot e^{i \cdot \Delta k \cdot f \cdot x} \qquad 2.17$$

Figure 2.4 depicts the sampling function and the according *PSF* for *f = 1/2* (i.e. the sampling function is shifted by $\Delta k / 2$ between consecutive timeframes). According to Eq. 2.17, shifting the sampling function does not affect the phase of the central *PSF*-peak at $x = 0$ but adds a phase of $\Delta\varphi = f \cdot n \cdot 2\pi$ ($n = 2, 4, 6\ldots$) to the side lobes of the *PSF* (i.e. at $x = n \cdot 2\pi / \Delta k$). According to Eq. 2.16 and Eq. 2.17, if an object to be imaged is twice as large as the *FOV*, meaning that two points of the image overlap into one voxel, the signal intensity of the voxel located at x varies between $O(x) \pm O(x + 2\pi / \Delta k)$ across time. Hence, the "true" signal $O(x)$, which remains stationary, can be easily separated from the alternating aliasing signal $O(x + 2\pi / \Delta k)$.

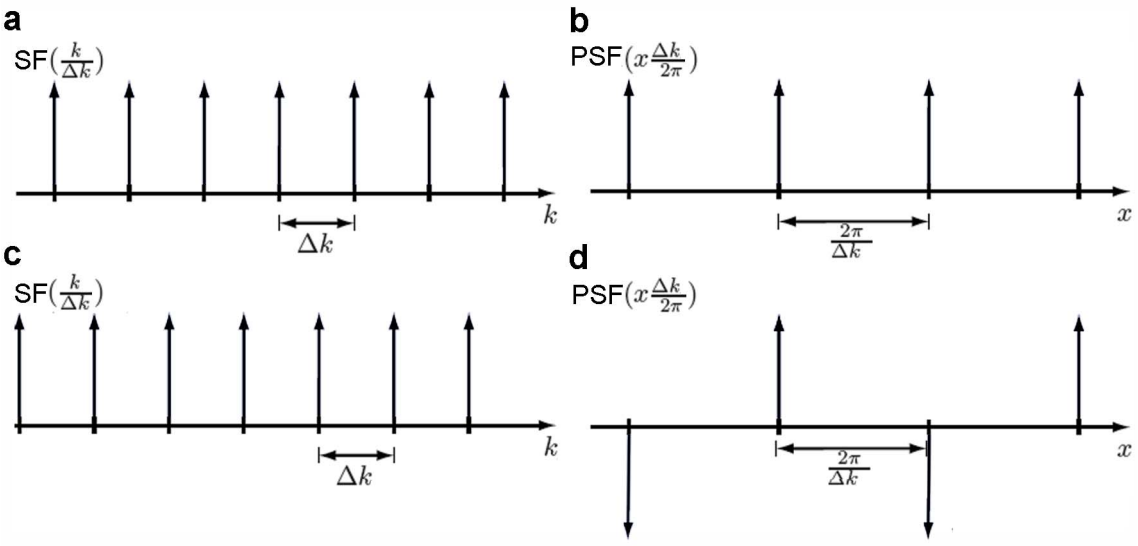

Figure 2.4 – Interleaved Sampling and Dynamic Point-Spread Function.
*Sampling function SF(k/Δk) (**a**) with periodicity Δk and corresponding PSF with periodicity 2π/Δk (**b**). Shifted sampling function (**c**) SF(k/Δk+1/2) and corresponding PSF with phase shifts linear in x (**d**).*

According to Eq. 2.16, if n points of the object overlap into a single voxel (i.e. n-fold aliasing) and the sampling function is shifted by $\Delta k \cdot t / n$ in time, where t is the time or the image number, respectively, then the voxel intensity is given by

$$I(t) = \sum_{j=0,1,..,n} O(j \cdot 2\pi / \Delta k; t) \cdot e^{i \cdot 2\pi \cdot t \cdot j / n}, \qquad 2.18$$

where the exponential is a Fourier basis function. According to Eq. 2.18, the spectrum $\tilde{I}(\omega) \equiv FFT(I(t))$ of a voxel contains n uniformly spaced peaks where each peaks is associated with one of the spatially overlapping points. The images can be unfolded by filtering out the aliasing peaks in the temporal spectrum of each voxel. In fMRI, it is important to ensure that the frequency components resulting from the neuronal activation are not overlapped with the aliasing peaks or with other activation peaks from aliased voxels. For a given temporal filter $F(w)$, the factor f_{SNR} by which the *SNR* is changed, is given by:

$$f_{SNR} = \sqrt{\frac{BW}{\int_{BW} F^2(w) dw}} \left(\frac{V_2 \sqrt{\tau_2}}{V_1 \sqrt{\tau_1}} \right) \qquad 2.19$$

Here, BW denotes the read out bandwidth of the imaging sequence, V_2 / V_1 and τ_2 / τ_1 the voxel volumes and respectively the data acquisition times with / without UNFOLD (Madore, et al. 1999). From Eq. 2.19 can be seen that, on the one hand, the *SNR* of the UNFOLD datasets increases compared to the non-accelerated datasets because temporal filtering removes noise from the power spectrum. On the other hand, the *SNR* decreases because single timeframe are sampled more rapidly.

2.4 The fMRI Experiment

Functional MRI is an imaging technique exploiting the BOLD effect (see Section 1.3.2) to visualize task-related or resting-state neuronal activity in the brain. At a field strength of 3 T, the BOLD signal changes are in the order of 2-10 % similar to the magnitude of the physiological background noise (Kruger, et al. 2001; Purdon and Weisskoff 1998). In order to detect those comparable weak BOLD signals, the subject passes through resting and active states during the fMRI experiment while time series of about 100-300 images are typically acquired. Finally, the time series is statistically analyzed voxel-by-voxel to localize task-related BOLD activation. This section briefly describes the stimulus paradigms, the image post-processing methods, and the statistical analysis tech-

niques used in this work. A broader overview of the basic fMRI principles can be found in the literature (Matthews and Jezzard 2004; Ramsey, et al. 2002).

2.4.1 Stimulation Presentation Types

Various study designs are available in fMRI to investigate brain function whereupon the most prominent ones are the block and the event-related designs. In a block design, a cognitive engagement is maintained in a task by presenting stimuli sequentially within alternating conditions (Figure 2.5 (a)). Blocked designed paradigms were used in the first years of fMRI due to simple modeling of the BOLD response (see Section 2.4.3), high statistical power (Friston, et al. 1999), and large BOLD signal changes related to the baseline (Buxton, et al. 1998; Glover 1999b) leading to robust (Brockway 2000; Loubinoux, et al. 2001) and reproducible results (Friston, et al. 1999). However, block designed stimuli presentations involve numerous assumptions and suffer from neuro-psychological drawbacks. Event-related study designs (Figure 2.5 (b)) present short and often random stimuli. Further they are less sensitive to head-motion (Birn, et al. 1999), avoid habituation effects (D'Esposito, et al. 1999), and are suitable to examine brain regions with transient neural activation (Braver, et al. 2001; Kiehl, et al. 2000; Schacter, et al. 1997) and emotional responses (Buchanan, et al. 2000; Williams, et al. 2001). Another major advantage of using event-related compared to block designs is that transient signal variations in hemodynamic responses are detectable allowing to characterize the BOLD hemodynamic response function (Buxton, et al. 2004; Rosen, et al. 1998), which was found to be spatially variable (Kruggel and von Cramon 1999b).

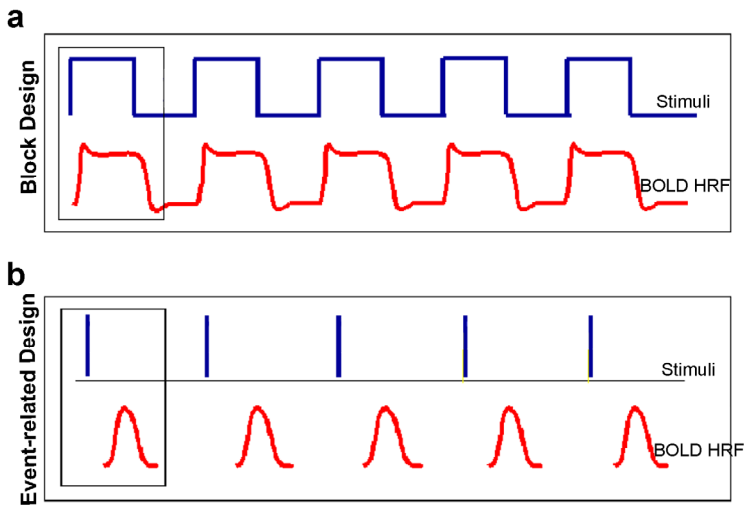

Figure 2.5 – Blocked and Event-Related Stimulus Design.
Adopted from (Amaro and Barker 2006).

2.4.1.1 Stimulation of the Sensorimotor Cortex

The SMC, located in the frontal lobe of the cerebral cortex and involved in planning, control, body movements, is the main sensory receptive area for the sense of touch. The SMC can be activated using a blocked designed fingertapping paradigm. Synchronic with the stimulus paradigm, the volunteers of the fingertapping experiments carried out in this work received start/stop commands communicated via earphones, instructing them to start and respectively to stop bilateral finger movement.

2.4.1.2 Stimulation of the Orbitofrontal Cortex

The OFC is located in the frontal lobes and involved in the cognitive processing of decision making, emotion, and reward. In this work, the OFC was activated using a self-paced probabilistic reversal-learning task adopted from (Linke, et al. 2010). A stimulus was presented via goggles and the volunteers made a forced choice between two playcards on each trial. The “correct" playcard received an 8/2 ratio of positive to negative feedback, whereas the “incorrect" playcard always received negative feedback. Feedback was provided in the form of winning (reward) or loosing (punishment) a small amount of money.

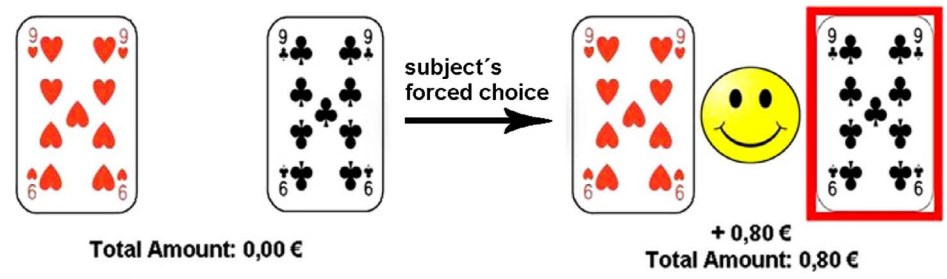

Figure 2.6 – Event-Related Reward-Reversal Task to Activate the OFC.
Adopted from (Linke, et al. 2010).

2.4.1.3 Stimulation of the Nucleus Accumbens

The nucleus accumbens (NAcc) is a subregion of the ventral striatum and can be divided into the shell and the core. The NAcc is associated with reward-learning (Diekhof, et al. 2008; Knutson, et al. 2001) and drug addiction (Diekhof, et al. 2008; Vollstadt-Klein, et al. 2010) and is therefore of great importance for cognitive neuroscience. In this work, an event-related motivation task with pseudorandom trials was used to evoke neuronal activation in the NAcc. Each trial consisted of an anticipation phase, an instrumental response phase, and an outcome phase (Figure 2.7) and was presented via goggles using MRI Audio / Video Systems (Resonance Technology Inc., Los Angeles, CA, USA). During the anticipation interval participants were informed if they could win money in the actual trial (condition "money win") or not (condition "no win"). In the following instrumental response phase of 3 seconds duration, participants had to press a button as often as possible, where each button press was rewarded with money in the condition "money win" only. In the outcome phase, feedback regarding the money amount gained in the actual trial was provided. To get familiar with the task, participants completed a practice session outside the scanner. Then, participants´ individual performance was assessed in the scanner environment before the fMRI task was actually started. This information was used to calculate the individual gain per button press to standardize the total win (average gain per run: 15 €). The motivation task was adapted from Bühler and colleagues (2010).

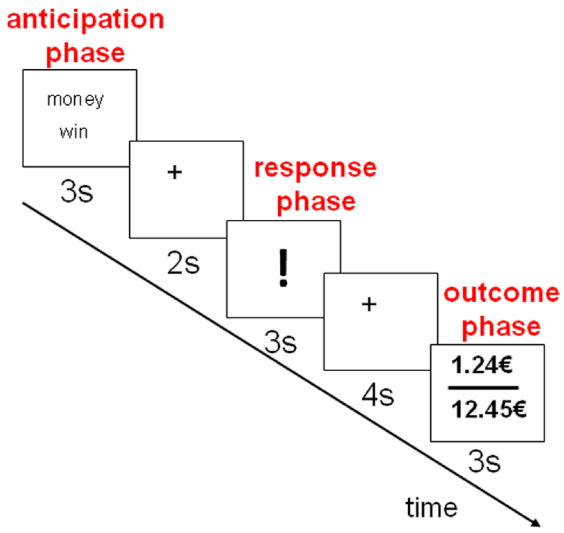

***Figure 2.7* – Event-Related Motivation-Task to Activate the NAcc.**
Adopted from (Buhler, et al. 2010).

2.4.2 Image Post-Processing

In fMRI, image post-processing involves numerous steps necessary before statistical inferences about task-related BOLD activations can be made. In this work, image post-processing was performed with the standard software package "SPM8" (http://www.fil.ion.ucl.ac.uk/spm) and included image realignment, slice-timing correction, image normalization, and spatial smoothing. Each post-processing step is briefly explained in the following sections.

2.4.2.1 Spatial Realignment

During the fMRI measurement, subject movement typically in the order of a few millimeters causes voxels at a fixed position in the brain reference frame to be mapped on different voxels in the scanner reference frame. Therefore, in the voxel-based analysis, subject movements potentially cause signal changes correlating with the stimulus onsets leading to false-positive activation. This occurs particularly in tasks where the subject has to move certain body parts (e.g. finger tapping) because the motion transfers di-

rectly to task-related head-motion. The first step to reduce such movement artifacts is to spatially realign the images. Assuming the brain as rigid body, there are 6 degrees of freedom (ndf) (i.e. ndf = 3 for translation and ndf = 3 for rotation) which are estimated by minimizing the sum of squares (*least squares*) between the respective image and an arbitrary reference image, which is often the first or the mean image of the time series. For further reduction of movement artifacts, the realignment-parameters can be used in the final statistical analysis as additional regressors (see Section 2.4.3).

2.4.2.2 Slice-Timing Correction

During the statistical analysis of the fMRI time series (see Section 2.4.3), the signal time course in each voxel is compared with a predicted BOLD signal at fixed time point. Often the acquisition times of the first (last) imaging slice are used as reference time points for which the predicted BOLD signal is modelled. Using EPI with a typical sequence timing, the temporal difference between the acquisition of the fist and the last slice is in the order of $TR/2$. Hence, for the purpose of an unbiased statistical analysis, a slice timing correction is necessary to account for the differences in the slice acquisition times. In order to make the data in each slice correspond to the same point in time, a slice dependent phase is added in the Fourier domain of the signal which, according to the shift theorem, corresponds to a temporal shift in the time domain. Physiological signal changes with a frequency higher than the Nyquist frequency of $1/(2 \cdot TR)$ cannot be recovered by this method. However, in an event-related study performed by Josephs and colleagues (1997), it has been demonstrated that no significant physiological signal changes were present at higher frequencies than the typical Nyquist frequency of $\omega^{\mathrm{Nyq}} \approx 0.25$ Hz. For simple block designed fMRI experiments, the slice time correction is often skipped because the stimulation durations are typically one order of magnitudes longer than the differences of the slice acquisition times within one imaging volume. However, considering the short neuronal responses in the order of a few seconds associated with event-related stimuli, the slice timing correction is an essential post-processing part for event-related studies.

2.4.2.3 Normalization to the MNI Space

In the 1940s, Talairach and Tournoux (1988) developed the first brain atlas based on an average brain of standard size and shape in order to locate brain areas in individuals.

Today, with respect to multi-subject analysis, spatial normalization is an essential post-processing step to locate average brain activation in a group of subjects on a voxel-by-voxel basis. In the mean time, different brain atlas are used in fMRI whereas the MNI (**M**ontreal **N**eurological **I**nstitute) brain atlas (Collins, et al. 1993), with a spatial resolution of 1.0 x 1.0 x 1.2 mm^3, is probably the most prominent one and was used in this work. In order to normalize an individual brain into MNI space, a T_1- or T_2-weighted anatomical image is acquired at the beginning or at the end of an fMRI experiment. Then, the anatomical image is registered to a T_1- or T_2-weighted template brain (e.g. provided by SPM8) by an affine transformation with 12 parameters using *least squares*. Finally, the parameters of the affine transformation are used to normalize the functional scans, in register with the structural scan acquired at the beginning of the fMRI experiment, to MNI standard space.

2.4.2.4 Spatial Smoothing

After spatial realignment and normalization to MNI space, the functional images are spatially smoothed to increase the *SNR* and thus BOLD sensitivity. Spatial smoothing corresponds to weighted averaging of voxel signal intensities and can be expressed by a convolution of the acquired image $X(\tilde{i},\tilde{j})$ and a weighting function $h(i-\tilde{i},j-\tilde{j})$, where $\tilde{i}$ and $\tilde{j}$ are fixed space coordinates (i.e. voxel positions):

$$Y(\tilde{i},\tilde{j}) = \sum_{i,j} h(i-\tilde{i},j-\tilde{j}) \cdot X(\tilde{i},\tilde{j}) \qquad 2.20$$

In this work, all datasets were smoothed with a Gaussian Kernel,

$$h(i,j) = a \cdot e^{-(i-\tilde{i})^2/2b^2} e^{-(j-\tilde{j})^2/2c^2} \quad \text{with } a,b,c \in \mathbb{R} \qquad 2.21$$

(i.e. in *x*-, *y*-, and *z*-direction) whereby the kernel size was varied depending on the focus of the respective fMRI study.

2.4.3 Statistical Analysis

Within the framework of the GLM (Friston 1996; Friston, et al. 1995), the fMRI signal time course of each voxel is statistically analyzed. It can be differentiated between the single subject analysis and multi-subject analysis. On the single subject level, statistical inference is made about BOLD activation strengths associated with a certain stimulus.

Multi-subject analysis makes inferences about the average BOLD activation within a group of subjects during a particular stimulus. Both, single subject and multi-subject analyses are performed voxel-by-voxel using the GLM which is briefly introduced in the following section.

2.4.3.1 The General Linear Model

The signal time course of a single voxel can be described by a vector y_i with N data points recorded at the time t_i, with i ϵ [1,..., N]. Each of the data points may be afflicted with the error ε_i. In the GLM, a linear combination of p regressors $X_{i,j}$ with j ϵ [1,..., p] may describe the measured time course y_i by optimizing the parameters β_i,

$$\begin{pmatrix} y_1 \\ y_2 \\ \vdots \\ y_N \end{pmatrix} = \begin{pmatrix} 1\, x_{1,1} & x_{1,2} & \cdots & x_{1,p} \\ 1\, x_{2,1} & x_{2,2} & \cdots & x_{2,p} \\ \vdots\ \vdots & \vdots & \vdots & \vdots \\ 1\, x_{N,1} & x_{N,2} & \cdots & x_{N,p} \end{pmatrix} \cdot \begin{pmatrix} \alpha \\ \beta_1 \\ \vdots \\ \beta_N \end{pmatrix}, \qquad 2.22$$

or in abbreviated form

$$\hat{y} = \hat{X}\hat{\beta} + \hat{\varepsilon}\,. \qquad 2.23$$

The matrix $\hat{X}$ is referred to as the design matrix. Equation 2.23 holds only for normally distributed errors ε_i respectively "white" noise:

$$\langle \hat{\varepsilon} \rangle = 0 \qquad 2.24$$

$$\mathrm{var}(\hat{\varepsilon}) = \sigma^2 \qquad 2.25$$

However, in fMRI datasets the noise is always non-white due to unmodelled signals related to e.g. cardiac pulsation, breathing, and subject motion. Therefore, before GLM parameter estimation is performed, the noise is pre-whitened (see Section 2.4.3.2). For the moment, it is assumed that the noise is white and the β_j-coefficients can be estimated by minimizing the sum of squared errors (*least-squares*):

$$\arg\min_{\beta_j \in \mathbb{R}} \left(\sum_{j=1}^{p} y_i - x_{i,j}\beta_j \right) \Rightarrow \hat{\beta} = \left(\hat{X}^T \hat{X} \right)^{-1} \hat{X}^T \hat{y} \qquad 2.26$$

For clearness, it is assumed that only a single regressor $\hat{X}$ is used. Then, Eq. 2.23 can be transformed to:

$$\hat{y} = \alpha + \hat{X}\beta + \hat{\varepsilon} \tag{2.27}$$

The coefficients α and β are determined by *least squares*,

$$\beta = \frac{\sum_{n=1}^{N}(x_n - \bar{x})(y_n - \bar{y})}{\sum_{n=1}^{N}(x_n - \bar{x})^2} = \frac{Cov(\hat{X}, \hat{Y})}{Var(\hat{X})}, \tag{2.28}$$

with α given by:

$$\alpha = \bar{y} - \hat{\beta}\bar{x} \tag{2.29}$$

The regressor $\hat{X}$ is given by the convolution of the step-function $\Theta(t)$ and the Hemodynamic Response Function (*HRF*) (Figure 2.8).

$$\Theta * HRF = \int \Theta(\tau) HRF(t - \tau) d\tau \tag{2.30}$$

The step-function $\Theta(t)$ is defined by the experimental paradigm and is zero during the resting states and one during the active states. As is known, the gamma variate function $\Gamma(t)$,

$$\Gamma(t) = \begin{cases} 0 & if \;\; t < \Delta t \\ \dfrac{1}{\tau n!}\left(\dfrac{t}{\tau}\right)^n e^{t/\tau} & else, \end{cases} \tag{2.31}$$

is different from the physiological *HRF* but is commonly used to model the BOLD response because it empirically fits the fMRI signal very well. In this definition, Δt denotes the delay between the stimulus and the onset of the BOLD response.

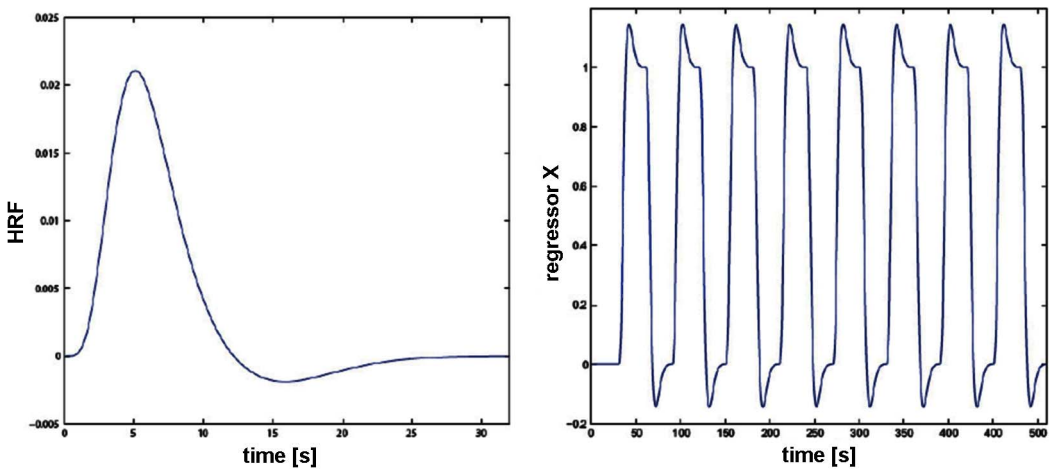

Figure 2.8 – Hemodynamic Response Function and Regressor.
(Left) Gamma variate function (left) commonly used to model the BOLD-HRF. (Right) Regressor, which is the convolution of the stimulus design and the BOLD-HRF. Source: (TheMathWorksInc 2008)

2.4.3.2 Pre-Whitening Noise

According to the GLM (see Eq. 2.23), the observed data $\vec{y}$ can be described as the product of a design matrix $\hat{X}$ with the parameter vector $\vec{\beta}$ plus and additional error vector $\vec{\varepsilon}$ with a Normal distribution $N\left(0,\sigma^2\hat{R}\right)$, with the autocorrelation matrix $\hat{R}$. The estimates of the $\vec{\beta}$-parameters are unbiased, if the autocorrelation matrix $\hat{R}$ of the residuals is equal to unity $\hat{I}$, respectively if the noise is "white". Assumed the autocorrelation matrix $\hat{R}$ is exactly known, there exists a square, non-singular matrix $\hat{K}$ such that $\hat{K}\hat{K}^T = \hat{R}$ and that $\hat{K}^{-1}\vec{\varepsilon} = \vec{\delta}$; $\vec{\delta} \sim N(0,\sigma^2\hat{I})$ (Seber 1977). Before estimating the GLM parameters, a smoothing matrix $\hat{S} = \hat{K}^{-1}$ is applied to the measured data and the design matrix $\hat{X}$ to pre-whiten the noise:

$$\hat{S}\vec{y} = \hat{S}\hat{X}\vec{\beta} + \vec{\eta}\ ; \quad \vec{\eta} \sim N(0,\sigma^2,\hat{V}) \tag{2.32}$$

If the estimation of the autocorrelation $\hat{R}$ is correct, then the filtered noise is white:

$$\hat{V} = \hat{S}\hat{R}\hat{S}^T = \hat{S}\hat{S}^{-1}(\hat{S}^{-1})^T\hat{S}^T = \hat{I} \tag{2.33}$$

Here, it is focused on the AR model to estimate the intrinsic autocorrelation of the noise to create the smoothing matrix $\hat{S}$. In the time domain, an AR(p) model of p^{th} order is expressed as,

$$z(t) = a_1 z(t-1) + a_2 z(t-2) + ... + a_p z(t-p) + w, \qquad 2.34$$

or in compact form as:

$$\vec{z} = \hat{A}\vec{z} + \vec{w} \;; \quad \vec{w} \sim N(0, \sigma^2 \hat{I}) \qquad 2.35$$

The regression coefficients a_i of the (p+1) x (p+1) lower triangular matrix $\hat{A}$ can be estimated by ordinary *least squares*. For most cases only the a_1-coefficient significantly differs from zero (Bullmore, et al. 1996). Therefore, an AR(1) model of first order is used by several authors (Bullmore, et al. 1996; Kruggel and von Cramon 1999a) to estimate the autocorrelation a_1 and the noise (σ^2) from the residuals ($\hat{z} = \hat{R}$) after fitting the GLM. Subsequently, the smoothing matrix $\hat{S} = \hat{I} - \hat{A}$ is used to pre-whiten the noise according to the Eq. 2.32 and Eq. 2.33.

2.4.3.3 Student´s *t*-Test

In fMRI, hypothesis tests are performed to determine whether a voxel was activated during a particular task. The null-hypothesis $H_0 = H(\hat{\beta}_0 \equiv 0)$ indicates that there was no activation and that the voxel time course contains only the noise $\hat{\varepsilon}$. The alternative hypothesis H_1 assumes that the voxel was activated. In this work, the so-called *t*-test (i.e. student´s *t*-test) was used to decide whether H_0 or H_1 should be refused. Under the null-hypothesis H_0, the test-variable *t* is defined as

$$t = \sqrt{n-p} \cdot \frac{\hat{\beta} - \hat{\beta}_0}{\sigma_\beta}, \qquad 2.36$$

with *p* being the number of regressors. The variance of the test-variable is *t*-distributed with ($n - p - 1$) degrees of freedom. With regard to the parameters n and $\hat{\beta}$, it must be differentiated between single subject and multi-subject analysis. On the single subject level, the parameter n is equal to the number images and the parameter $\hat{\beta}$ corresponds to the average activation strength during the stimulus determined by Eq. 2.26. In contrast, on the group level, the parameter *n* is equal to the number of subjects and the parameter $\hat{\beta}$ corresponds to the average activation strength in all subjects in the voxel of interest. A pre-defined threshold α specifies below which probability of error the alternative-hypothesis H_1 will be accepted and the null-hypothesis H_0 discarded. The critical α-value is determined on the basis of the associated α-quantile of the Student´s *t*-distribution and the critical β-parameter on the basis of Eq. 2.36. Hence, a voxel is con-

sidered to be activated, if the β-value of that particular voxel is above the threshold (i.e. $\beta > \beta^{\alpha}$). As mentioned previously, the raw functional images are spatially smoothed prior to the GLM parameter estimation to increase the *SNR*. Considering Eq. 2.36, it is obvious that higher *SNR* improves the BOLD sensitivity because in case of "true" activation the variance of the $\hat{\beta}$-estimates σ_{β} decreases and thus the *t*-value of an activated voxel increases. Figure 2.9 (a) shows a *maximum intensity projection* (MIP) of BOLD activation during a simple fingertapping experiment (i.e. the projection of the peak voxel in the respective direction). The darker the gray shades in the MIP, the higher the *t*-value of the activated voxel whereby the threshold α must be exceeded. For a voxel to be activated it was additionally requested that at least 9 neighbouring voxels were activated (i.e. cluster size $k \geq 10$). In the case that activated voxels are located in clearly non-activated brain areas, then these voxels are referred to as false-positives.

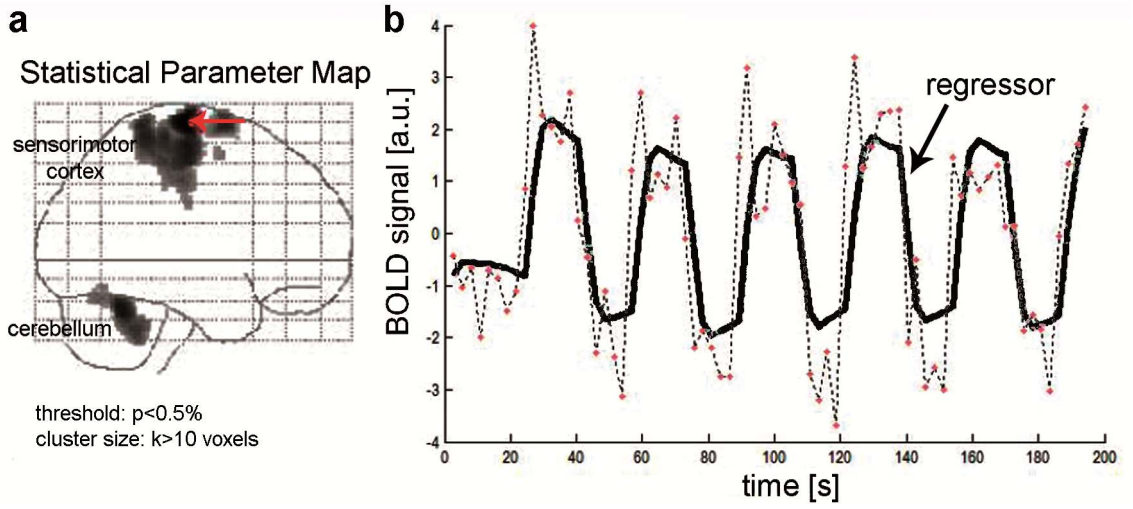

Figure 2.9 – BOLD Activation During a Simple Fingertapping Task.
*(**a**) Maximum intensity projection of a statistical parameter map. (**b**) Peak voxel time course (marked by red points) and regressor (marked by the black line). Source: (TheMathWorksInc 2008)*

2.5 T_2* and Gradient-Field Mapping

Data Acquisition

BOLD sensitivity using EPI depends on the local transversal relaxation time T_2^* and on the macroscopic in-plane and through-plane field gradients G_{sp} and G_{ss}, respectively (see Section 2.2.1.1). In order to optimize the *TE*-parameter towards maximal BOLD sensitivity, T_2* and gradient fields were measured in six healthy subjects (27 ± 1 years, five males) using a multi-gradient-echo FLASH imaging sequence (Haase, et al. 1986).

T_2*-weighted images were acquired between 5 ms and 140 ms (i.e. TE = 5 ms, 10 ms, 15 ms, 20 ms, 25 ms, 30 ms, 40 ms, 50 ms, 70 ms, 90 ms, 110 ms, 140 ms) with AC-PC section orientation. Further imaging parameters were: # slices = 40; matrix size = 64 x 64; TR = 30 ms; flip angle $\alpha = 25°$; FOV = 220 mm^2; slice thickness Δz = 2.5 mm. Within the same session, phase images were acquired using the same imaging sequence at *TE* values of 2.45 ms, 5.12 ms, 7.79 ms, 10.46 ms, and 13.13 ms. The flip angle was set to $\alpha = 12°$ but the remaining imaging parameters were kept constant. Phase-unwrapping was performed along the temporal dimension (Windischberger, et al. 2004).

Parameter Estimation

The gradient fields were estimated from the phase images. The measured phase difference $\Delta\varphi$ between adjacent voxels is proportional to the strength of the macroscopic field gradient $G_{ss/sp}$ (assumed to be constant within each voxel), the voxel dimension Δx (i.e. Δx denotes the voxel dimension in RO or PE direction), and the echo time:

$$\Delta\varphi = \gamma \cdot G_{ss/sp} \cdot \Delta x \cdot TE \qquad 2.37$$

Equation 2.37 was used to estimate G_{ss} and G_{sp} separately by *least squares* fitting. The local transversal relaxation rates were estimated from the T_2*-weighted images. For T_2^*-fitting, often a simple exponential decay (Eq. 1.36) is assumed. However, it has been shown that neglecting the additional dephasing effects of through-plane gradients G_{ss} leads to an underestimation of T_2^* (Peters, et al. 2007). In this work, Eq. 2.6 was used as fitting function for T_2^*-estimation whereby the free parameter G_{ss} was used from the gradient field mapping results based on Eq. 2.37. The confidence bounds for T_2*-fitting and gradient field mapping were set to 95 %. Voxels with a relative error of

$\Delta T_2^* / T_2^* > 0.25$ and $\Delta G_{ss/sp} / G_{ss/sp} > 0.25$ were excluded from further processing. The results of this study are presented in Section 3.1.1.

3 Results

3.1 Increasing BOLD Sensitivity using Slice-Dependent Echo Times

A slice-dependent echo time allows maximizing the BOLD sensitivity in each slice separately. Focusing on BOLD activation in the amygdala, Stoecker and colleagues (2006) showed that an EPI sequence with slice-dependent echo times improved signal detection at 1.5 T. In this work, an EPI with a slice-dependent echo time was developed to optimize the BOLD contrast in the OFC at field strength of 3 T. First, the optimal echo times were simulated for the OFC based on the T_2* and gradient-field mapping study (see Section 2.5). Finally, the optimized EPI sequence with slice-dependent echo times was compared to a standard EPI sequence with an echo time of 27 ms during fMRI using the reversal-learning task described in Section 2.4.1.2. A condensed version of this section can be found in the publication (Domsch, et al. 2013).

3.1.1 BOLD Sensitivity Simulations

Figure 3.1 shows T_2*-relaxation times below 10 ms and susceptibility gradients of more than 200 μTm^{-1} in the lower part (slice 1) of the OFC. The upper part (slice 5) of the OFC is clearly less affected by susceptibility gradients leading to increasing T_2* and decreasing susceptibility gradient values. In slice 1, T_2* was on average between 8 ± 3 ms and 31 ± 7 ms. In- (through-) plane gradients were on average in the range of -202 ± 57 μTm^{-1} (-230 ± 56 μTm^{-1}) and 288 ± 63 μTm^{-1} (214 ± 17 μTm^{-1}). In slice 5, T_2* was on average in the range of 19 ± 3 ms and 47 ± 9 ms. And in- (through-) plane gradients were on average in the range of -135 ± 61 μTm^{-1} (-209 ± 36 μTm^{-1}) and 73 ± 25 μTm^{-1} (63 ± 25 μTm^{-1}). Individual results of all subjects are summarized in Table 3.1.

Figure 3.2 shows the effect of typical susceptibility gradient strengths observed in the OFC on BOLD sensitivity. For example, given a T_2*-value of 35 ms, and a susceptibility gradient of 150 μTm^{-1} in slice or in phase encoding direction would shift the BOLD sensitivity peak from 35 ms to 4 ms or to 19 ms. Using a standard *TE*-value of 27 ms, the maximal BOLD sensitivity would reach only 87 % and 2 %, respectively.

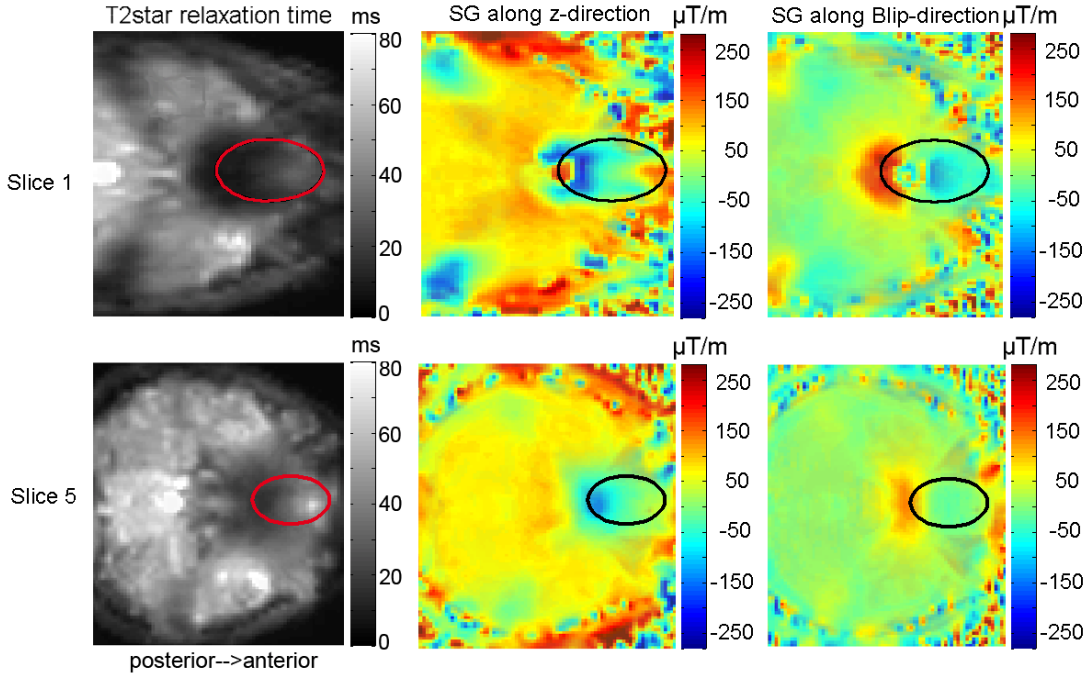

Figure 3.1 – T_2*-Relaxation Time and Field Gradient Maps in Slice and PE Direction.
The OFC is marked by the ROI. These are two axial slices acquired from a representative subject. The parameter maps are normalized to the standardized MNI-coordinates and resampled to a 96 x 96 x 40 matrix size.

Figure 3.3 depicts a simulation of the maximal *TE* values before total signal loss occurs due to in-plane gradients in the range of -350...350 µTm^{-1}. According to Eq. 2.9, the maximal *TE* value TE^{max} was defined as $TE^{max} \equiv 1/2 \cdot TA/|1-1/Q|$. It shows that a *TE* value of 22 ms prevents total signal loss for any negative in-plane gradients in the range of [-350…0] µTm^{-1} ($Q > 1$). For increasing positive gradient strengths in the range of [0…180] µTm^{-1} ($0 < Q < 1$), the maximal echo time decreases rapidly below 20 ms. In the range of [180…350] µTm^{-1} ($Q < 0$), TE^{max} slightly increases but still remains below feasible *TE* values.

Slice 1 / Subject	T_2* **[ms]**	G_{ss} **[µTm^{-1}]**	G_{sp} **[µTm^{-1}]**
1	[8 ... 32]	[-178...190]	[-124...209]
2	[10...25]	[-240...240]	[-250...186]
3	[6 ... 29]	[-250...324]	[-255...219]
4	[5 ... 32]	[-200...286]	[-214...212]
5	[11...44]	[-100...338]	[-274...239]
6	[5 ... 23]	[-243...350]	[-261...216]
mean	**[8 ± 3...31 ± 7]**	**[-202 ± 57...288 ± 63]**	**[-230 ± 56...214 ± 17]**

Slice 5 / Subject	T_2* **[ms]**	G_{ss} **[µTm^{-1}]**	G_{sp} **[µTm^{-1}]**
1	[17...58]	[-146...57]	[-34 ... 90]
2	[20...41]	[-205...43]	[-154...79]
3	[15...35]	[-257...95]	[-180...65]
4	[22...55]	[-222...48]	[-104...27]
5	[20...47]	[-212...41]	[-204...81]
6	[18...47]	[-211...92]	[-135...94]
mean	**[19 ± 3...47 ± 9]**	**[-209 ± 36...63 ± 25]**	**[-135 ± 61...73 ± 25]**

Table 3.1 – T_2*-Relaxation Times and Gradient-Fields in Two Different Slices.
The minimal and maximal parameter values denote the 5 and 95 percentiles, respectively. The standard deviation denotes the variation between the different subjects.

Figure 3.4 shows a BOLD sensitivity calculation based on Eq. 2.9 and Eq. 2.11 for typical in- and through-plane gradients. According to this simulation, a *TE* value of 20 ms is adequate to recover BOLD sensitivity for all possible combinations of through-plane gradients in the range of -350 µTm^{-1} to 350 µTm^{-1} and in-plane gradients in the range of -350 µTm^{-1} to the order of 100 µTm^{-1}. When *TE* is reduced from 40 ms to 30 ms and to 20 ms, the percentage of dead pixels (i.e. $BS/BS^{max} < 0.1$) decreases from 37 % to 32 % and to 8 % in the left hemisphere of the G_{sp}-G_{ss} plane (i.e. $G_{sp} < 0$). This echo time reduction yields nearly no effect in the right hemisphere (i.e. $G_{sp} > 0$) decreasing the percentage of dead pixels from 44 % to 43 % and to 40 %, respectively.

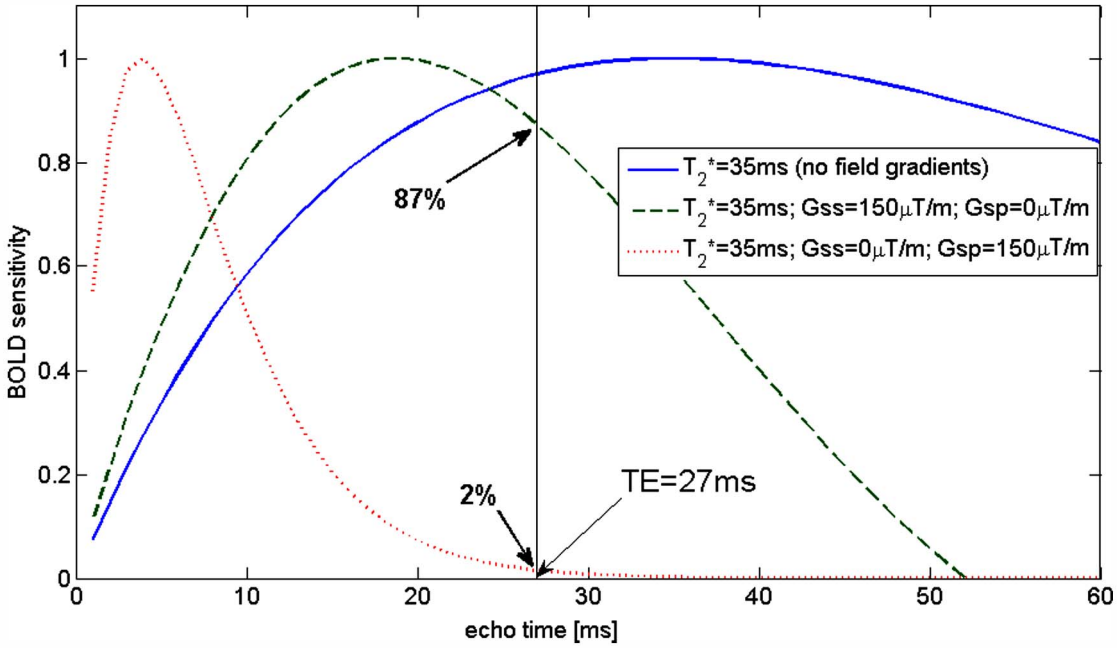

Figure 3.2 – BOLD Sensitivity as a Function of the Echo Time.
The BOLD sensitivity is depicted for typical susceptibility gradients occurring in the OFC at field strength of 3 T. The maximum is normalized to 100 %.

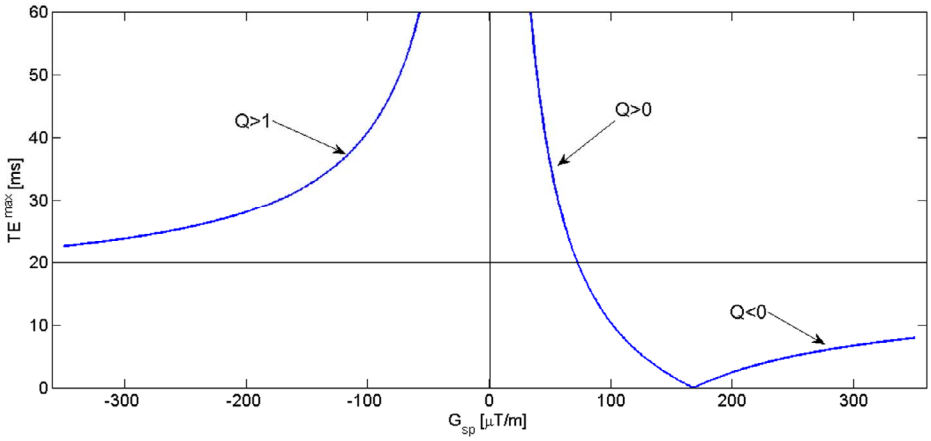

Figure 3.3 – Maximal Echo Time before Total Signal Loss Occurs.
In the presence of macroscopic susceptibility gradients in EPI PE-direction, the gradient-echo is shifted in time (see Eq. 2.8). Signal loss occurs if the echo formation is outside the signal acquisition window (see Eq. 2.9). This simulation shows the maximal echo time (TE^{max}) before total signal loss occurs. As can be seen from the curve, TE^{max} depends critically on the parameter Q (see Eq. 2.7).

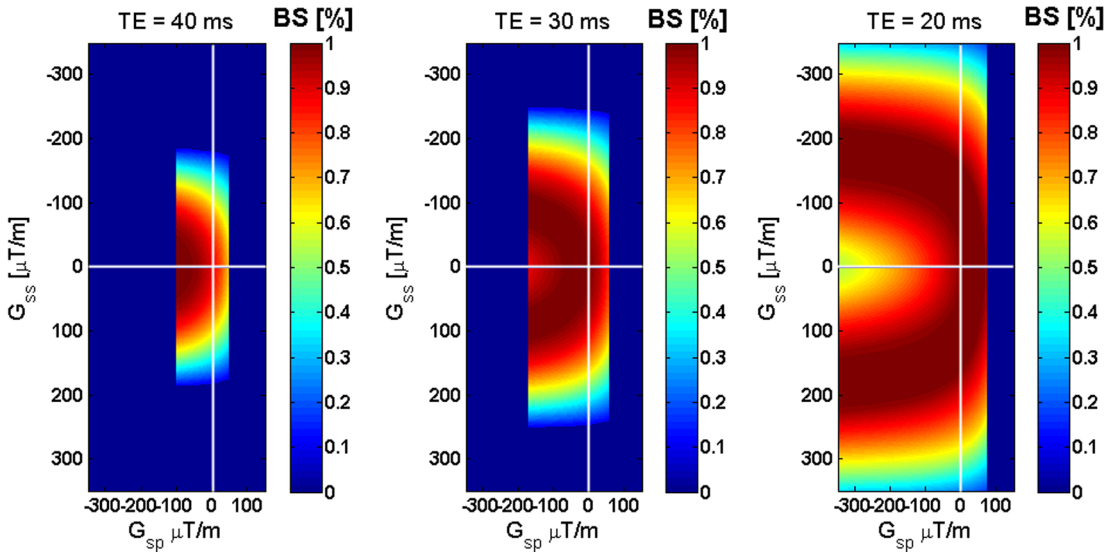

Figure 3.4 – BOLD Sensitivity Affected by Susceptibility Gradients.
The parameter maps (from left to right) are depicted for decreasing echo times of 40 ms, 30 ms, and 20 ms. The reference point at (0\|0) is indicated by the white crosshair. BS-values were calculated according to Eq. 2.9 and Eq. 2.11 assuming the following sequence parameters: T_2 = 25 ms, band-width = 1578 Hz/Px, TA = 30 ms, FOV = 220² mm², slice-thickness = 3.0 mm. The maximum was normalized to 100 % and values below 10 % were set to zero.*

For inferior axial slices, Figure 3.5 demonstrates that shortening *TE* effectively increases the BOLD sensitivity and reduces signal loss in the OFC but otherwise decreases the BOLD sensitivity in areas not affected by susceptibility gradients. For example, when *TE* is reduced from 40 ms to 30 ms to 20 ms, the percentage of dead voxels in the OFC, averaged over all subjects, decreases from 67 ± 15 % to 39 ± 16 % to 16 ± 4 %, respectively.

A calculation of the average BOLD sensitivity in the OFC in all subjects reveals that *BS* is significantly enhanced when *TE* increases with the slice number (Figure 3.6). Optimal *TE* values simulated for all subjects are depicted in Figure 3.7. The BOLD sensitivity is maximal for increasing *TE* values between 17 ± 2 ms (slice 1) and 39 ± 2 ms (slice 9) in foot-to-head direction. In areas not affected by susceptibility gradients, an optimal *TE* value of 46 ± 3 ms was measured, which is in good agreement with cortical values of about 40-50 ms (Peters, et al. 2007).

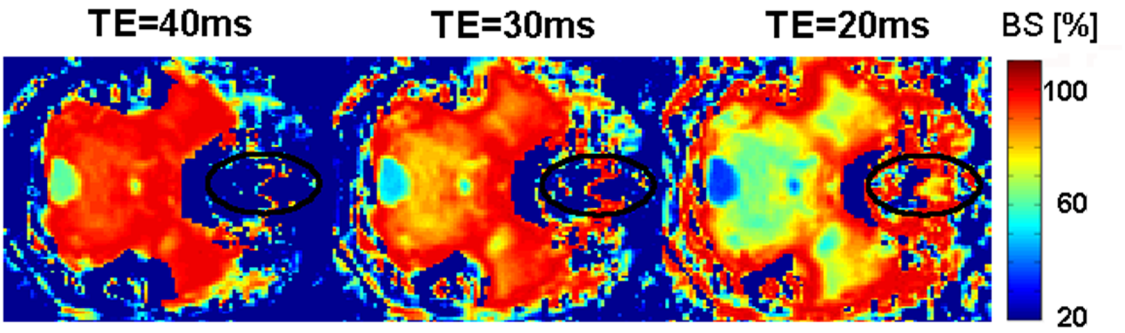

Figure 3.5 – BOLD Sensitivity Maps from a Representative Subject.
The parameter maps (from left to right) are depicted for decreasing echo times of 40 ms, 30 ms, and 20 ms. The OFC is marked by the ROI. The BOLD sensitivity maximum was normalized to 100 %.

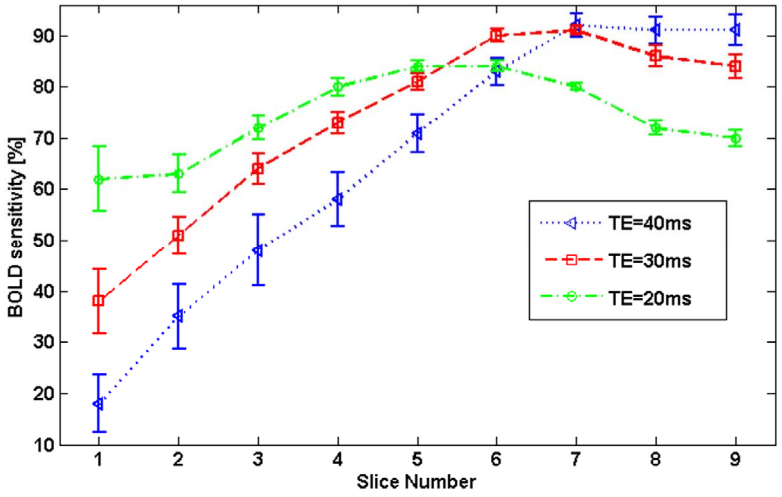

Figure 3.6 – BOLD Sensitivity in Slice Direction Measured in the OFC.
The values are depicted for decreasing echo times (i.e. 40 ms, 30 ms, and 20 ms) and were averaged over six different subjects. The errorbar denotes the standard error of the mean.

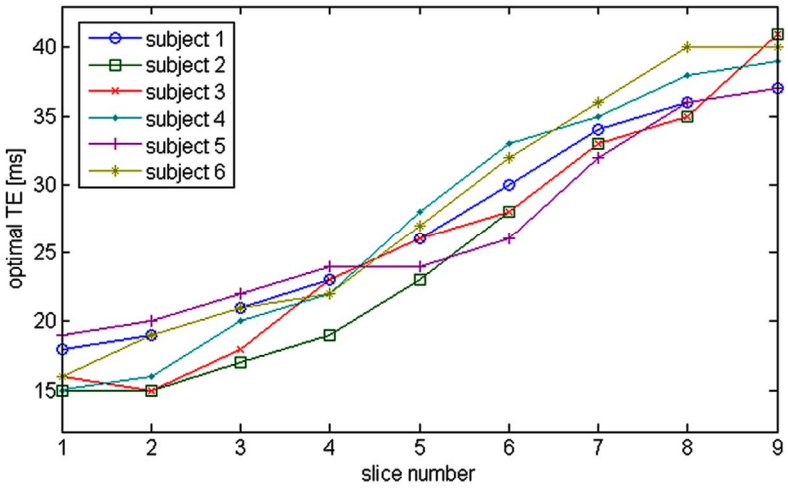

Figure 3.7 – Simulated Optimal Echo Times in the OFC in Slice Direction.
The optimal values were calculated according Eq. 2.11. T_2 and macroscopic field gradients were measured in six healthy subjects.*

3.1.2 fMRI Experiment: Reward-Reversal Study

Within an interval of 2 weeks 12 healthy participants (23 ± 3 years, six females) performed two runs of the self-paced probabilistic reward-reversal task (see Section 2.4.1.2). In the first and second run, an EPI sequence with slice dependent echo times and a standard EPI sequence with an echo time of $TE = 27$ ms was used. For time efficient volume coverage, the slices were aligned parallel to the AC-PC line (Figure 3.8). Using the modified EPI, the OFC was imaged with between 22 ms and 37 ms. In the upper slices (i.e. from slice 28 to slice 40) *TE* remained at a constant value of 47 ms. Imaging data was post-processed and analyzed according to standard procedures described in Section 2.4.2 and Section 2.4.3.

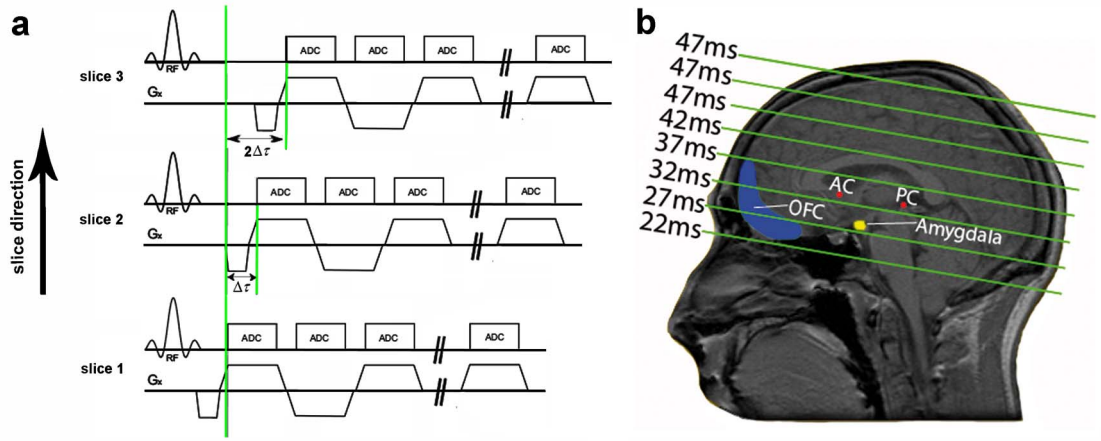

Figure 3.8 – Sequence Design and Section Orientation of the modified EPI.
*(**a**) In ascending slice direction, TE increases from 22 ms to 47 ms by shifting the EPI read out train by multiples of Δτ. (**b**) Using AC-PC section orientation, the OFC is imaged between a TE of 22 ms and 27 ms. The imaging parameters of the standard and the modified EPI sequence were: # slices = 40 (descending slice direction); matrix-size = 96 x 96; TR = 2.7 s; bandwidth = 1578 Hz/Px, flip angle = 90°; FOV = 220 mm^2; slice thickness = 2.3 mm, interslice-gap = 0.7 mm, PI-factor R = 2, PI-reconstruction: GRAPPA).*

BOLD Activation in the OFC

Figure 3.9 shows single subject data for two inferior slices acquired with a standard and a modified EPI sequence. The slices on top and bottom were acquired at *TE* of 27 ms using the standard EPI and at a *TE* of approx. 22 ms using the modified EPI sequence. The OFC shows clearly less signal loss, marked by the red arrows, when *TE* was reduced from 27 ms to 22 ms.

The single subject fMRI analysis shows OFC activation in six out of twelve participants when the standard EPI sequence was used (Table 3.2). With the modified EPI sequence, activation was detected in all participants, the average number of activated voxels increased from 87 ± 44 to 549 ± 83, and the maximal *t*-value, averaged over all subjects, increased from 4.4 ± 0.3 to 5.4 ± 0.3.

At a significance level of $p \leq 10^{-4}$ (uncorrected), a second level one-sample *t*-test revealed an average number 55 voxels to be activated in the OFC using the standard EPI sequence (Figure 3.10). At the same threshold, 553 voxels were activated when the modified EPI sequence was used. Activation in inferior and superior slices acquired at echo times below and above 27 ms was clearly more robust. Slices acquired at echo

times of about 27 ms showed similar activation in both EPI datasets. However, parietal activation was stronger at *TE* values above 27 ms showing the superiority of the modified EPI sequence. Comparing statistical inferences of both EPI sequences in a second level paired *t*-test ($p \leq 10^{-3}$ (uncorrected)) stronger activation was detected in 303 (0) voxels of the OFC when the modified (standard) EPI was used (Figure 3.11).

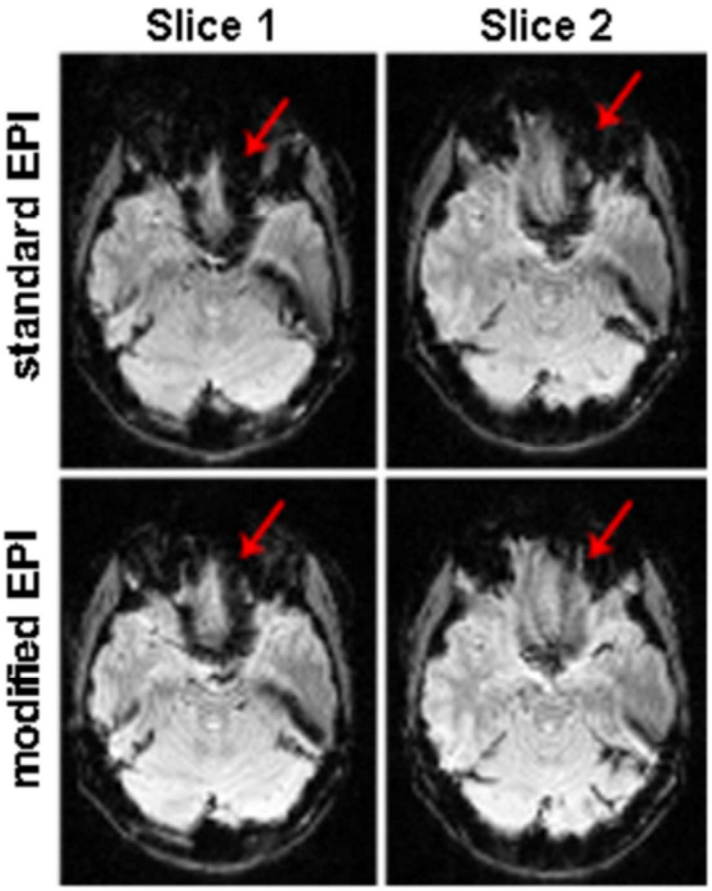

Figure 3.9 – Reduced Signal Drop Out in the OFC using the modified EPI Sequence.

	Standard EPI		EPI with Slice-Dependent *TE*	
subject	***N***	T^{max}	***N***	T^{max}
1	201	3.8	289	4.4
2	108	4.4	359	4.8
3	526	6.3	609	6.0
4	0	-	461	5.1
5	67	3.6	127	3.9
6	0	-	1054	6.5
7	0	-	377	4.6
8	0	-	695	4.9
9	77	5.0	630	5.9
10	0	-	243	4.8
11	50	3.4	873	6.4
12	0	-	866	7.3
Mean	**87 ± 44**	**4.4 ± 0.3**	**549 ± 83**	**5.4 ± 0.3**

Table 3.2 – BOLD Activation in the OFC using the Standard and the Modified EPI.
The number of significant voxels (N) and maximal t-values (T^{max}) detected in the OFC are depicted for each subject. The results are displayed at a threshold of $p \leq 5 \cdot 10^{-3}$ (uncorrected). The minimal cluster size was set to 15 voxels. The error denotes the standard error of the mean.

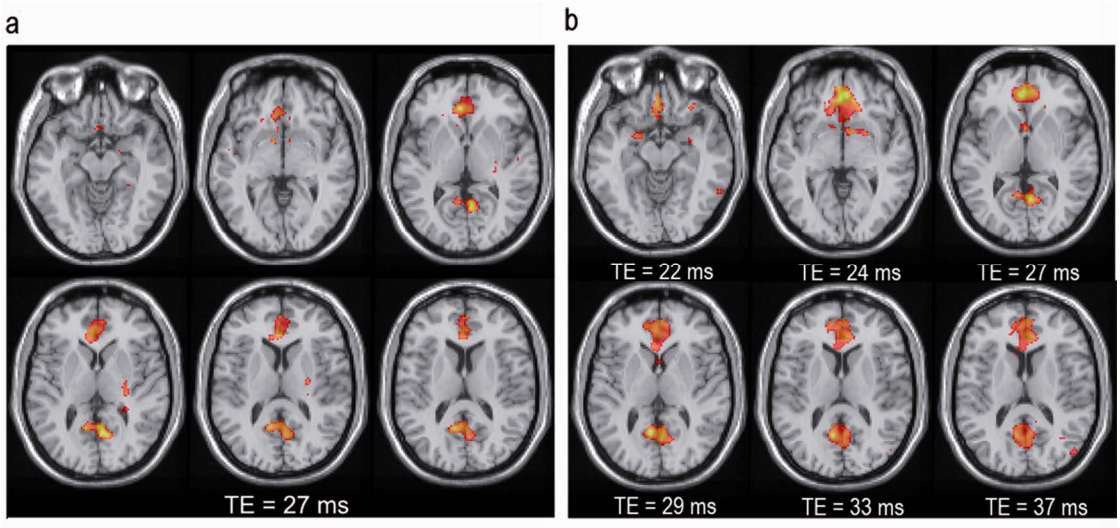

Figure 3.10 – BOLD Activation in the OFC: Standard vs. Modified EPI Sequence.
*In this representation, the parameter maps for the standard EPI (**a**) and the modified EPI (**b**) are in alignment with AC-PC according to the slice orientation during image acquisition. Thus, each slice shown here was acquired at a distinct echo time given in the figure. The maps were overlaid on structural T_1-weighted images. Robust orbitofrontal and parietal activation was detected at a threshold level of $p \leq 10^{-4}$ (uncorrected). The minimal cluster size was set to 15 voxels. The left hemisphere is displayed on the left.*

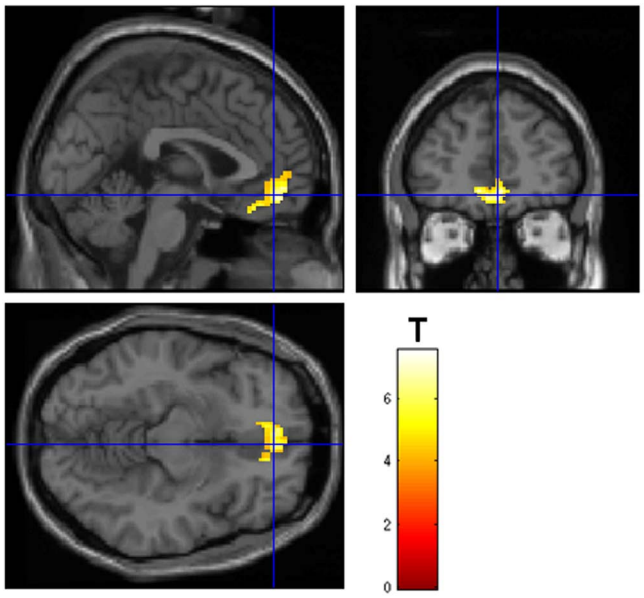

Figure 3.11 – Improved BOLD Activation in the OFC using Slice-Dependent Echo Times.
Paired t-test results displayed at a threshold of $p \leq 10^{-3}$ (uncorrected) and a minimal cluster size of 15 voxels. Colored pixels indicate that the BOLD activation in the modified EPI datasets was on average stronger than the activation in the standard EPI datasets. The left hemisphere is displayed on the left.

3.2 Improving Spatial Specificity in EPI using Parallel Imaging

The goal was to investigate the feasibility of fMRI at high spatial specificity using EPI with large matrix sizes in combination with high PI-factors. First, *PSF*-simulations and resolution-phantom measurements were performed. EPI protocols with different spatial resolutions were then tested in two separate fMRI studies. During a simple motor-task experiment, BOLD activation in the SMC was studied for increasing matrix sizes (and corresponding PI factors) between 96 x 96 (R = 2) and 192 x 192 (R = 4). A sophisticated motivation-task study was performed to study the BOLD activation in the NAcc using a standard 96 x 96 (R = 2) and a high-resolution 160 x 160 (R = 3) EPI protocol. The BOLD spatial specificity was assessed by the number of distinguishable activation clusters and local maxima as a surrogate and further examined using the proposed edge-sharpness measure. This study was carried out within the framework of the minor project part of the SFB 636 Graduate Program.

3.2.1 Point-Spread Function Simulation

First of all, it was investigated whether the spatial resolution in EPI can be theoretically increased beyond a conventional voxels size of $\Delta x \geq 2$ mm in PE direction. Blurring results from T_2*-dephasing during the EPI read out intrinsically limiting the spatial resolution. The T_2*-relaxation time strongly depends on the location within the human brain. At a field strength of 3 T, T_2*-values range between 26 ms in the OFC (Buhler, et al. 2010) and 66 ms in gray matter (de Zwart, et al. 2004). Hence, the duration of the EPI signal RO is in the order of the T_2*-relaxation time leading to non-negligible weighting of the acquired *k*-space data (Figure 3.12).

Neglecting detrimental effects of macroscopic field inhomogeneities causing signal dropouts and image distortions (Gelman, et al. 1999), the simulated *PSF* can be depicted in Figure 3.13. For T_2*-values of 20 ms, 35 ms, and 50 ms, the effective spatial resolution (i.e. *FWHM* of the *PSF*) in PE direction was 1.5 mm, 1.3 mm, and 1.2 mm, respectively. The *FWHM* decreased rapidly for increasing T_2*-values between 20 ms and 40 ms while for higher T_2*-values of more than 60 ms, the *FWHM* nearly remained at a

constant value of 1.1 mm. The spread of the *PSF* in RO direction (not shown) was negligible due to the fast signal acquisition in that direction.

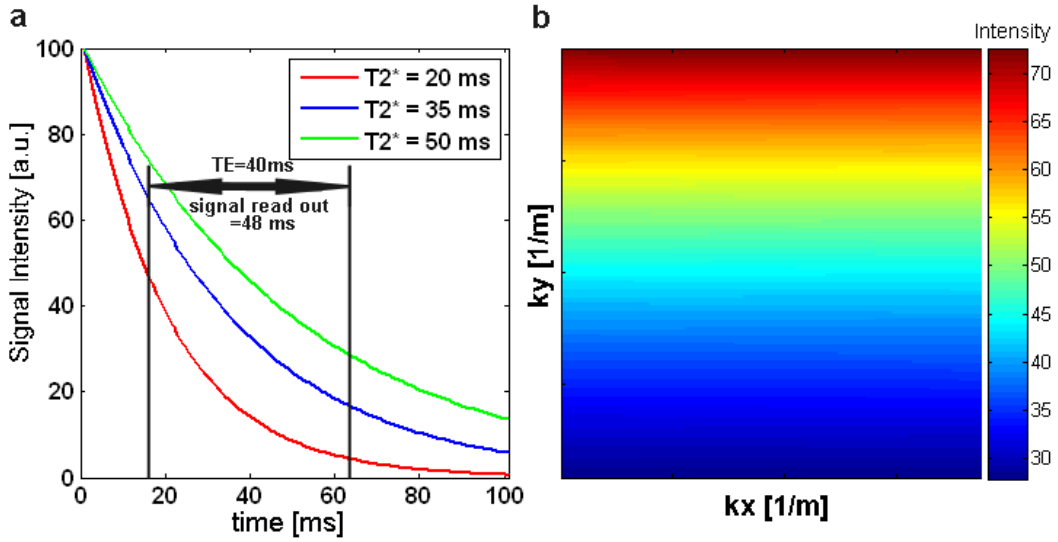

Figure 3.12 – K-space Weighting in EPI due to T_2*-Relaxation.
*Signal decay during GE-EPI RO (**a**) shown for three typical T_2*-relaxation times in the brain. The duration of the signal RO was assumed to be 48 ms corresponding to typical EPI parameters: (e.g. matrix-size = 96 x 96, BW = 1000 Hz/Px, PI-factor R = 2). The echo time was set to TE = 40 ms. K-space weighting function (**b**) is plotted as a 192 x 192 matrix assuming a T_2* value of 50 ms. A standard EPI k-space trajectory was assumed beginning at ($-k_x^{max}$, $+k_y^{max}$) and ending at ($+k_x^{max}$, $-k_y^{max}$).*

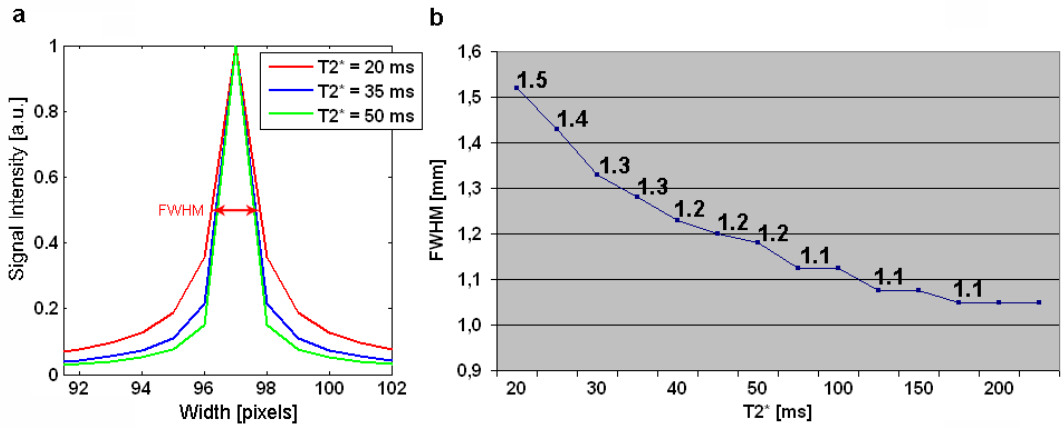

Figure 3.13 – Spatial Point-Spread Function Simulated for a Standard EPI Sequence.
*The PSF in PE direction (**a**) is shown for three different T_2*-relaxation rates. The FWHM (**b**) is depicted for T_2*-relaxation times in the range of 20 ms to 225 ms.*

3.2.2 Phantom Measurements

A structural phantom with bores of different diameters between 1 mm and 13 mm was used to evaluate the image quality at increasing matrix sizes in combination with higher PI factors keeping the sequence timing constant (i.e. *TE* and *TR*). The phantom was filled with distilled water and $NiSO_4$ resulting in a transversal relaxation rate of $T_2^* = 130$ ms.

Focussing on spatial aliasing artifacts solely and not on spatial resolution, Figure 3.14 shows a representative slice of the resolution-phantom without bores. It can be seen from the images itself and particularly from the line profiles in PE direction, that the image quality was improved when the matrix size (PI-factor) was increased from 96 x 96 (R = 2) to 128 x 128 (R = 3) and to 160 x 160 (R = 3). By further increasing the matrix size to 192 x 192 and the PI-factor to R = 4, the noise level obviously increased. Severe aliasing was present at higher PI-factors of $R \geq 5$. Therefore, the PI-factor was limited to $R \leq 4$ for all measurements.

Higher spatial resolution can be seen in the phantom images (Figure 3.15) when the matrix size was increased from 96 x 96 (R = 2) to 128 x 128 (R = 3) and to 192 x 192 (R = 4). Appropriately contrasted, moderate aliasing can be seen at any matrix size (PI factor). Regarding the line profile in PE direction shows that the smallest bores with diameters of 1.0 mm, 1.2 mm, and 1.5 mm could not be spatially resolved using the 96 x 96 (R = 2) but using the 128 x 128 (R = 3) and the 192 x 192 (R = 4) matrix sizes. It can be seen that the line profile in RO direction was superior in the 192 x 192 (R = 4) dataset. Averaged over ten different slices, the *FWHM* of the line-profiles in PE direction decreased from 2.5 ± 0.3 mm to 2.0 ± 0.2 mm when the matrix size was increased from 128 x 128 (R = 3) to 192 x 192 (R = 4) (Table 3.3).

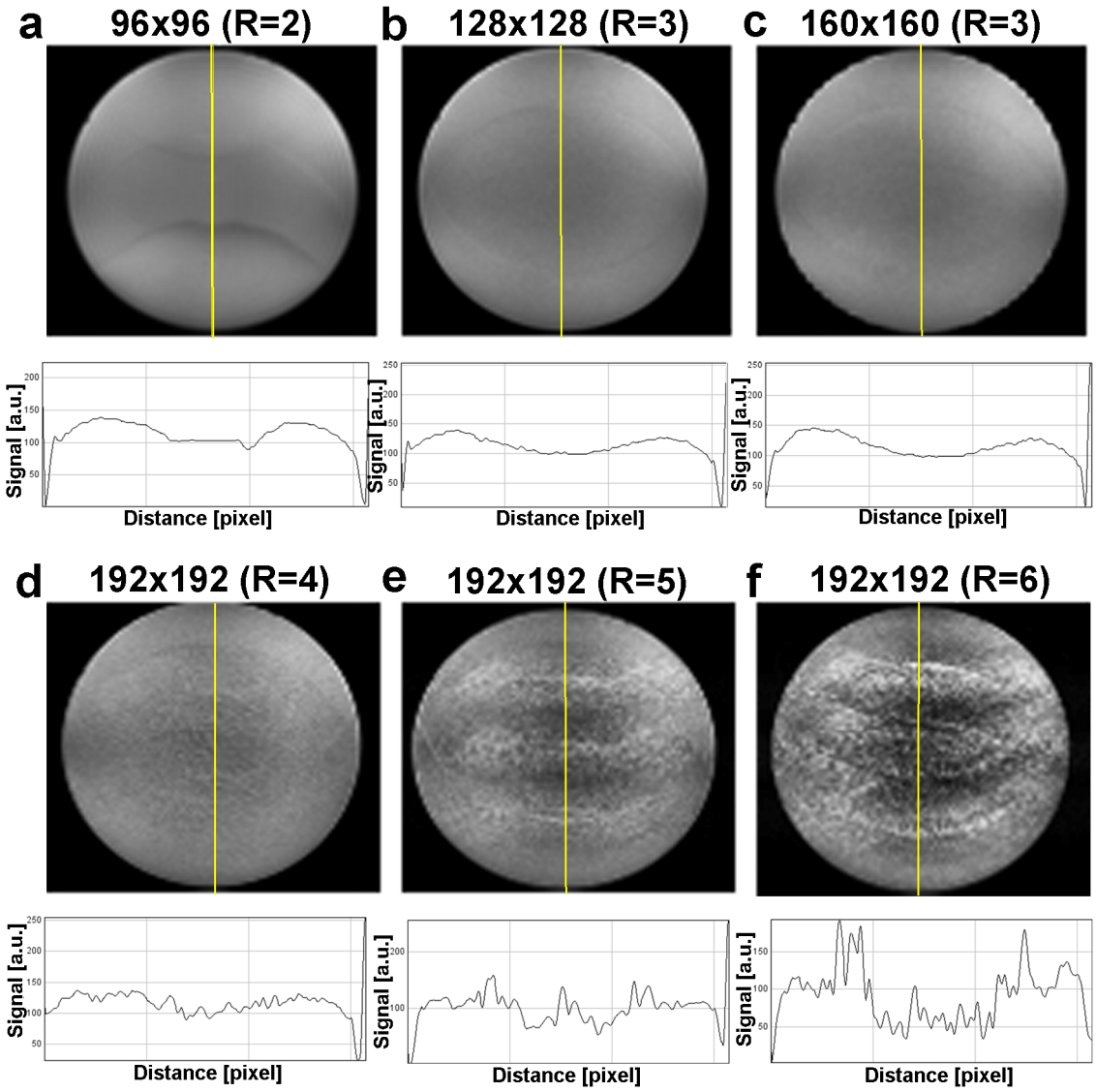

Figure 3.14 – Phantom Measurements using EPI with Increasing Matrix Sizes (PI-Factors).
*Mean images (N = 10) acquired at matrix sizes (PI-factors) of 96 x 96 (R = 2) (**a**), 128 x 128 (R = 3) (**b**) 160 x 160 (R = 3) (**c**), 192 x 192 (R = 4) (**d**), 192 x 192 (R = 5) (**e**), and 192 x 192 (R = 6) (**f**). Each image was individually contrasted emphasizing blurring and aliasing artifacts. Line profiles along the yellow lines parallel to the PE direction are shown below each phantom image. Imaging parameters: repetitions = 10, TE/TR = 35/2700 ms, FOV = 210 x 210 mm^2, # slices = 36, slice-thickness Δz = 3 mm, BW = 1002 Hz/Px. PI-reconstruction: GRAPPA (see Section 2.3.1).*

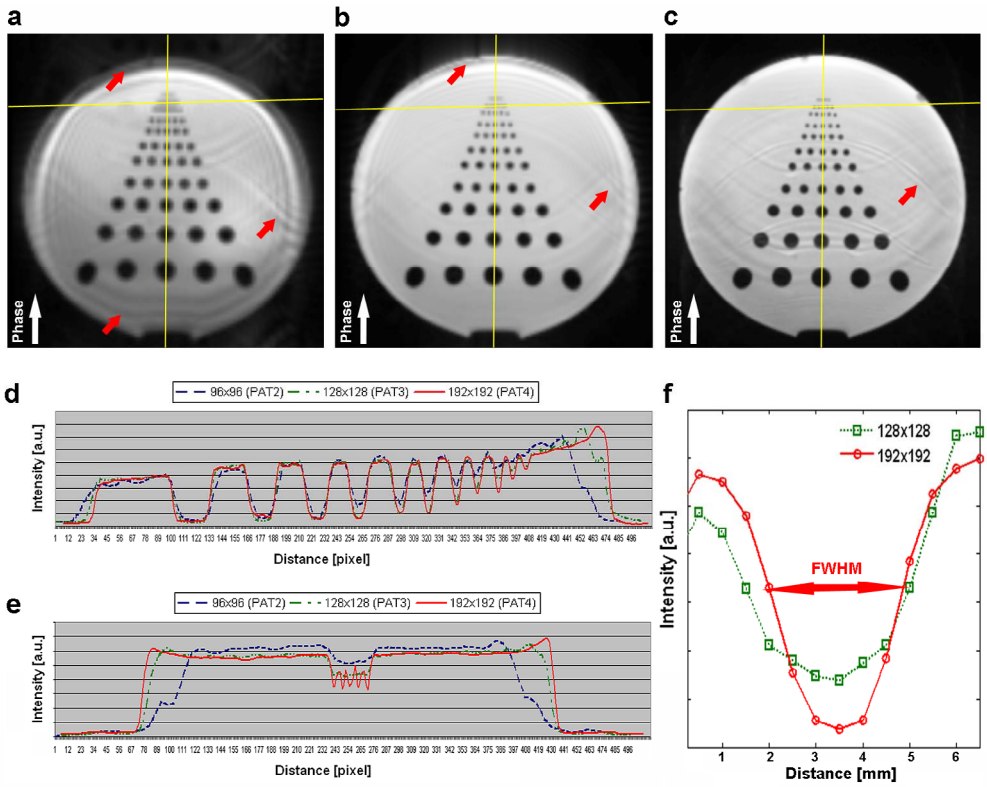

Figure 3.15 – Improved Spatial Resolution using Optimized EPI Protocols.
*Mean images (N = 10) acquired at matrix sizes (PI-factors) of 96 x 96 (R = 2) (**a**), 128 x 128 (R = 3) (**b**), and 192 x 192 (R = 4) (**c**). Each image was individually contrasted emphasizing blurring and aliasing artifacts marked by the red arrows. The line profiles in PE (**d**) and RO direction (**e**) are marked by the yellow crosshairs (**a-c**). Line profile in PE direction (**f**) across a bore with a diameter of 1.0 mm. Imaging parameters: repetitions = 10, TE/TR = 35/2700 ms, FOV = 210 x 210 mm^2, # slices = 36, slice-thickness Δz = 3 mm, BW = 1002 Hz/Px. PI-reconstruction: GRAPPA (see Section 2.3.1).*

Slice	1	2	3	4	5	6	7	8	9	10	Mean ± Std. Dev
128 x 128 (R = 3)	2.3	2.3	2.3	2.8	2.8	2.2	2.3	2.3	2.3	2.8	**2.5 ± 0.3**
192 x 192 (R = 4)	1.7	1.7	1.7	2.2	2.2	1.7	1.7	2.2	1.8	2.0	**2.0 ± 0.2**

Table 3.3 – Spatial Resolution in a Structural-Phantom using EPI.
FWHM of the line profile along the smallest bore with a diameter of 1.0 mm depicted for the 128 x 128 (R = 3) and the 192 x 192 (R = 4) matrix sizes. The FWHM was measured in PE direction in ten different slices.

3.2.3 fMRI Experiment I: Fingertapping Study

Data Acquisition and Processing

Four runs of a bilateral fingertapping task with a total duration of 4 min 30 s were performed by six healthy subjects (24 ± 3years, 3 females). The block designed paradigm consisted of 10 active and 10 rest periods with a duration of 13.5 s each. 105 EPI image volumes were acquired with four different EPI protocols per run (in randomized order) using different matrix sizes and PI-factors, while keeping the sequence timing constant. A high-resolution T1-weighted 3D image was acquired for each subject to detect potential morphological abnormalities in individuals. The matrix sizes (PI-factors) were 96 x 96 (R = 2), 128 x 128 (R = 3), 160 x 160 (R = 3) and 192 x 192 (R = 4). The sequences shared the following EPI imaging parameters: *TR*/*TE* = 2700/35 ms, repetitions = 105, *FOV* = 210 x 210 mm^2, # slices = 36, slice thickness Δz = 3 mm, interslice gap = 1.5 mm, bandwidth = 1002 Hz/Px. The images were post-processed and statistically analyzed according to the methods described in Section 2.4.2 and Section 2.4.3. The images were normalized and resampled to a voxel size of 1.0 x 1.0 x 1.0 mm^3 and spatially smoothed with a Gaussian kernel size at *FWHM* of 3.2 x 3.2 x 3 mm^3. The conditions of interest were "tapping" versus implicit baseline.

Algorithm for Cluster Sharpness Analysis

The edge-sharpness of activated clusters detected in the SPM activation maps was assessed to reflect the BOLD spatial specificity in eight different region-of-interests (ROIs) in the SMC per subject in the fingertapping data (Figure 3.16 (a)). In four adjacent slices, the different ROIs with a size of 30 x 30 pixels (1 pixel = 1.1 mm^2) were chosen to cover the left and the right SMC separately. For each ROI, the activation profiles (*t*-profiles) were analyzed for each column and each line parallel to the PE and RO direction, respectively, resulting in a total number of 480 *t*-profiles. Activation was considered to be a cluster if the activation profile exhibited one maximum above the threshold level and one minimum below the threshold level on each side of the maximum (Figure 3.16 (b)). The edge-sharpness (*S*) was defined as the absolute value of the mean slope of the cluster profile between the threshold level (α) and half-maximum (*HM*) $t^{HM}(x) = \alpha + dT$, with $dT \equiv \frac{1}{2} \cdot (T^{max} - \alpha)$. Activation below the threshold level of $\alpha = 3.1$, which corresponds to a statistical error of $p < 1‰$ in single subjects (*n.d.f.* = 88), was considered as noise. Hence, with the variables defined in Figure 3.16, the edge-sharpness is given by $S = 1/2 \cdot |dT / (x_2 - x_1)| + 1/2 \cdot |dT / (x_4 - x_3)|$. For single subjects, the

edge-sharpness comparison was performed only for those clusters that were activated in all datasets. In more detail, the edge-sharpness of an activated cluster was only compared, if the locations of the activation peaks (i.e. T^{max}-values) were within the range of the *FWHM* of the cluster detected in the 96 x 96 (R = 2) dataset (i.e. between x_2 and x_3).

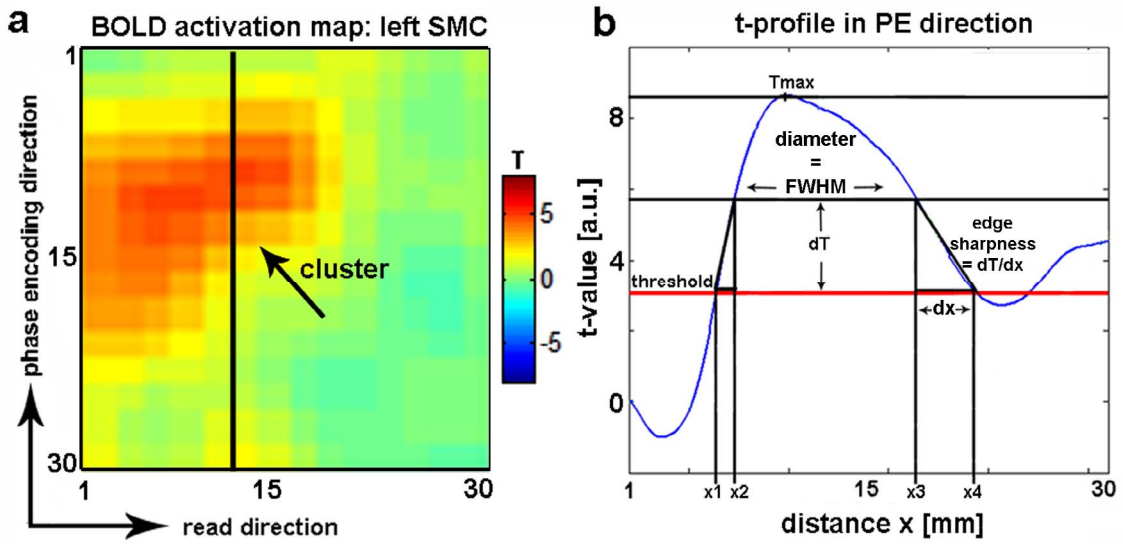

Figure 3.16 – Activation Profiles Analysis of Clusters Detected in the SMC.
*Activation map (**a**) (30 x 30 pixels) obtained from a single subject who performed a fingertapping task using the 96 x 96 (R = 2) EPI protocol. Activation profile (**b**) along the vertical black line, shown in (**a**), parallel to the EPI phase encoding direction.*

3.2.3.1 Single Subject Analysis

Figure 3.17 shows that the in-plane resolution was continuously improved when the matrix size (PI-factor) was increased using the 12-channel head coil. Despite increasing PI-factors, no PI artifacts can be seen. The comparison between the EPI images and a high-resolution (320 x 320 pixels) T_2-weighted image (Fig. 3e) reveals that the highest structural similarity was achieved using the 192 x 192 (R = 4) EPI protocol. By increasing the matrix size (PI-factor), the correlation between the EPI and the high-resolution image was continuously increased (Figure 3.17 (f)). By using the 192 x 192 (R = 4) compared to the 96 x 96 (R = 2) EPI protocol, the correlation coefficient in PE (RO) direction increased from 84 % (82 %) to 91 % (97 %), respectively.

Figure 3.18 exemplarily shows that robust BOLD activation was detected in the SMC using both the 96 x 96 (R = 2) and the 192 x 192 (R = 4) EPI protocol. It is obvious that the BOLD activation is visually less blurred and spatially more separable in terms of more activated clusters and local maxima using the 192 x 192 (R = 4) EPI protocol.

Figure 3.19 shows that the T^{max}-values (Figure 3.19 (a)) in the SMC were slightly increased in the 96 x 96 (R = 2) and 128 x 128 (R = 3) datasets compared to the 160 x 160 (R = 3) and 192 x 192 (R = 4) datasets. The T^{max}-value was decreased by 8 % in the 96 x 96 (R = 2) compared to the 192 x 192 (R = 4) datasets. However, the average number of activated voxels (Figure 3.19 (b)) was continuously decreased by 42 %, 16 %, and 22 % when the matrix size (PI-factor) was increased from 96 x 96 (R = 2) to 128 x 128 (R = 3), to 160 x 160 (R = 3), and to 192 x 192 (R = 4), respectively. The inter-subject variability of the average T^{max}-values and the number of activated voxels was continuously decreased using higher matrix sizes (PI-factors). Increasing the matrix size (PI-factor) from 96 x 96 (R = 2) to 192 x 192 (R = 4) led to a reduction of the relative error of the T^{max}-value from 11% to 5 %. Furthermore, the relative error of the number of voxels was decreased from 36 % to 20 %.

Figure 3.20 reveals that for lower thresholds the highest number of activated clusters (Figure 3.20 (a)) and local maxima (Figure 3.20 (b)) was detected in the 192 x 192 (R = 4) datasets while the lowest numbers were detected in the 96 x 96 (R = 2) datasets. At a threshold of $p < 2.5$ % (uncorr., $k \geq 30$), the number of clusters was increased by 50 % and the number of local maxima by 74 % by increasing the matrix size (PI-factor) from 96 x 96 (R = 2) to 192 x 192 (R = 4). However, all datasets show a similar number of clusters and local maxima at higher threshold levels. The cluster and local maxima separability in the 128 x 128 (R = 3) and the 160 x 160 (R = 3) datasets was almost the same at any threshold level.

Figure 3.21 (a) shows BOLD activation in the SMC of a representative subject detected at increasing matrix sizes (PI-factors). Even though the BOLD activation becomes more separable, no obvious improvement of the edge-sharpness of the clusters can be noticed. The quantitative cluster shape analysis performed for all subjects (Fig. 7b) confirms that there was no trend to increased edge-sharpness for increased matrix sizes (PI-factors). It can be seen for all datasets that the cluster were sharper in RO than in PE direction.

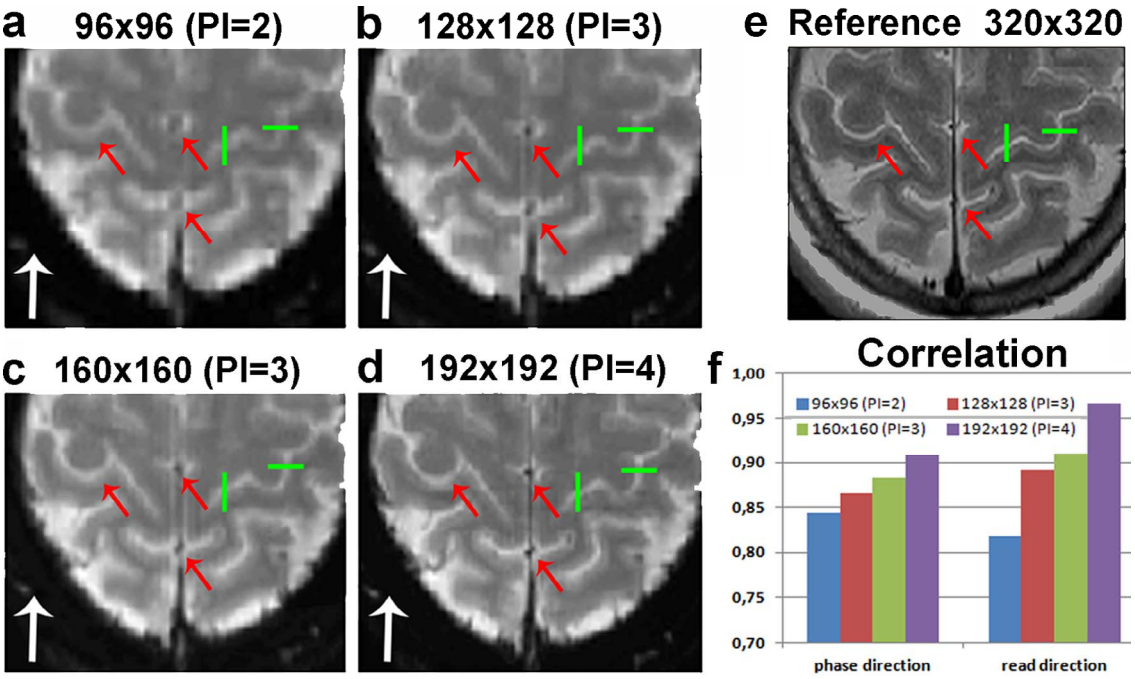

Figure 3.17 – Axial EPI Slices Acquired at Increasing Matrix Sizes (PI-factors).
*EPI time series averages (N = 100) from a representative subject acquired during the fingertapping experiment using a 12-channel head coil. The EPI matrix sizes (PI-factor) (**a-d**) were 96 x 96 (R = 2), 128 x 128 (R = 3), 160 x 160 (R = 3), and a 192 x 192 (R = 4), respectively. The EPI phase encoding direction is marked by the white arrows. Conspicuous structural differences between the images are marked by the red arrows. For comparison, the same slice displayed was acquired at a matrix size of 320 x 320 using a high-resolution spin-echo sequence (**e**). Signal profiles were compared along the PE (RO) direction, indicated by the green vertical (horizontal) line. (**f**) Correlation coefficients between signal profiles in the EPI and in the high-resolution image. For a fair comparison, the EPI images in (**a-d**) were resampled to a 320 x 320 matrix size using bilinear interpolation.*

3.2.3.2 Group Analysis

Figure 3.18 shows that robust BOLD activation was detected in the SMC using both the 96 x 96 (R = 2) and the 192 x 192 (R = 4) EPI protocol. The BOLD activation appears less blurred and spatially more separable in terms of more activated clusters and local maxima using the 192 x 192 (R = 4) EPI protocol.

Figure 3.19 shows a clear trend to increased T^{max}-values (Figure 3.19 (c)) and numbers of activated voxels (Figure 3.19 (d)) comparing the 128 x 128 (R = 3), 160 x 160 (R = 3), and 192 x 192 (R = 4) datasets. It should be noted that the BOLD activation in

the 96 x 96 (R = 2) dataset was more robust to threshold variations compared to the 128 x 128 (R = 3) dataset, revealing 18 % higher T^{max}-values and 100 % more activated voxels. Moreover, in the 96 x 96 (R = 2) datasets, the number of voxels was increased by 32 % compared to the 160 x 160 (R = 3) datasets. However, when the 192 x 192 (R = 4) EPI protocol was used, the T^{max}-values (numbers of activated voxels) was increased by 41 % (37 %) compared to the 96 x 96 (R = 2) EPI protocol.

Figure 3.20 shows that the highest number of clusters was detected in the 192 x 192 (R = 4) datasets while the lowest number of clusters were detected in the 96 x 96 (R = 2) datasets (Figure 3.20 (c)). With respect to the numbers of local maxima (Figure 3.20 (d)), on average the highest number was again found in the 192 x 192 (R = 4) EPI protocol whereas the lowest number of local maxima was detected in the 128 x 128 (R = 3) dataset at nearly all thresholds. However, the 128 x 128 (R = 3) datasets exhibited distinctly the highest number of local maxima compared to the remaining datasets at the particular threshold level of $p < 2.5$ % (uncorr.). At this threshold, the number of clusters and local maxima were both increased by 167 % and 35 %, respectively, by using the 192 x 192 (R = 4) compared to the 96 x 96 (R = 2) EPI protocol. Moreover, using the 160 x 160 (R = 3) compared to the 128 x 128 (R = 3) protocol did not improve the detectability of activated clusters or local maxima. In the context of threshold optimization, it is important to note that the number of activated clusters and local maxima were generally decreased using higher threshold levels.

Figure 3.21 (c) displays the increased edge-sharpness with increasing matrix size (PI-factor). Accordingly the edge sharpness was continuously improved in the quantitative cluster shape analysis (Figure 3.21 (d)). Comparing the 96 x 96 (R = 2) and the 192 x 192 (R = 4) datasets, the edge-sharpness in PE (RO) direction was increased by 100 % (119 %). However, there was no statistically significant difference in the edge-sharpness along the PE direction between the 128 x 128 (R = 3) and the 160 x 160 (R = 3) datasets.

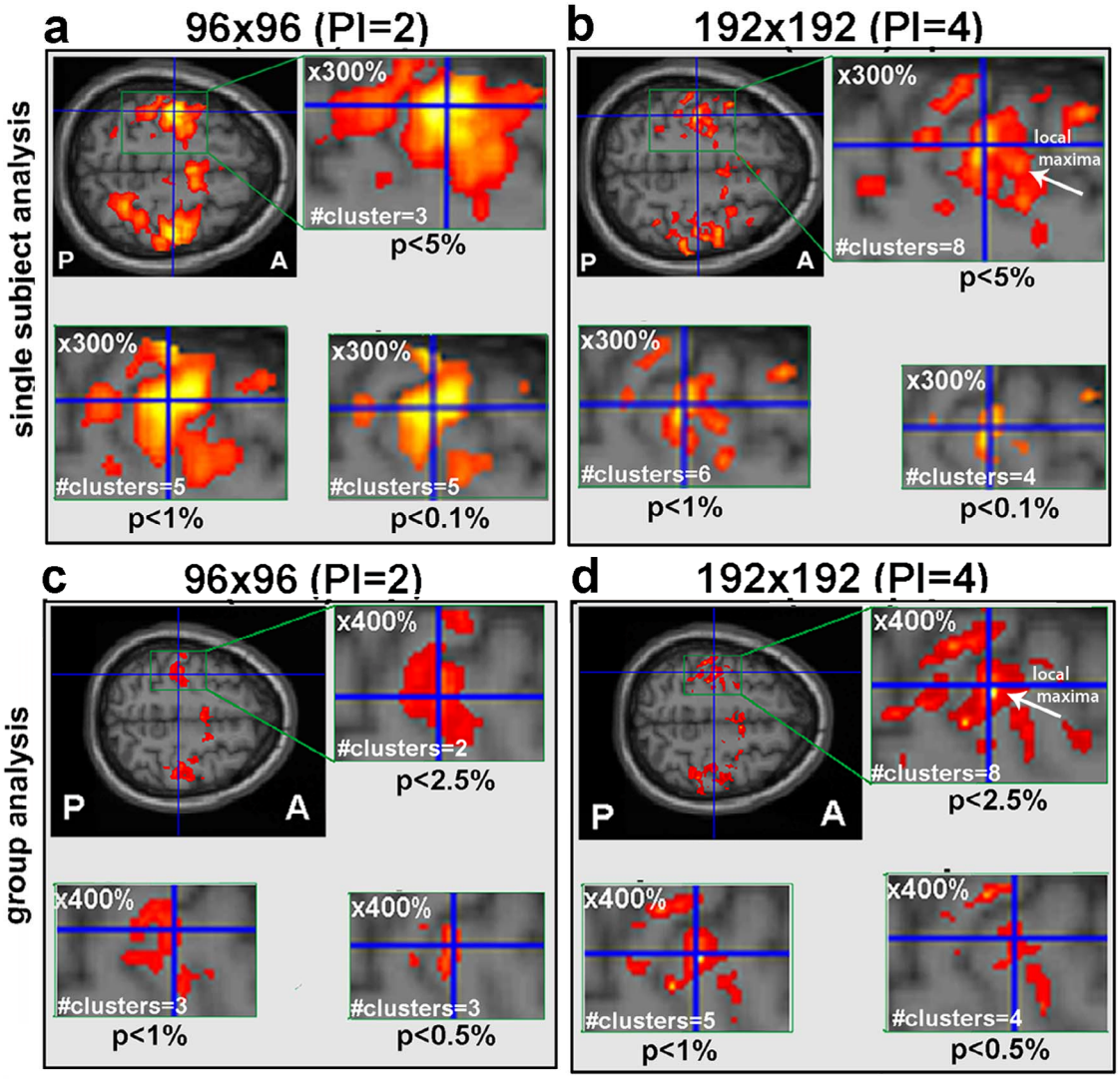

Figure 3.18 – BOLD Activation Measured with EPI at Different In-Plane Resolutions.
*Single subject (**a-b**) and group activation (**c-d**) in the SMC during a bilateral fingertapping task (N = 6) depicted for three different statistical thresholds. The blue crosshair marks the peak voxel in each dataset while the white arrow points at a local maximum. The activation maps are depicted in MNI-space and were superimposed on a T1-weighted structural image.*

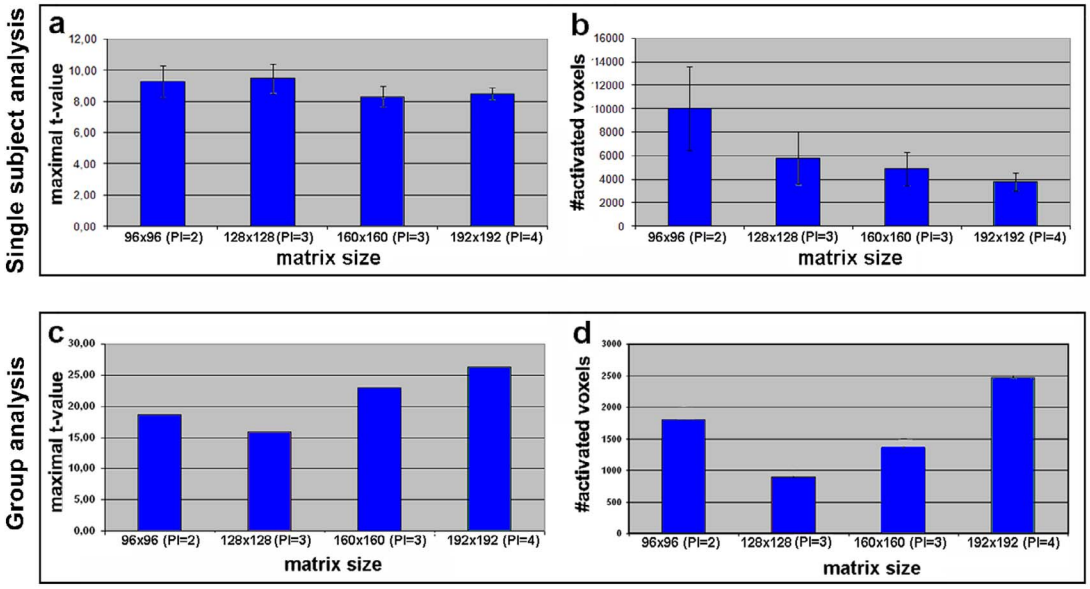

Figure 3.19 – Fingertapping fMRI Analysis using EPI with Increasing Spatial Resolution.
*Average T^{max}-values (**a**) and number of activated voxels (**b**) in the SMC detected on the single subject level during a fingertapping task (N = 6). T^{max}-values (**c**) and number of activated voxels (**d**) detected on the group level. The results were obtained at a statistical threshold of p < 1 % (uncorrected) and a minimal cluster size of k ≥ 30 voxels.*

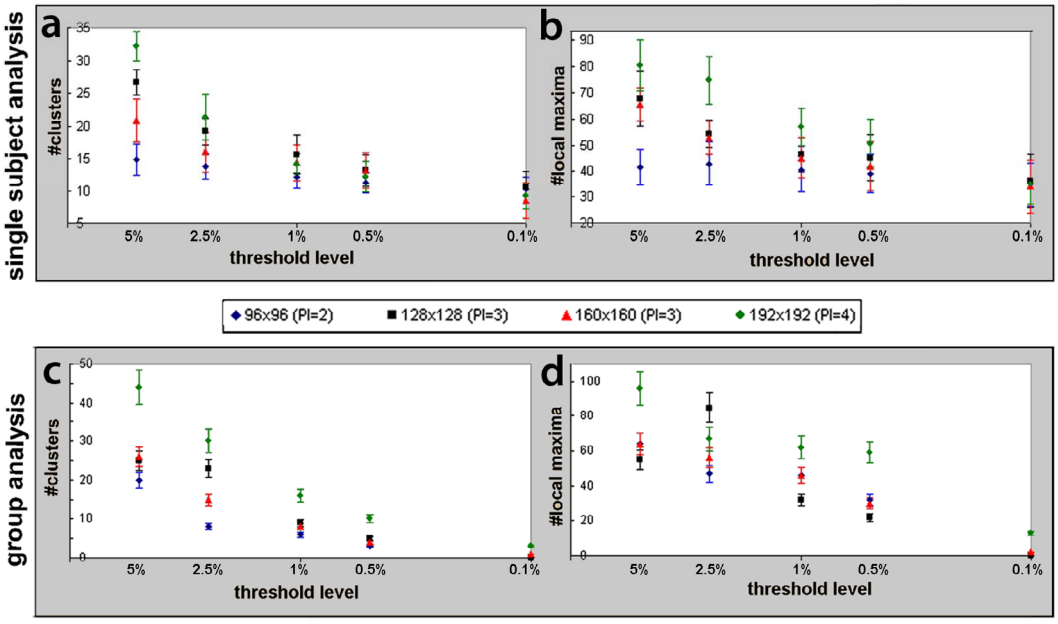

Figure 3.20 – BOLD Activation Separability using Different EPI Protocols.
*Average number of activated clusters (**a**)/(**c**) and local maxima (**b**)/(**d**) in dependence of the threshold level measured on the single subject level / group level (N = 6). The BOLD activation was detected in the*

*SMC. The errorbars in (**a**) and (**b**) denote the standard error across different subjects. The errorbars in (**c**) and (**d**) denote a standard error of 10 %.*

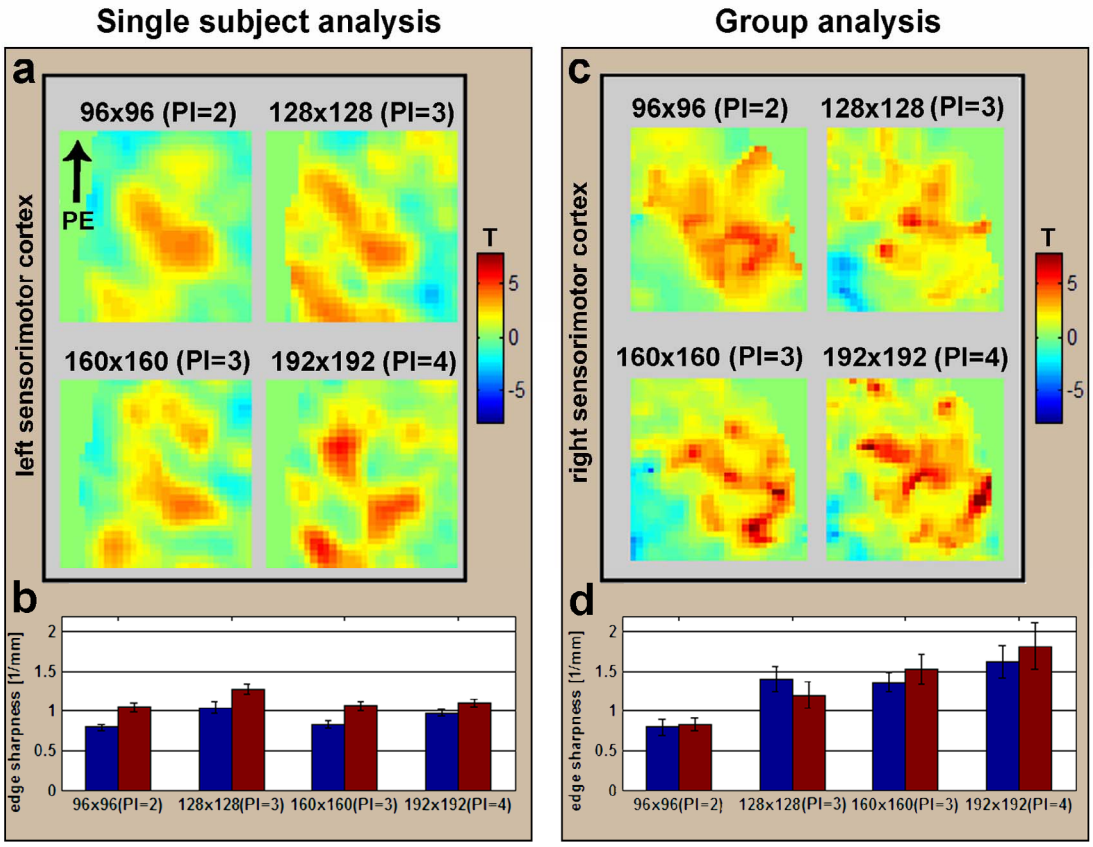

Figure 3.21 – Cluster-Edge Sharpness in the SMC using Different EPI Protocols.
*Average edge-sharpness of activated clusters in PE (blue) and RO direction (red) depicted for the single subject level (**a**) and for the group level (**b**). The edge-sharpness in PE (RO) direction was measured in 88 (174) activation profiles on the single subject level and in 20 (17) activation profiles on the group level.*

3.2.4 fMRI Experiment II: Motivation-Task Study

Data Acquisition and Processing

19 subjects were initially recruited and measured using the motivation-task described in Section 2.4.1.3. Data from 4 participants had to be discarded because of heavy head movement or incompliance with the task instruction. The final sample consisted of 15

healthy right-handed subjects (age = 26 ± 6 years, 3 females). Participants were measured using a standard and a high-resolution EPI protocol in randomized order. The motivation task comprised 48 trials with a pseudorandom order of presentation and a total duration of 16 min and 3 s. In addition to the fMRI protocols high-resolution T1-weighted 3D image data was acquired to detect potential morphological abnormalities in individuals. The standard and the high-resolution EPI datasets were acquired at matrix sizes of 96 x 96 (R = 2) and 160 x 160 (R = 3), respectively. Further imaging parameters were: *TR*/*TE* = 3000/27, repetitions = 321, *FOV* = 192 x 192 mm^2, # slices = 40, slice thickness Δz = 2 mm, interslice-gap = 1 mm, bandwidth = 1085 Hz/Px. The images were post-processed and statistically analyzed according to the methods described in Section 2.4.2 and Section 2.4.3. The images were normalized and resampled to a voxel size of 1.0 x 1.0 x 2.0 mm^3 and spatially smoothed with a Gaussian kernel size at *FWHM* of 3.2 x 3.2 x 8 mm^3. The condition of interest was "money win" versus implicit baseline.

3.2.4.1 Single Subject Analysis

The in-plane resolution was continuously improved when the matrix size (PI-factor) was increased from 96 x 96 (R = 2) to 160 x 160 (R = 3) using the 32-channel head coil (Figure 3.22). Bilateral NAcc activation was detected using both the 96 x 96 (R = 2) and the 160 x 160 (R = 3) EPI protocol (Figure 3.23). The transversal slices show that the BOLD activation was less blurred and more distinguishable in the 160 x 160 (R = 3) compared to the 96 x 96 (R = 2) dataset. Only one cluster in each hemisphere was detectable in the coronal slices of the standard 96 x 96 (R = 2) datasets whereas two clusters with separable local maxima in each hemisphere were detectable in the 160 x 160 (R = 3) datasets.

The T^{max}-values and the numbers of voxels were on average decreased by 14 % and by 70 %, respectively, using the 160 x 160 (R = 3) compared to the 96 x 96 (R = 2) EPI protocol (Figure 3.24 (a), (b)). It can be seen that the inter-subject variability of the T^{max}-values and the numbers of activated voxels was clearly reduced at increased matrix size (PI-factor). This led to a decrease of the relative error (i.e. mean/std. error) of the average T^{max}-value (number of activated voxels) from 7 % to 6 % (41 % to 36 %).

3.2.4.2 Group Analysis

In the high-resolution 160 x 160 (R = 3) datasets, the T^{max}-value was increased by 10 % while the number of activated voxels was decreased by 16 % compared to the standard 96 x 96 (R = 2) datasets (Figure 3.24 (c), (d)). In the NAcc, the BOLD specificity in the high-resolution datasets was clearly improved indicated by the increased number of spatially separable clusters (+ 40 %) and local maxima (+ 20 %) (Figure 3.24 (e), (f)).

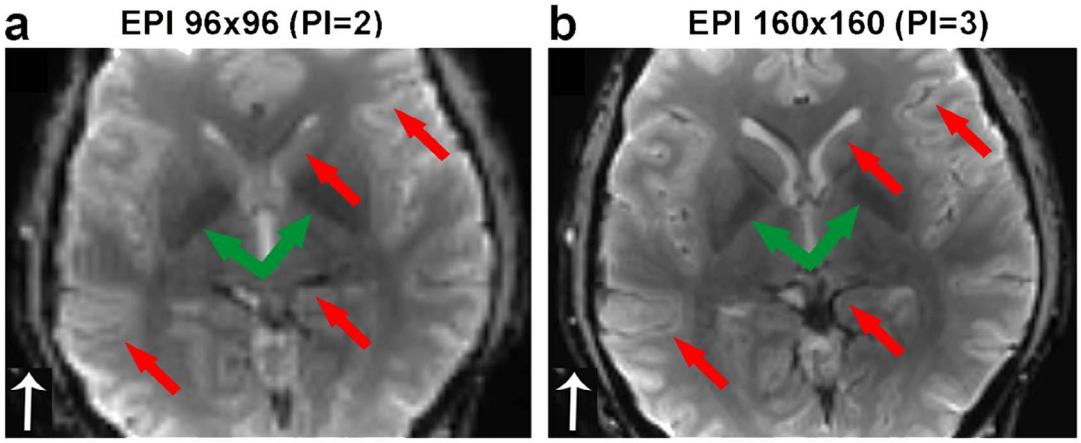

Figure 3.22 – EPI Slices Acquired with Optimized Matrix Size (PI-Factor) and Coil Setup.
*EPI time series averages (N = 321) from representative subjects acquired during the motivation-task experiment using a 32-channel head coil and the 96 x 96 (R = 2) (**a**) and the 160 x 160 (R = 3) EPI protocol (**b**). The EPI phase encoding direction is marked by the white arrows. Conspicuous structural differences between (**a**) and (**b**) are marked by the red arrows. The NAcc, which was the target brain region of the motivation task, is marked by the green arrows. For a fair comparison, the images were resampled to a 320 x 320 matrix size using bilinear interpolation.*

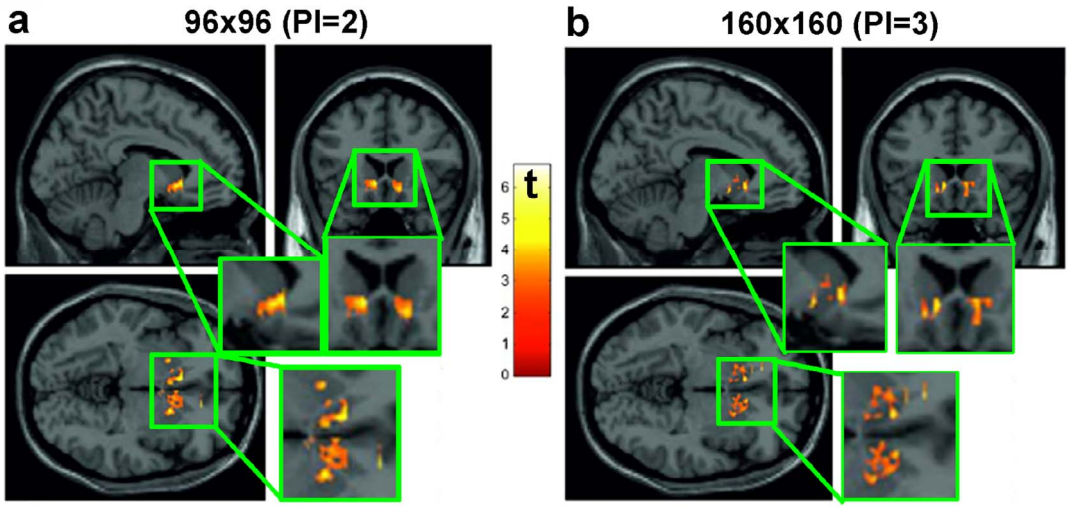

Figure 3.23 – Group Activation in the NAcc using EPI with Optimized Spatial Resolution.
BOLD activation outside the NAcc is not shown using a binary mask from the Nielsen & Hansen database (2002). The activation maps are depicted in MNI-space and were superimposed on a T1-weighted structural image.

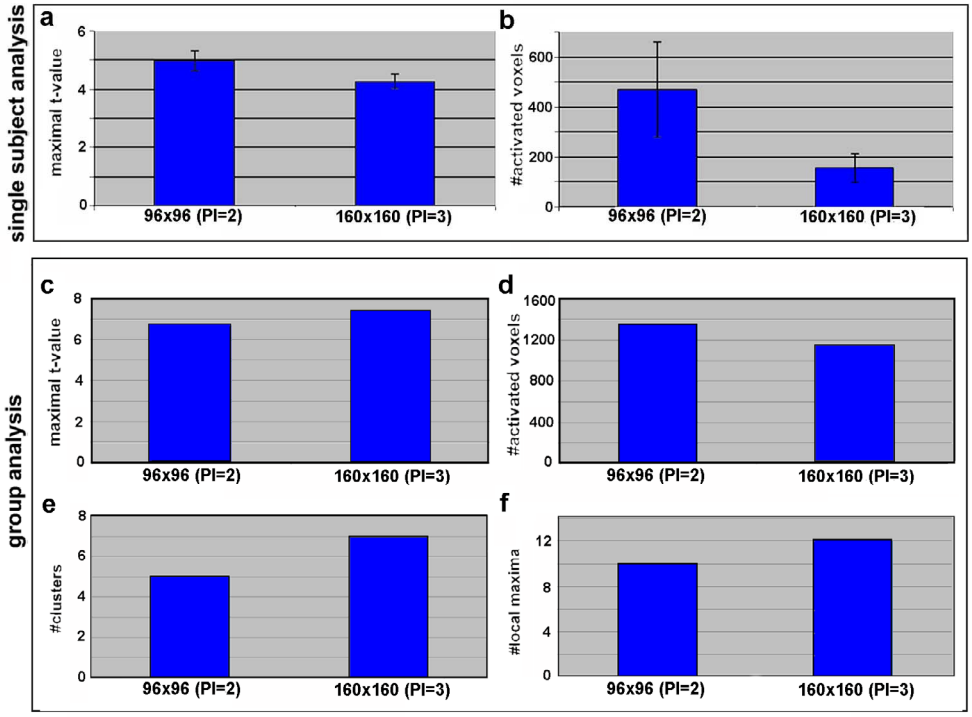

Figure 3.24 – FMRI Analysis Results of the Motivation-Task Study.
*Average maximal t-value (**a**) and average number of activated voxels (**b**) detected on the single subject level. Maximal t-value (**c**), number of activated voxels (**d**), clusters (**e**), and local maxima (**f**) detected on the group level. The results refer to BOLD activation in the NAcc, analysed at a statistical threshold of $p < 1$ % (uncorrected) and a minimal cluster size of $k \geq 20$ voxels.*

3.3 Acceleration of High-Resolution Segmented EPI using UNFOLD

The goal was to develop fMRI techniques with high spatiotemporal resolution. Exploiting the typical temporal sparsity of fMRI signals, the UNFOLD method effectively increases image acquisition time in fMRI (Madore, et al. 1999). In a first step, a 2D-Multislice Segmented EPI was implemented and tested in a phantom. Subsequently, a 3D version of a Segmented UNFOLD-EPI sequence was developed to increase the *SNR* compared to the 2D sequence (see Section 3.3.2). Furthermore, a phase-detrending algorithm was developed to reduce temporal autocorrelations hampering the statistical analysis of fMRI signals (see Section 2.4.3.2). Finally, the feasibility of fMRI at submillimeter voxel size and high temporal resolution was studied.

3.3.1 2D-Multislice Segmented UNFOLD-EPI

Sequence Implementation

The sequence diagram and the *k*-space acquisition pattern of the 2D-Multislice Segmented UNFOLD-EPI are schematically depicted in Figure 3.25. The total number of gradient-echoes acquired after a single RF-excitation was limited to $n^{phase} = 16$ to avoid spatial blurring artifacts due to T_2*-decay (see Section 3.2.1). An UNFOLD acceleration factor R was achieved by sampling every R^{th} phase encoding line of the *k*-space matrix. Hence, to acquire a matrix size of $N_y \cdot N_x$ voxels (i.e. N_y phase encodes), each slice was excited $N_y/R/n^{phase}$ times. For example, to acquire a 256 x 256 matrix size with an UNFOLD factor of R = 4, a single time frame required 4 RF-excitations per slice. To ensure a steady-state signal, the slices were excited uniformly in time. Hence, the slice-selecting gradient (G_z) was varied with each RF-excitation to excite the next slice while the amplitudes of the phase encoding gradients (G_y) were fixed. As soon as a set of phase encoding lines has been acquired for each slice, the first slice was excited again with altered phase encoding gradients to start the acquisition of a different set of phase encoding lines. This scheme was repeated until every R^{th} phase encoding line was acquired. For a total number of slices N^{sli}, and a repetition time of *TR* ms (i.e. the time between two RF-pulses), each slice was excited every $N^{sli} \cdot TR$ ms. Accordingly, a single time frame of the N^{sli} slices consisted of N^{sli} undersampled 2D data matrices of $N_y \cdot N_x$ voxels and was acquired with a nominal temporal resolution of $TR^{nom} = TR \cdot N^{sli} \cdot N_y/(R \cdot n^{phase})$.

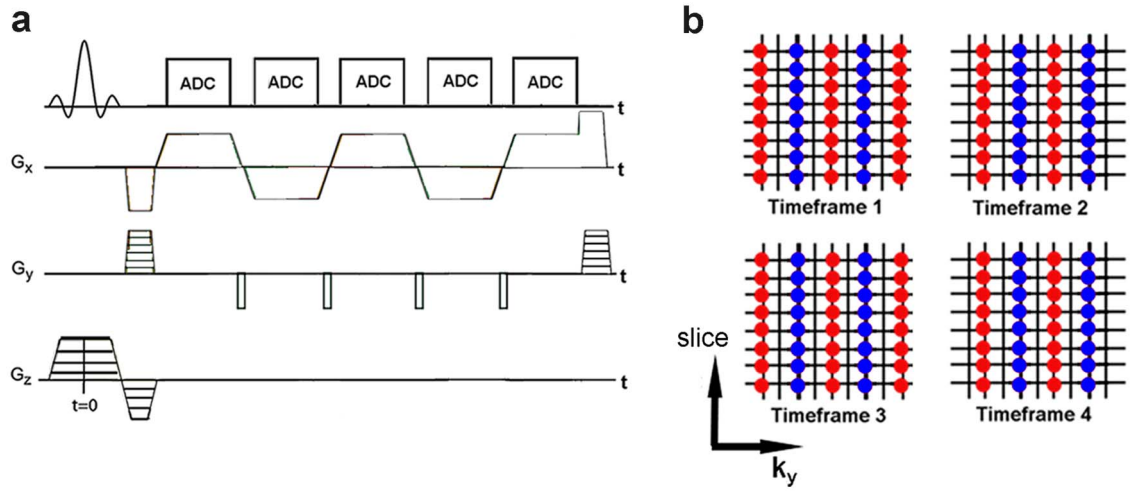

Figure 3.25 – Sequence Scheme of the 2D-Multislice Segmented UNFOLD-EPI.
*(**a**) Schematic sequence diagram (**b**) K-space acquisition scheme using UNFOLD factor R = 2 by skipping every other phase encoding line (i.e. $\Delta k_y = 4\pi/FOV$). In this example, each slice must be excited twice to collect sufficient data. To ensure a steady state signal, a different slice is being excited with each RF-excitation. The color scheme indicates the order in which the data is being acquired: The red data points are sampled after the first and the blue data points after the second RF-excitation of each slice.*

Phantom Measurements

Figure 3.26 depicts a representative slice of a resolution-phantom acquired using the 2D-Multislice Segmented UNFOLD-EPI sequence with an UNFOLD factor of R = 4. Multiple slices (i.e. N = 16) were acquired. The time series consisted of 32 images in total. Severe aliasing artifacts are visible in the image domain before temporal filtering (Figure 3.26 (a)). The power spectrum exhibits four uniformly spaced aliasing peaks (Figure 3.26 (b)). After the aliasing peaks are set to zero using a simple multiband filter (Figure 3.26 (c)), the image quality was significantly improved (Figure 3.26 (d)). Due to the severe aliasing before temporal filtering, the different bores of the resolution-phantom cannot be spatially resolved (Figure 3.26 (e)). In contrast, the same signal profile of the final image exhibits all 11 separate bores of the resolution-phantom with diameters between 0.5 mm and 13 mm (Figure 3.26 (f)).

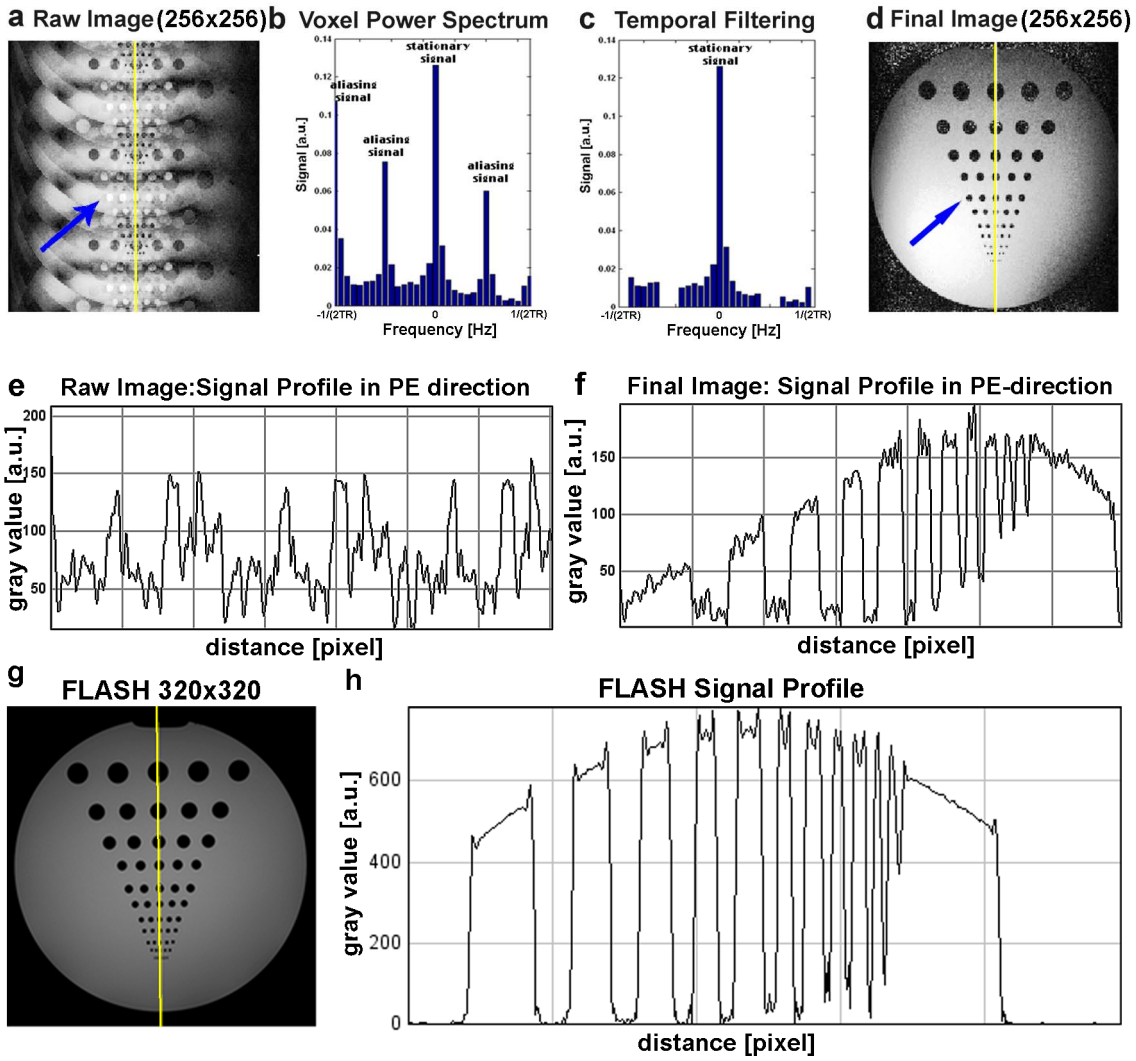

Figure 3.26 – Resolution-Phantom Acquired with the Segmented 2D UNFOLD-EPI.
*A time series of 32 scans (256 x 256 voxels) consisting of 16 slices was acquired with an UNFOLD factor of R = 4. A representative slice of the resolution phantom is shown before (**a**) and after the removal of spatial aliasing artifacts (**d**). The power spectrum of a single voxel at the location indicated by the blue arrow is depicted before (**b**) and after temporal filtering (**e**). Signal profiles shown along the yellow lines in (**a, d, g**) along the PE direction of the raw image (**e**) and of the final image (**f**), respectively. For comparison: High-resolution FLASH image (320 x 320 pixels) (**g**) and corresponding signal profile (**h**).*

3.3.2 3D Segmented UNFOLD-EPI

Sequence Implementation

The sequence diagram and the *k*-space acquisition pattern of the 3D Segmented UNFOLD-EPI are schematically depicted in Figure 3.27. As in the 2D case, the total number of gradient-echoes acquired after a single RF-excitation was limited to $n^{phase} = 16$ to avoid blurring artifacts due to T_2*-decay. An UNFOLD factor R, with $R = p^2$ ($p \in \mathbb{N}$) was achieved by either undersampling along the phase encoding dimension (k_y) only or by undersampling along both, the phase encoding and the partition dimension (k_z) (Figure 3.27 (b)). In the both scenarios, the partition ("slice selecting") gradient G_z was switched with every RF-pulse, similar to the 2D case. However, in a 3D sequence, there is no steady-state constraint because the whole imaging volume is being excited with each RF-pulse. The purpose of switching the partition gradient rapidly was to sample the *k*-space center with higher update rate. With regard to the UNFOLD method, this issue has not been addressed in the literature yet. However, it was suspected that sampling the *k*-space center with a higher update rate improves the detection of transient signals in fMRI. If the number of partitions and phase encoding lines in 3D equals to the number of slices and phase encoding lines in 2D, the sequence timing is identical.

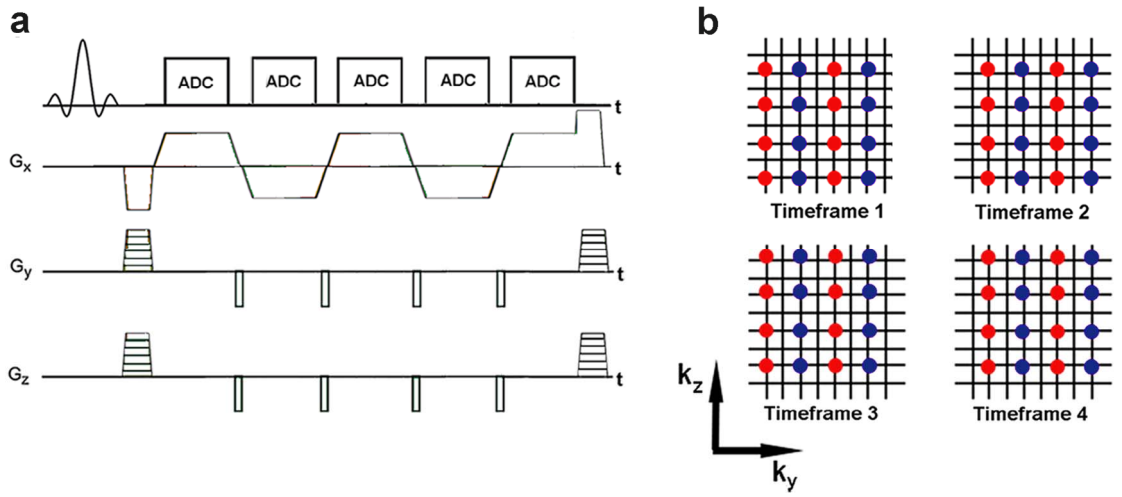

Figure 3.27 – Sequence Scheme of the 3D Segmented UNFOLD-EPI.
*(**a**) Sequence diagram (**b**) K-space acquisition scheme with UNFOLD factor R = 4 by sipping every other phase encoding line in k_y and k_z direction (i.e. $\Delta k_y = 4\pi/FOV_y$; $\Delta k_z = 4\pi/FOV_z$). The colour scheme indicates the order in which the data is being acquired. The red data points are sampled first and subsequently the blue data points in order to sample the k-space center with higher update rate.*

3.3.2.1 Image Quality and Signal-to-Noise: 2D-Multislice vs. 3D Segmented UNFOLD-EPI

Figure 3.28 shows resolution-phantom measurements using a fourfold accelerated 2D Segmented UNFOLD-EPI sequence and two types of fourfold accelerated 3D Segmented UNFOLD-EPI sequences. The 3D sequence can be accelerated with UNFOLD in one and in two dimensions. The 3D Segmented UNFOLD-EPI (type 1) was accelerated by skipping three phase encoding lines in k_y-direction whereas the 3D Segmented UNFOLD-EPI (type 2) achieved the same acceleration factor by skipping one phase encoding lines in k_y and one phase encoding lines in k_z-direction (i.e. partition direction). The comparison between the fully sampled (i.e. four consecutive timeframes summed up) 2D-Multislice and 3D Segmented EPI images reveals comparable image quality (Figure 3.28 (a), (c)). Accordingly, the signal profiles in PE-direction of both sequences are similar in terms of overshoots at the boundaries of the resolution-phantom bores which are more prominent for small diameters and small spatial distance between the bores. Figure 3.28 (b), (d), and (e) show that independent of the employed sequence, the unaliased UNFOLD images reveal high image quality free of visible aliasing indicating that the aliasing peaks in the temporal frequency spectrum were properly re-

moved. In consistence, the line profiles (in PE direction) reveal no obvious differences between the 2D and the 3D (type 1, type 2) UNFOLD images. It should be noted that the image quality in terms of ringing artifacts was not affected by UNFOLD which can be seen by comparable overshoots at the boundaries of the bores in the fully sampled 2D and 3D images (a, c) and the UNFOLD images (b, d, e). Moreover, the line profiles suggest that structures down to a diameter of approximately 2 mm (i.e. bore # 7 from left to right) can be resolved.

The *SNR* was increased by a factor of 2.4 in the fully sampled reference images (i.e. no UNFOLD) by using the 3D (type 2) compared to the 2D sequence (Figure 3.29). Comparing the accelerated UNFOLD 2D and 3D (type 1 and type 2) images, the *SNR* was increased by a factor of 2.2 and 2.3, respectively, which is close to the predicted value of 2.7. Comparing the *SNR* in the fully sampled images and the UNFOLD images of the same datasets, the *SNR* in the 2D, 3D (type 1), and 3D (type 2) datasets was reduced by 19 %, 27 %, and 25 %, respectively.

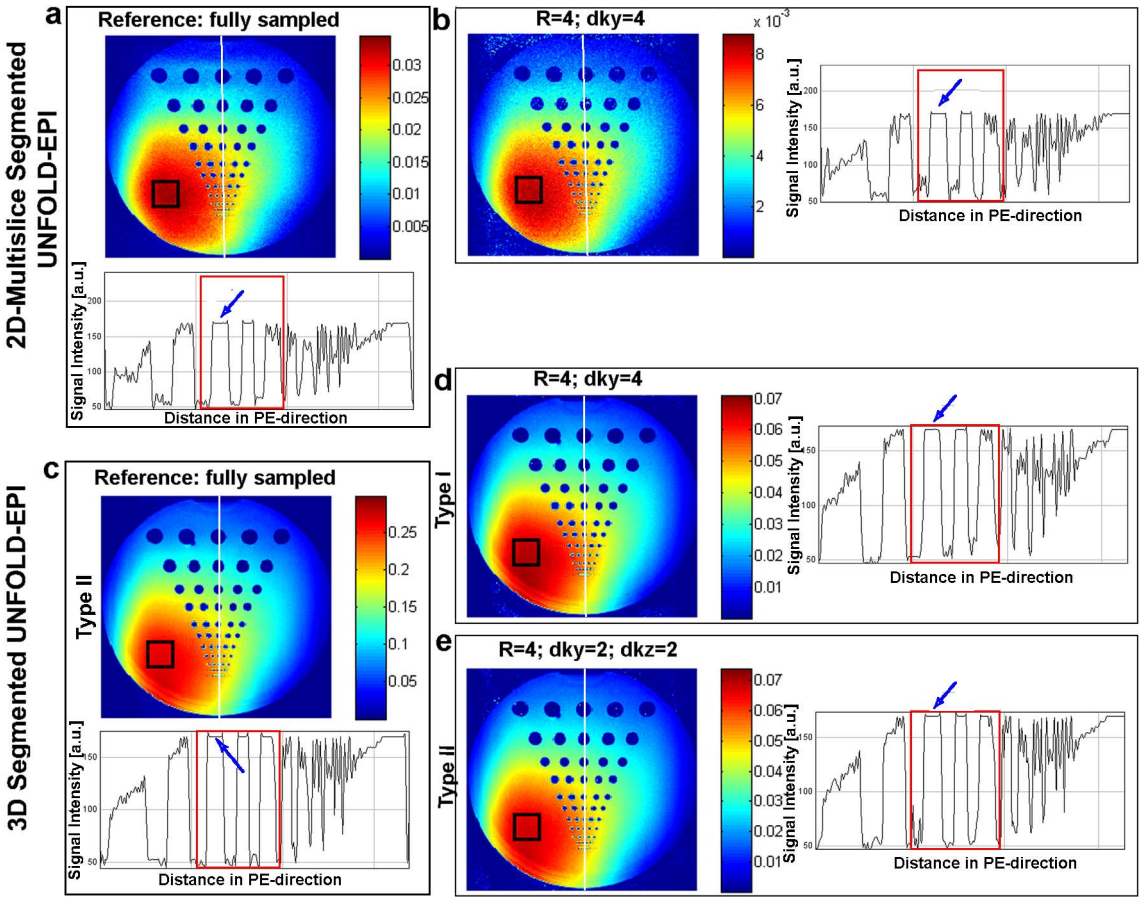

Figure 3.28 – Resolution-Phantom Measurements: 2D vs. 3D Segmented UNFOLD-EPI.
*A time series (N = 32) of phantom images (192 x 192 pixel, 60 slices) was acquired with a fourfold accelerated segmented 2D-Multislice (**a**, **b**) and a 3D UNFOLD-EPI (**c**, **d**, **e**). In (**b**), the step size in PE direction was 4·Δk_y (i.e. $\Delta k_y = 2\pi/FOV_y$). In (**d**, **e**), the step size in PE and partition direction was 2·Δk_y and 2·Δk_z (i.e. $\Delta k_z = 2\pi/FOV_z$), respectively. The fully-sampled reference images are shown for the 2D sequence and the 3D sequences in (**a**) and (**c**), respectively. The 2D and 3D reference images were obtained by recombining k-space data from four undersampled images. Signal profiles next to the phantom images are depicted along the white vertical lines, parallel to the PE direction, superimposed onto the phantom images. The black square indicates the region in which the temporal SNR was measured. The colorbar encodes signal intensities. The images shown here were reconstructed from the data of a single channel as it can be seen by the intensity profile.*

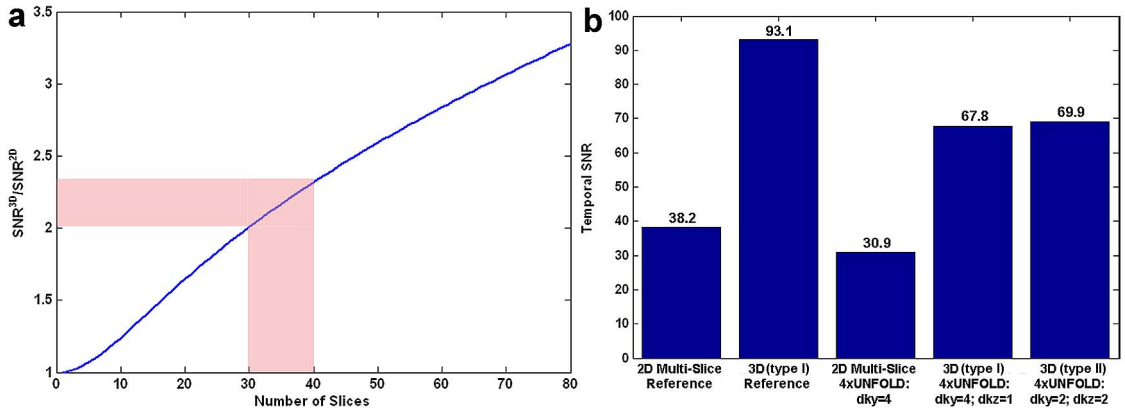

Figure 3.29 – SNR Comparison: 2D-Multislice vs. 3D Segmented UNFOLD-EPI.
*(**a**) SNR simulation based on Eq. 1.69 assuming a sequence time of T_{seq} = 491 ms (i.e. time required for RF-excitation and the signal read out) and a longitudinal relaxation time of T_1 = 1820 ms. The typical slice number for whole-brain coverage in fMRI is indicated by the red area. (**b**) Temporal SNR comparison in a resolution-phantom using the 2D-Multislice and the 3D Segmented UNFOLD-EPI. The SNR was measured in the black ROI in Figure 3.28.*

3.3.3 Reduction of Temporal Coherence

UNFOLD datasets exhibit shifted and broadened aliasing peaks resulting from linear and quadratic phase drifts due to signal instability and scanner imperfections (Hu 2011). Accordingly, the removal of spatial aliasing requires broad temporal filtering introducing correlations between the images decreasing the effective temporal resolution. Hu and colleagues (2011) successfully demonstrated that after removal of first and second order phase trends, minimal filtering is sufficient to eliminate spatial aliasing. Furthermore, it was shown that the signal detection in fMRI is improved due to increased temporal signal stability.

3.3.3.1 Phase-Detrending Algorithm

According to Eq. 2.17, the phase of a voxel signal acquired with UNFOLD contains phase jumps across the time in addition to the natural phase drifts. The phase jumps have to be eliminated before the linear and quadratic phase drift can be estimated. A possible solution implemented in this work is to reconstruct a time series of fully sampled timeframes without aliasing and therefore without the phase jumps by combining R undersampled timeframes acquired with an UNFOLD factor R. The phase in each voxel

of the undersampled time series acquired with high frame rate was approximated by linear interpolation. The interpolated phase evolution of a representative voxel acquired during a fingertapping experiment using an eightfold accelerated 3D Segmented UNFOLD-EPI (type 2) is shown in Figure 3.30 (a). The linear and the quadratic component of the phase drift was estimated by a second order polynomial fit,

$$\Phi^{meas}\left(t_i\right) = \Phi_0 + b \cdot t_i + c \cdot t_i^2 , \qquad \textbf{3.1}$$

where t_i is the sample number of the R undersampled timeframes ($t_i = t_1 ... t_R$). Subsequently, the linear $\Phi^{lin}\left(t_i\right) = b \cdot t_i$ and quadratic phase drift $\Phi^{quad}\left(t_i\right) = c \cdot t_i^2$ were subtracted from the measured phase to obtain the corrected phase:

$$\Phi^{corr}\left(t_i\right) = \Phi^{meas}\left(t_i\right) - \Phi^{lin}\left(t_i\right) - \Phi^{quad}\left(t_i\right) \qquad \textbf{3.2}$$

Figure 3.30 (b) depicts the power spectrum of the voxel shown in (**a**) before and after phase detrending. As it can be seen, the width of the aliasing peaks has been significantly narrowed and the major part of the energy of the aliasing peaks is contained in a single frequency bin. This indicates that "less" temporal filtering may be required to remove spatial aliasing in the images which was tested in the following paragraph.

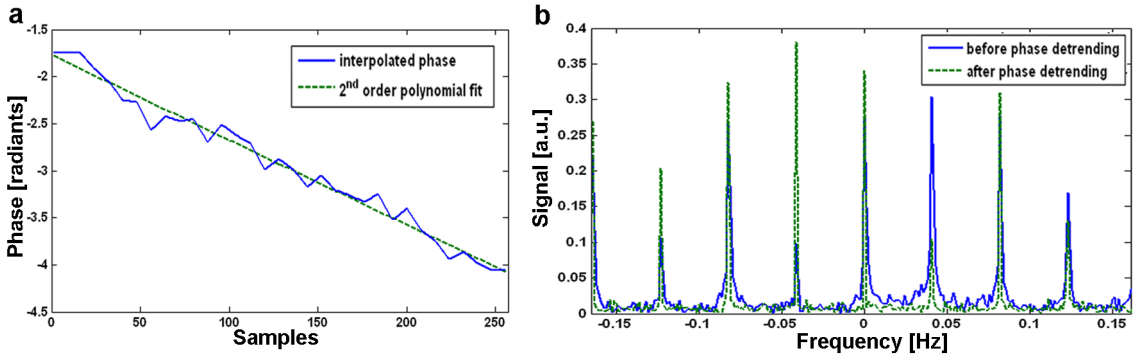

Figure 3.30 – Power Spectrum of a Single Voxel Before and After Phase Detrending.
*(**a**) Interpolated phase evolution (blue solid line) for a typical voxel of an UNFOLD dataset (N = 256 images) acquired with an 8-fold accelerated 3D Segmented UNFOLD-EPI (type II: $\Delta k_z = 2$, $\Delta k_y = 4$) during a fingertapping experiment. The second order polynomial fit (Eq. 3.1) is shown as green dashed line. (**b**) Power spectrum of the voxel shown in (**a**) exhibiting 8 aliasing peaks resulting from R = 8.*

3.3.3.2 Effects on Spatial Aliasing and Temporal Coherence

In Figure 3.31, the difference between the images obtained without and with phase-detrending clearly demonstrates the effectiveness of phase detrending prior to temporal filtering. As expected from the smaller peak width in the power spectrum, it can be seen that spatial aliasing was significantly reduced in the phase-detrended datasets. The deciding issue to remove spatial aliasing in the image domain is that the signal energy of the aliasing peaks is being fully removed. In the following, multiband filtering n-bin refers to setting n frequency bins, symmetrically around the main aliasing peaks to zero.

Without phase detrending, the image quality was superior using the multiband filter 3-bin compared to the 1-bin strategy (Figure 3.31 (b), (c)). However, severe aliasing was still present using the multiband filter 3-bin strategy without prior phase detrending. In contrast, no visible aliasing is apparent in the phase-detrended datasets either using the multiband filter 3-bin or 1-bin strategy (Figure 3.31 (d), (e)).

The impulse response function or temporal *PSF* of the multiband filter 1-bin and the multiband filter 3-bin is depicted in Figure 3.32. It shows that the width of the main lobe, a measure of the effective temporal resolution, was independent of the filtering strategy. However, due to less temporal filtering using the multiband filter 1-bin compared to the 3-bin strategy, the temporal coherence between the images of the time series, which can be measured by the amplitude of the first side lobe of the filter response function, was reduced by 66 %.

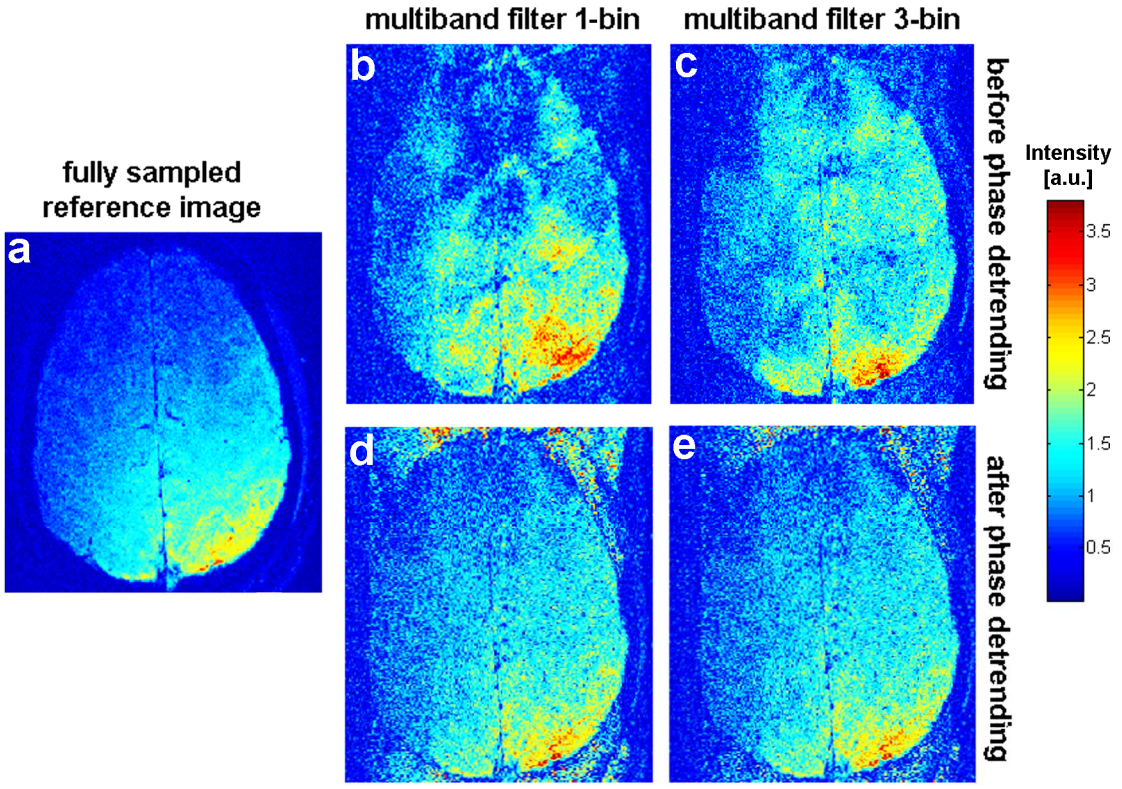

Figure 3.31 – Image Quality Before and After Phase-Detrending.
*The in-vivo data was acquired using an accelerated segmented 3D UNFOLD-EPI with acceleration factor R = 8. (**a**) Fully sampled reference slice acquired by combining 8 undersampled UNFOLD timeframes. (**b**-**c**) UNFOLD slices without prior phase detrending using the multiband filter 1-bin and 3-bin strategy, respectively. (**d**-**e**) UNFOLD slices with prior phase detrending using the multiband filter 1-bin and 3-bin strategy, respectively. The images shown were reconstructed from the data of a single channel which is apparent from the signal intensity profile.*

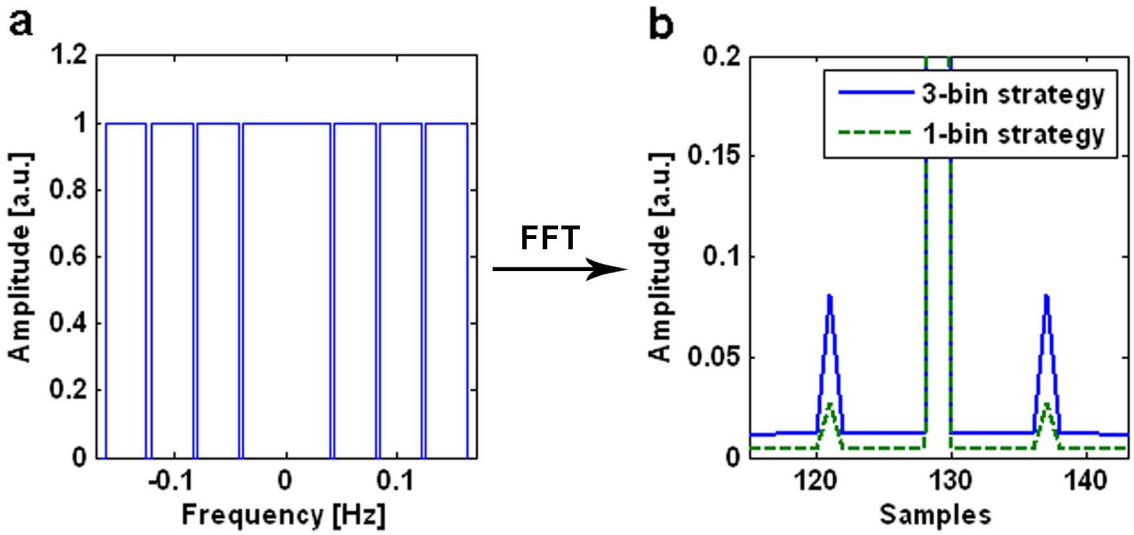

Figure 3.32 – Temporal Coherence using Different Multiband Filter Strategies.
*(**a**) Normalized signal amplitude of the multiband filter 3-bin. (**b**) Normalized amplitude of the temporal PSF of the multiband filter 1-bin and respectively 3-bin strategy.*

3.3.4 Feasibility Study

A major challenge for high-resolution fMRI is the limited temporal resolution. However, sufficient temporal sampling is essential to detect transient BOLD signal modulations in event-related fMRI experiments. The 3D Segmented UNFOLD-EPI was accelerated by a factor of R = 8 to obtain high-resolution 3D images at 0.7 x 0.7 mm^2 in-plane resolution covering half of the brain within a *TR* of 3 seconds. The sequence was tested in an event-related finger tapping experiment. The goal was to study feasibility with this technique for fMRI requiring both, high temporal and spatial resolution. A condensed version of this section can be found in the publication (Domsch, et al. 2011).

Data Acquisition and Processing

Three healthy subjects participated in this event-related fingertapping study. They received an auditory stimulus presented at a rate of 1/15 Hz. According to the Nyquist criterion, the frame rate without UNFOLD acceleration was insufficient to detect neuronal activation in this fMRI experiment because the sampling rate was significantly smaller than the stimulus rate (Figure 3.33). At each stimulus, fingertapping was performed for three seconds. In a total scan time of 13 min, 256 undersampled timeframes

were acquired using the accelerated 3D Segmented UNFOLD-EPI (R = 8; $\Delta k_y = 4$; $\Delta k_z = 2$). Image post-processing included phase detrending, temporal filtering, and the standard procedures described in Section 2.4.2 and Section 2.4.3.

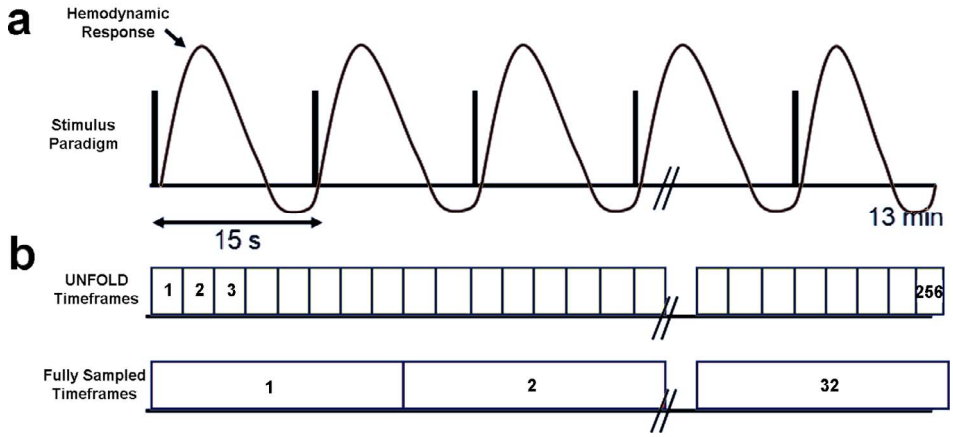

Figure 3.33 – Event-Related Stimulus Paradigm of the Fingertapping Experiment.
*(**a**) Timing of short repetitive stimuli at a rate of 1/15 Hz and the triggered hemodynamic response. (**b**) Data acquisition timing of UNFOLD and fully sampled timeframes. According to the Nyquist criterion, a minimal sampling frequency of $\omega^{Nyq} = 2/15$ Hz is required to directly detect the BOLD signal of the neuronal activation associated with the stimulus. Therefore, the sampling rate of $2.5 \cdot \omega^{Nyq}$ of the undersampled timeframes is sufficient whereas the sampling rate of $0.3 \cdot \omega^{Nyq}$ without UNFOLD would is too low.*

BOLD Activation in the SMC

A comparison between the mean image of the fully-sampled time series ($N = 32$) and the mean image of the undersampled time frames ($N = 256$) is depicted in Figure 3.34. It can be seen that no noticeable artifacts were introduced by the UNFOLD method. Robust neuronal activation associated with the fingertapping task was detected in all subjects whereas strong bilateral activation was detected only in subject 1 and subject 2 (Figure 3.35). Furthermore, no clear false positives were found at a threshold of $p < 0.005$. In each subject, the peak voxel (i.e. the voxel with the highest *t*-value) was located in the SMC (Table 3.4).

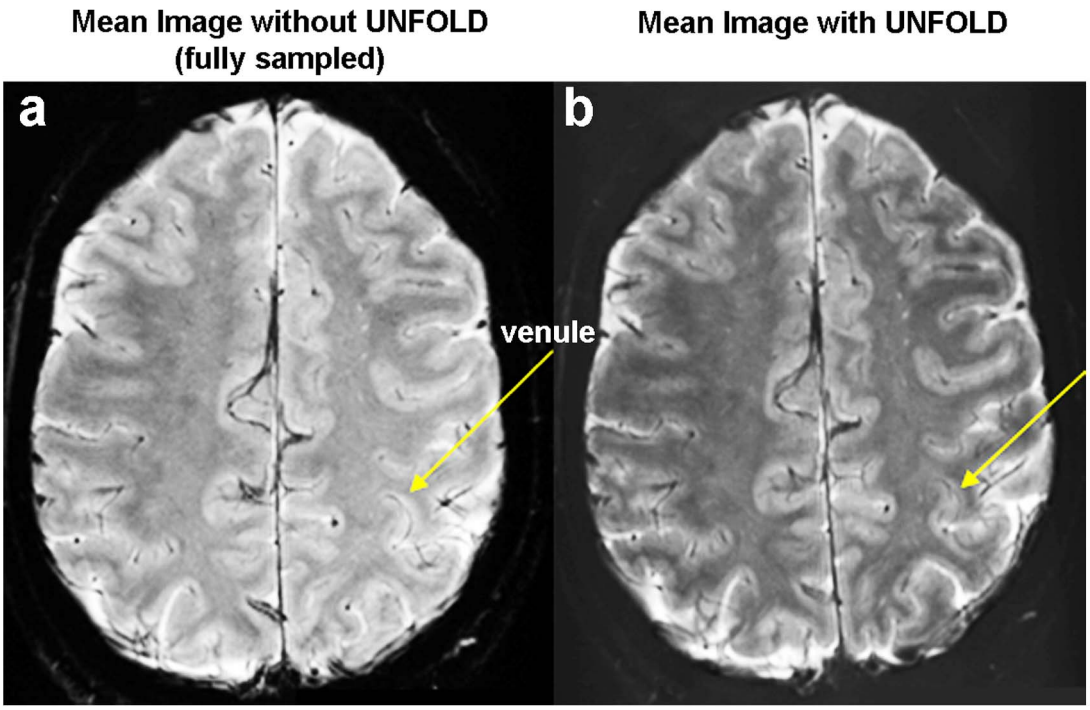

Figure 3.34 – Axial EPI Slice Acquired at 0.7 x 0.7 mm^2 Resolution using UNFOLD.
(**a**) *Representative slice averaged over 32 fully sampled timeframes acquired during the fingertapping experiment.* (**b**) *The same slice averaged over 256 UNFOLD timeframes. The yellow arrow marks a venule which can be clearly seen in the fully sampled and in the UNFOLD images. The images in* (**a**) *and* (**b**) *were reconstructed from the same dataset and were contrasted differently emphasizing on structural details. For imaging, the accelerated 3D Segmented UNFOLD-EPI (R = 8; Δk_y = 4; Δk_z = 2) was used with the following sequence parameters: TE/TR = 35ms/93.6 ms, TR/3D-stack = 3.05 s, FOV = 180 x 180 x 48mm^3, flip-angle = 22°, bandwidth = 520Hz/Px, 3D encoding direction: head to foot, phase encoding direction: anterior-posterior. A fat-saturation pulse of 5ms was applied before RF-excitation of a 3D slab. The matrix size was 256 x 256 x 16 leading to a nominal in-plane resolution of 0.7 x 0.7 mm^2 and a slice-thickness of 3.0 mm.*

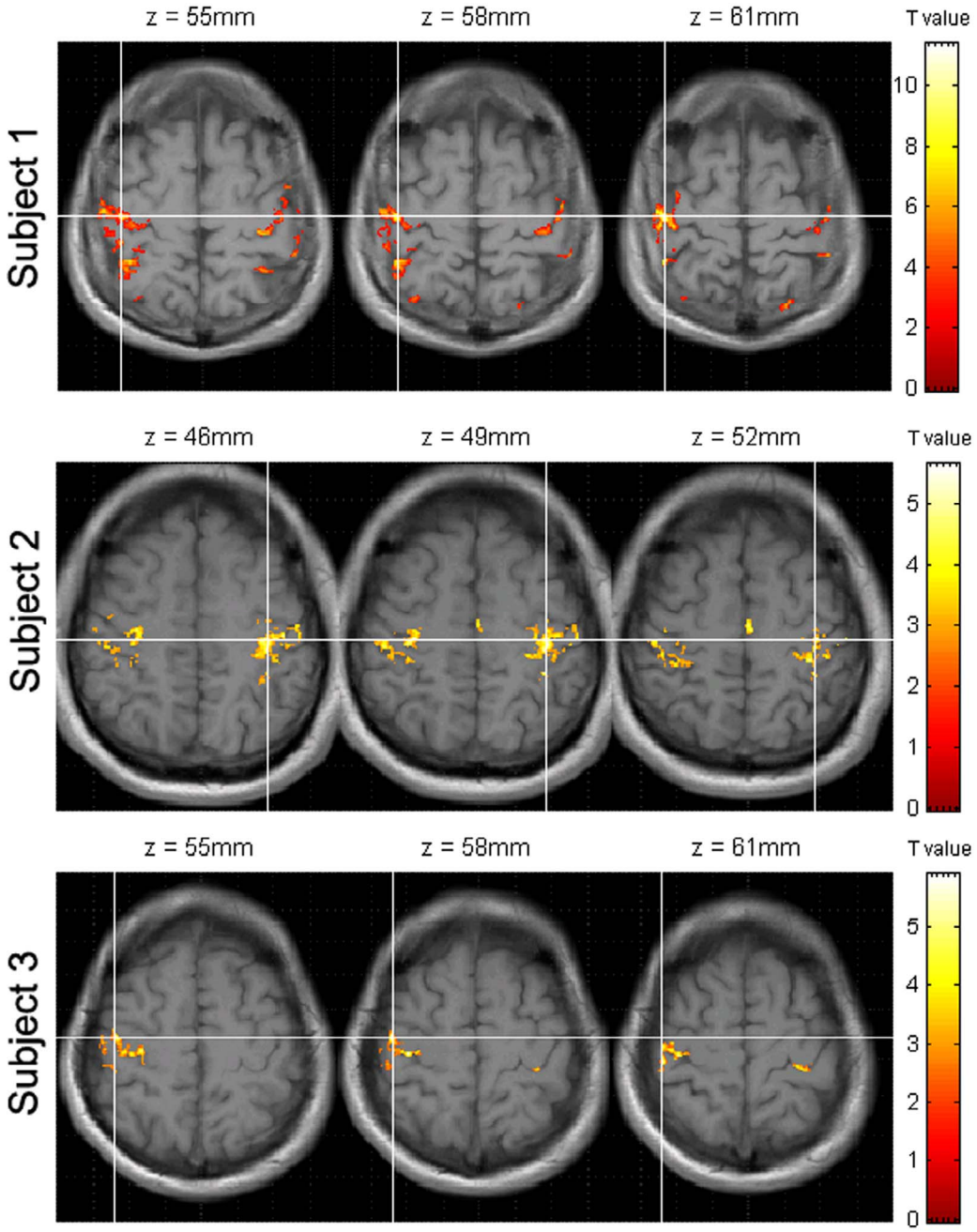

Figure 3.35 – BOLD Activation in the SMC at 0.7 x 0.7 mm^2 In-Plane Resolution.
The activation maps from three healthy subjects, presented in MNI space, were overlaid on individual T1-weighted images. The statistical threshold for activation was set to $p < 5 \cdot 10^{-3}$ and the minimal cluster size was set to $k \geq 50$ pixels. The z-coordinates are depicted for each slice and each subject. The left hemisphere is displayed on the right. The voxel with the maximal t-value in each slice is marked by the cross-hairs.

Subject	T^{max}	N^{active}	MNI: x y z	Area
1	11.33	4510	43 -18 61	SMC-right
2	7.77	5401	-37 -20 49	SMC-left
3	8.88	1794	38 -22 46	SMC-right

Table 3.4 – BOLD Activation in the SMC at 0.7 x 0.7 mm^2 In-Plane Resolution.
The maximal t-value, T^{max}, the total number of activated voxels, N^{active}, the MNI-coordinates of the peak voxel, and the corresponding brain area of the peak voxel are depicted for each subject at a statistical threshold of $p < 5 \cdot 10^{-3}$ and a cluster size of $k \geq 50$ pixels.

3.4 Increased Statistical Inference in UNFOLD fMRI with Novel Filter

In the previous section a phase detrending algorithm was developed with the main goal to decrease temporal coherence in UNFOLD fMRI datasets. By using a standard multiband filter (i.e. setting the aliasing peaks to zero), temporal coherence is still present in the fMRI signal compromising statistical inference. In this section, a novel UNFOLD filtering technique is proposed to reduce temporal coherence or rather non-white noise in fMRI datasets acquired with UNFOLD. The proposed filtering strategy was applied to simulated fMRI datasets without aliasing signals resulting from undersampling and without natural non-white noise sources in order to investigate the filtering effects on a general basis. Furthermore, the proposed filtering strategy was compared to multiband filtering in a simple fingertapping fMRI experiment at sub-millimeter spatial and high temporal resolution using the 3D Segmented UNFOLD-EPI sequence. The imaging parameters were the same as in the "Feasibility Study" in Section 3.3.4. The experimental setup is briefly summarized in the next paragraph. A condensed version of this section can be found in the publication (Domsch, et al. 2012).

3.4.1 Development of the White-Noise Filter

Figure 3.36 shows a typical power spectrum of a single voxel time course recorded with UNFOLD factor R during the fingertapping experiment described in Section 3.4.3. According to Eq. 2.18, the power spectrum exhibits R uniformly spaced peaks at the frequencies $f = TR^{-1}\left(n / \mathrm{R} - 1/2\right)$, with n = (0, 1, 2, ..., R - 1), where TR denotes the repetition time per imaging volume (i.e. TR = 3.05 s). The aliasing peak width varied between 1.3-9.3·10^{-3} Hz or respectively between 1-7 frequency bins. The average peak width was 4·10^{-3} Hz corresponding to 3 frequency bins. Improper removal of the aliasing peaks leads to spatial aliasing affecting the detectability of activation. Thus, four different multiband filters with different widths were tested to remove the aliasing peaks by setting n = 1, 3, 5, 7 frequency bins symmetrically around each aliasing peak to zero. These filter setups are referred to as multiband filter n-bin. Furthermore, an alternative filtering strategy was used replacing the aliasing peaks with Gaussian white noise, referred to as white-noise filter n-bin. The mean and the variance of the simulated Gaussian noise were estimated from the intensity distribution in the frequency spectrum, ex-

cluding the aliasing frequencies itself, the three frequency components next to the aliasing frequencies, the basic stimulation frequency and its first harmonic.

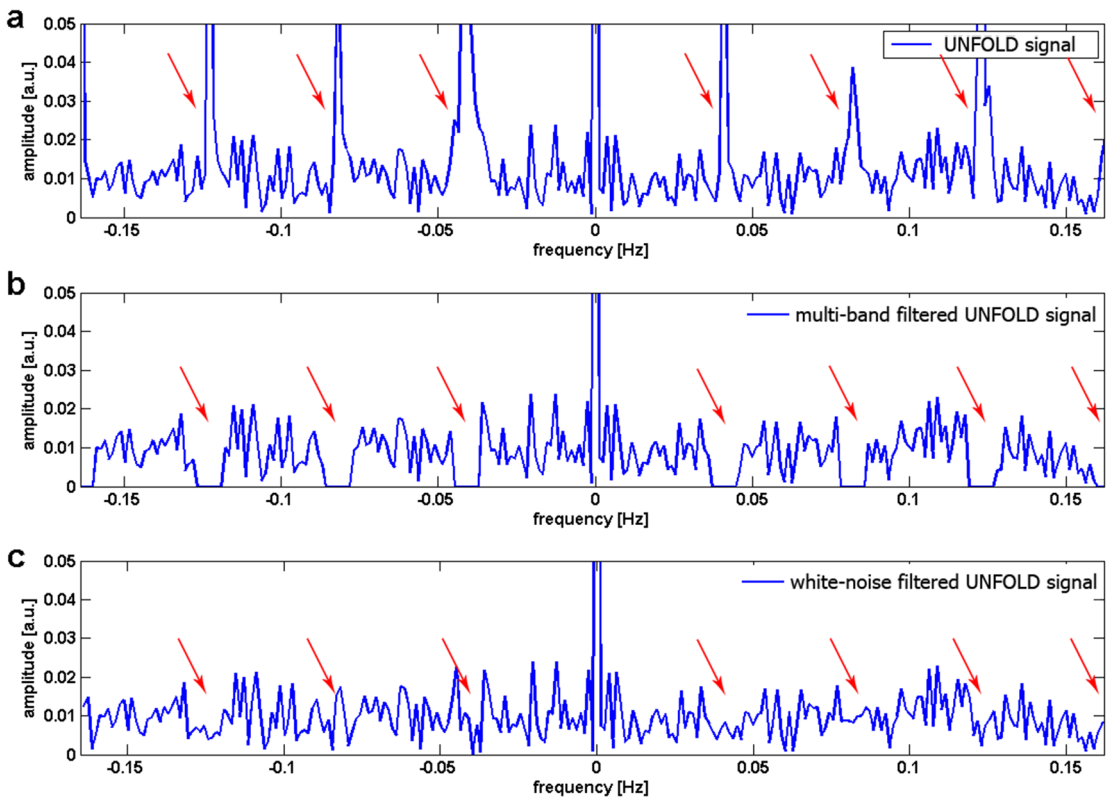

Figure 3.36 – Typical Power Spectrum of a Single Voxel using UNFOLD.
*(**a**) Unfiltered UNFOLD spectrum. Notice that the aliasing peaks, indicated by the red arrows, have high variability in the peak widths. (**b**) Filtered power spectrum using the multiband filter 7-bin strategy. (**c**) Filtered power spectrum using the white-noise filter 7-bin strategy.*

3.4.2 Simulation Study

Figure 3.37 shows two simulated time series consisting of 256 images containing Gaussian white noise in the time domain. In the first time series, artificial activation was added to the time signal of 7.7 % of all voxels (active dataset) while the second time series consisted of Gaussian white noise solely (null dataset). In the active dataset, the frequency bins 1, 8, 15… 249 of the power spectrum of the time signal have non-zero signal contribution due to the simulated activation. Thus, the remaining six frequency

bins between neighbouring activation peaks contained only noise. The noise was progressively "colored" by successively increasing the number of deleted noise bins until five of the six frequency bins between the neighbouring activation peaks were set to zero. In other words, the multiband filter n-bin was used with n = 1-5. Afterwards, the colored noise was re-whitened by adding artificial noise using the white-noise filter 1-5 bin strategy. After each of the different filters was applied, signal changes were modelled on a voxel-by-voxel basis according to the GLM (see Section 2.4.3.1). Before the GLM parameters were estimated, the AR(1) model was used to account for serial correlations (see Section 2.4.3.2).

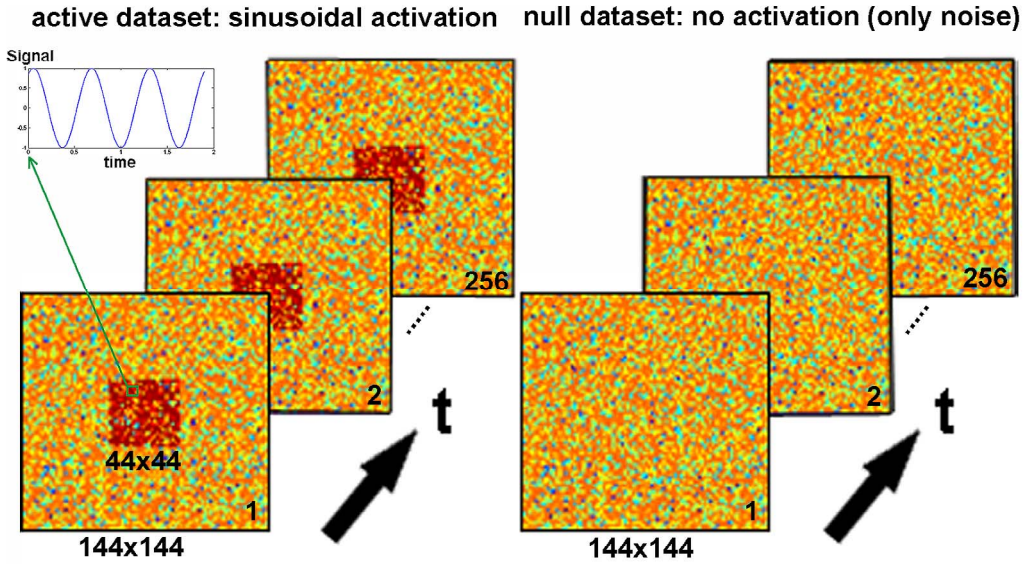

Figure 3.37 – Simulated fMRI Datasets Consisting of an Active and a Null Dataset.
In the active dataset (left), the central 44 x 44 voxels are activated whereas the null dataset (right) consists only of non-activated noisy voxels. The time course of an activated voxel is exemplarily shown for the green square. Each dataset consists of a time series of 256 slices with a dimension of 144 x 144 voxels. The colour coding scheme shows the signal intensity in each voxel. The temporal SNR (tSNR) was set to tSNR = 7.1, a typical value for fMRI datasets acquired at high spatiotemporal resolution.

Temporal Autocorrelations: Stability of the White-Noise Filter Approach

The autocorrelation function (ACF) of the average time-course of 20 voxels of the null dataset shows a characteristic side lobe peak after temporal filtering was performed (Figure 3.38 (a)). For multiband filtering, this peak successively increased with the number of removed bins (Figure 3.38 (b)). In contrast, the autocorrelation (i.e. the first

side lobe peak) was significantly smaller and remained stable when the white-noise filtering approach was chosen. The side lobe peak of the autocorrelation function for the white-noise filtering strategy in dependence of the number of frequency bins used to estimate the artificial noise can be depicted from Figure 3.38 (c). It can be seen that the autocorrelation rapidly stabilised and was not further reduced if more than approximately 10 frequency bins were used.

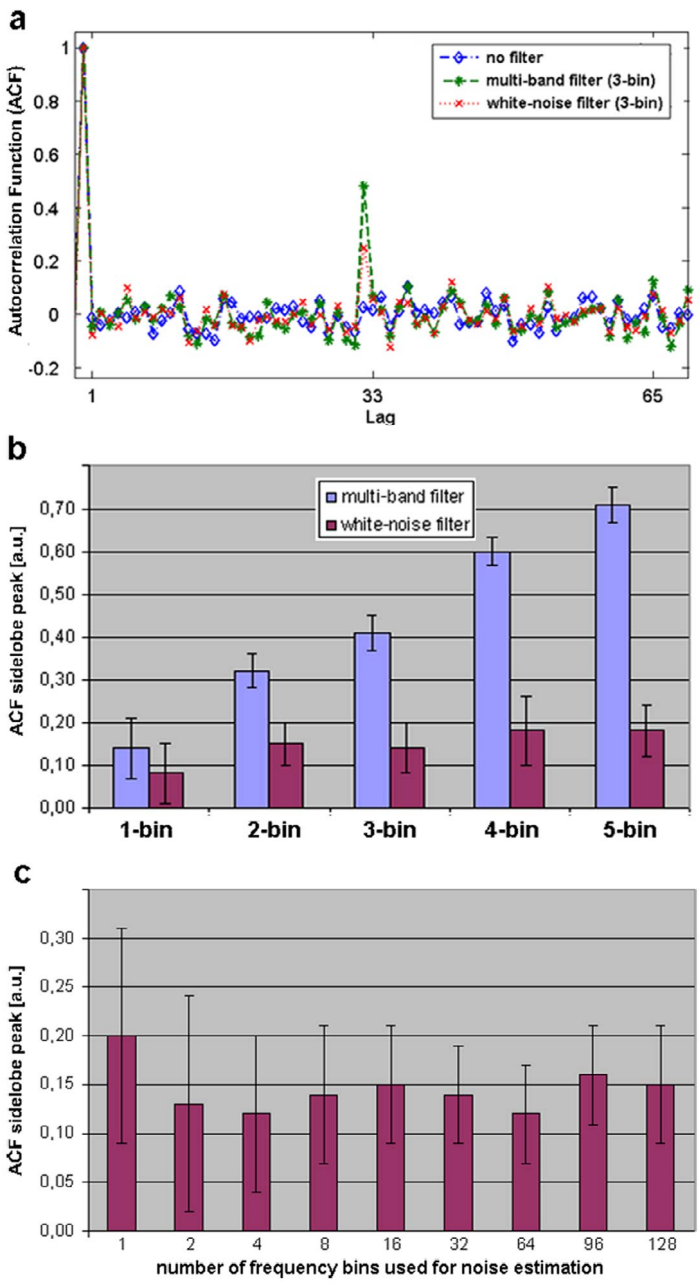

Figure 3.38 – Autocorrelation Function for Temporally Filtered Gaussian White Noise.
*(**a**) Lag 1-70 of the ACF of simulated white-noise applying no filter and respectively the multiband and white-noise filter 3-bin strategy. (**b**) Magnitudes of the characteristic side lobe peaks at lag 32, shown for the multiband 1-7 bin and white-noise filter 1-7 bin, respectively. (**c**) Magnitude of the side lobe peaks for the white-noise filter 3-bin using variable numbers of frequency bins in order to estimate the mean and the variance of the noise.*

T-value Distribution

The statistical parameter maps of the simulated active datasets are depicted in Figure 3.39. A clear distinction between the activated and the non-activated areas can be seen. It further shows that the number of true activated voxels and true false positive voxels clearly vary between the multiband and the white-noise filtered datasets and the unfiltered case.

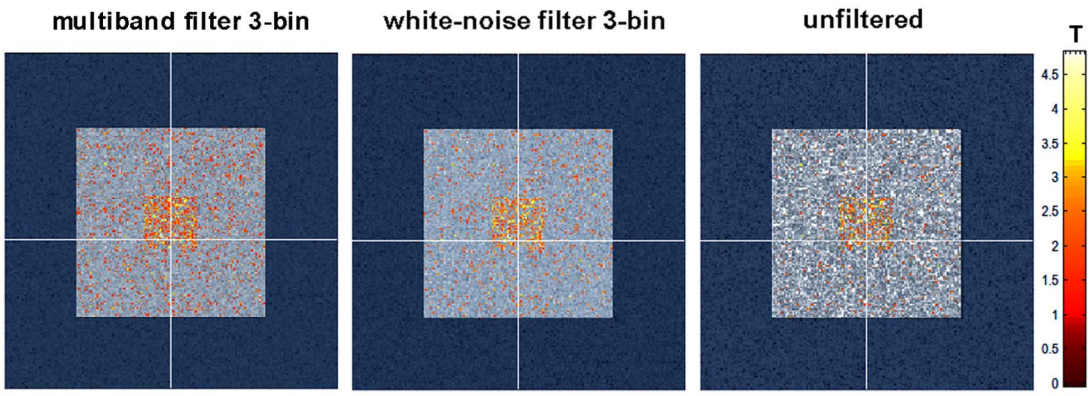

Figure 3.39 – Activation Maps from the Simulated fMRI Datasets.

To study this effect in more detail, the *t*-value distributions of the null datasets of both filter types were analyzed. Apparently, the width (i.e. standard deviation) of the *t*-distribution was generally smaller for the white-noise compared to the multiband filtering strategy (Figure 3.40 (a)). Moreover, using the multiband filter n-bin, the width of the *t*-distribution steadily increased for an increasing the number of removed bins. In contrast, when the white-noise filter n-bin was used, the width remained nearly constant for $n > 3$ (Figure 3.40 (b)).

At any given number of false positives counted in the null datasets, the number of significant voxels observed in the active datasets continuously decreased using the multiband filter n-bin when the number of bins (n) was increased (Figure 3.41 (a)). Using the white-noise filter, the number of activated voxels decreased compared to the use of no filter as well (Figure 3.41 (b)). However, the decrease was significantly less prominent compared to multiband filtering. Moreover, there was no further decrease for the white-noise filtering 3-bin, 4-bin, and 5-bin strategy. Accordingly, at the same actual significance level (i.e. same number of false positives) significantly more activated voxels were detected in the white-noise filtered datasets compared to the respective multiband filter datasets. For instance, comparing the 1-bin and the 3-bin strategy at a false posi-

tive rate of 1 %, the number of activated voxels increased by 6 % and 29 %, respectively, by using the white-noise filter.

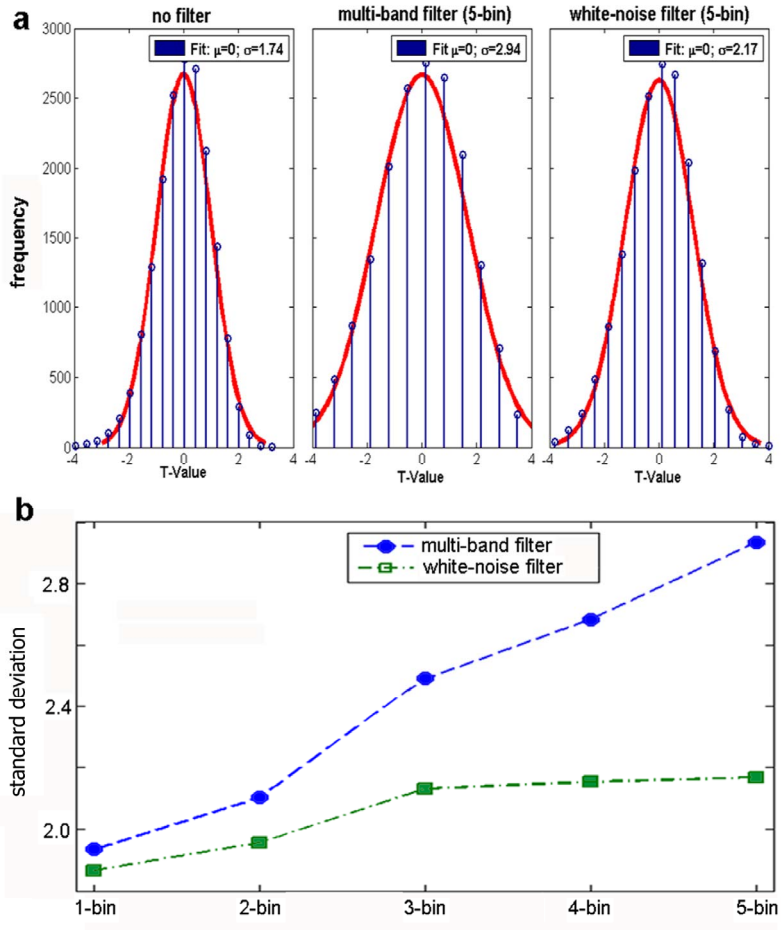

Figure 3.40 – Histogram of t-values Before and After Temporal Filtering.
*The t-value distributions were measured in the simulated null dataset containing Gaussian white noise. (**a**) T-distribution (blue circles) depicted for the unfiltered case and for the multiband filter 5-bin and white-noise filter 5-bin, respectively. The mean μ and the standard deviation σ of the t-distribution were estimated by fitting a Gaussian distribution (red solid line). (**b**) Standard deviation of the fitted Gaussian distribution shown for the 1-5 bin case using the multiband and the white-noise filter, respectively.*

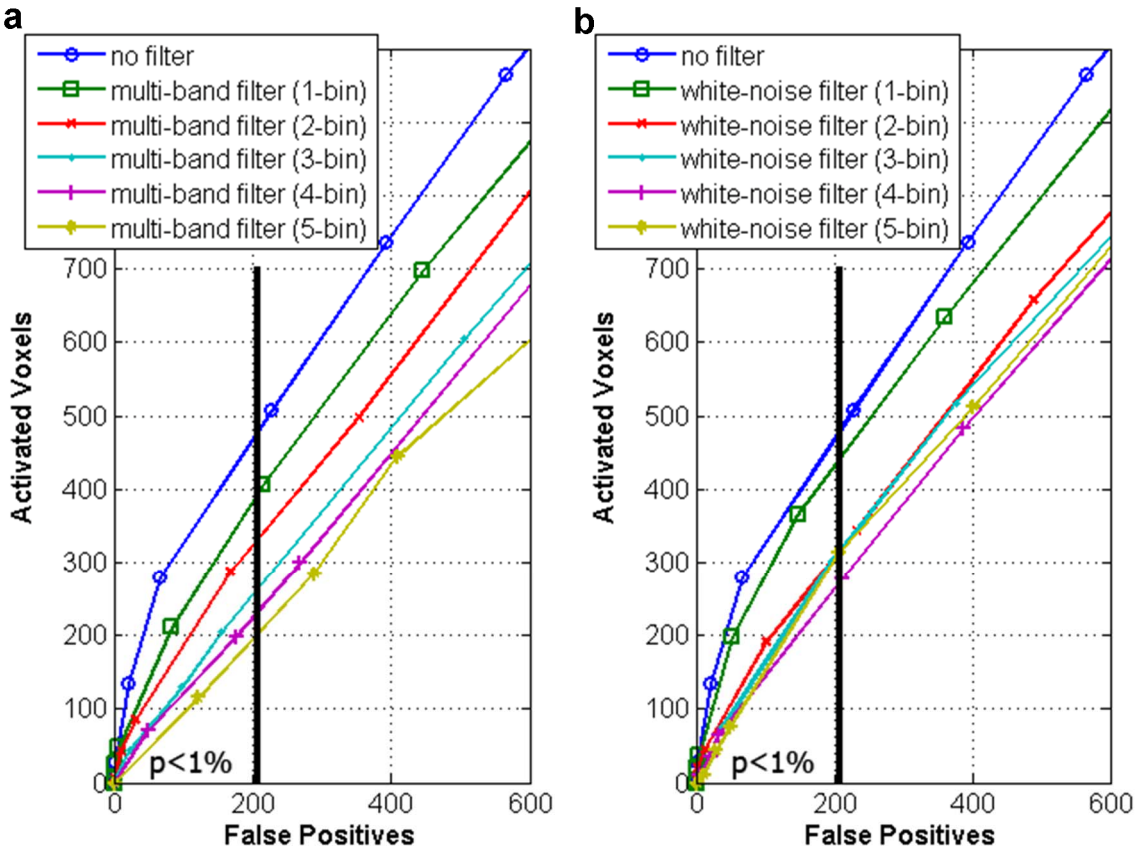

Figure 3.41 – Simulation Study: Modified ROC for Multiband and the White-Noise Filter.
*The horizontal (vertical) axis shows the number of false positives (activated voxels) detected in a simulated null- (activate) dataset using the multiband filter (**a**) and the white-noise filter (**b**). The significance level of $p < 1\ \%$ is indicated by the black vertical line.*

3.4.3 fMRI Experiment: Fingertapping Study

Five healthy subjects (25 ± 2 years) were scanned twice. In the first run of the experiment, a simple bilateral fingertapping task was performed with a total scan time of 13 minutes acquiring 256 image volumes (active dataset). In the second run, the same imaging parameters were used and the volunteers were scanned during the resting state i.e. where no fingertapping was performed (null datasets). The fMRI paradigm consisted of 52 repeating blocks. In the first 3 seconds of each block bilateral fingertapping was performed as instructed by short audio stimuli presented every 15 seconds. Phase trends were removed from the active and the null-datasets to narrow the aliasing peak width

(see Section 3.3.3.1). The temporally filtered datasets were post-processed and statistically analyzed as described in Section 2.4.2 and Section 2.4.3.

BOLD Activation in the SMC

The SMC was not subject to major impact of spatial aliasing artifacts when the 1-bin and the 3-bin strategy were used (Figure 3.42). However, other parts of the brain clearly show a severe degradation of the image quality. It can be seen that the spatial aliasing decreased with the number of removed bins. Apparently, the image quality was not noticeable changed when the white-noise filter was used.

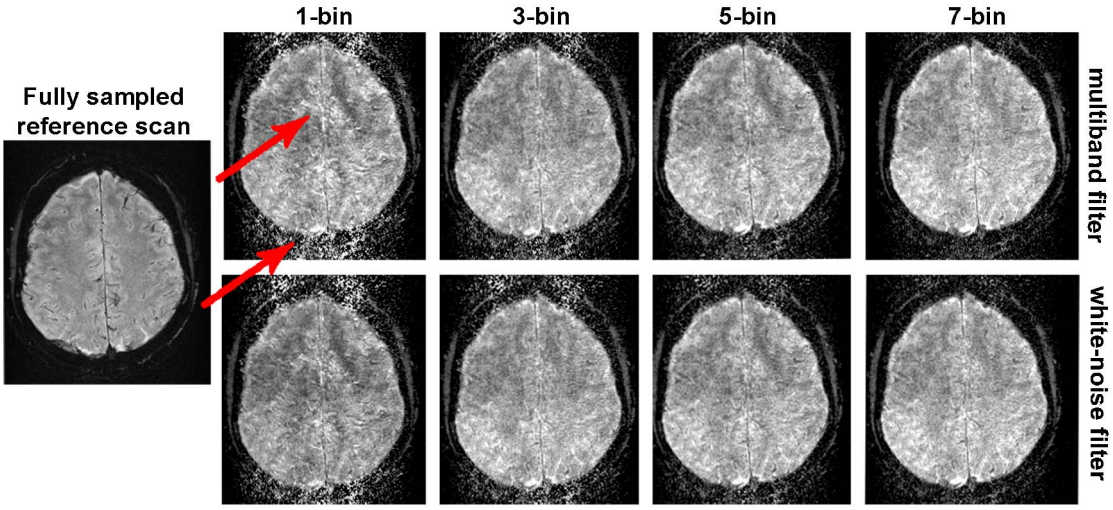

Figure 3.42 – Axial Slices Acquired with the 3D Segmented UNFOLD-EPI (R = 8).
The images (from left to the right) were obtained using the multiband (top) and the white-noise filter (bottom) 1-bin, 3-bins, 5-bins, and 7-bin strategy, respectively. Spatial aliasing artifacts are indicated by the red arrows. All images are contrasted equally. The data is depicted from a representative subject.

The SPM analysis result, as it can be depicted for a single subject in Figure 3.43, shows that the number of false positives was clearly decreased when the white-noise filter was used while the number of activated voxels detected in the SMC remained nearly the same. By using the 1-bin, 3-bin, and 7-bin white-noise compared to the multiband filter, the number of activated clusters, which can be clearly assigned to be false positives (i.e. outside the SMC), was reduced by 26 %, 57 %, and 20 %, respectively. For the 5-bin strategy the number of false positives was increased by 50 % with the white-noise filter

but in this special case the number of activated voxels inside the SMC was slightly increased.

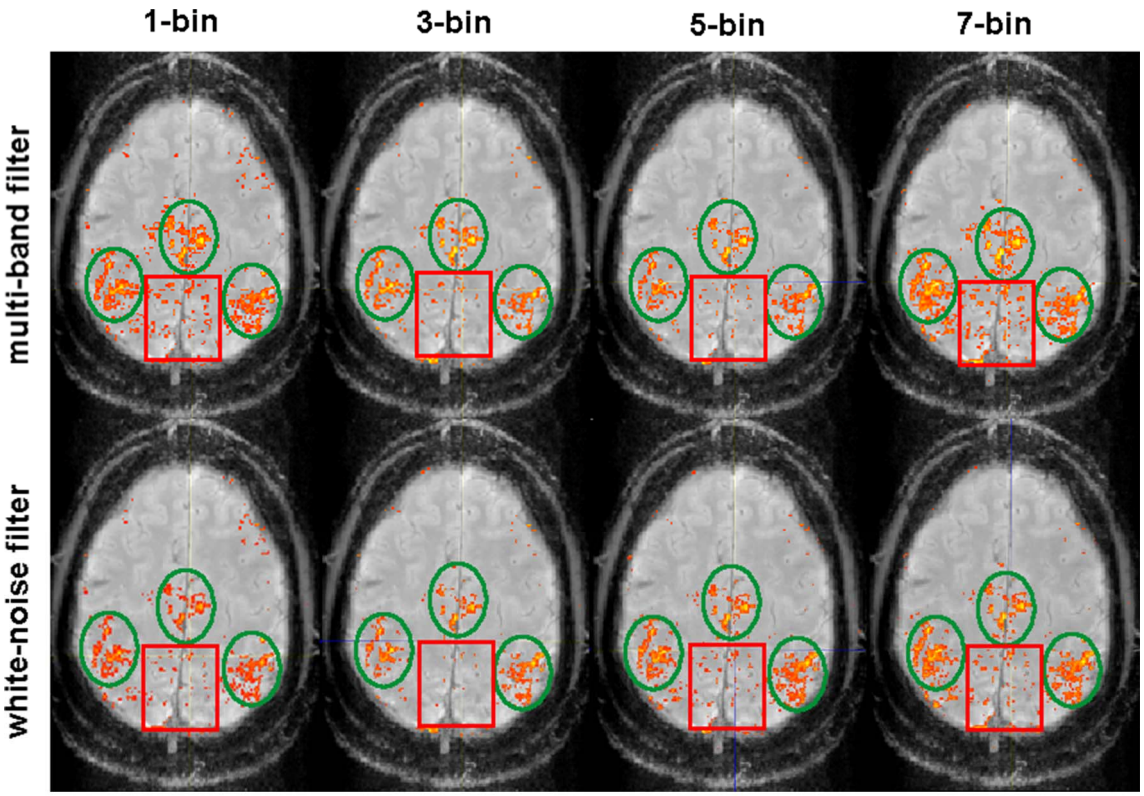

Figure 3.43 – Fingertapping Results using the Multiband and the White-Noise Filter.
The depicted data from a representative subject was thresholded at a nominal significance level of $p < 5$ % (uncorrected). Significant voxels are overlaid on the time series mean image acquired during fingertapping. Activated voxels outside the green circles are most likely false positives. The majority of them lies inside the red rectangle. There was no minimal cluster size used (i.e. $k \geq 0$) in order to emphasize false positive activations.

Linear Regression Analysis

The fingertapping experiment results for the active and the null datasets of all subjects were separately analyzed with linear regression, as exemplarily shown in Figure 3.44, for the 5-bin and 7-bin strategy. Within a confidence interval of 95 %, the number of false-positives detected in the null datasets was significantly reduced to 54 %, 89 %, 80 %, and 34 % by using the white-noise filter 1-bin, 3-bin, 5-bin, and 7-bin, respectively, compared the corresponding multiband filter n-bin. Furthermore, using the white-

noise filter, the number of activated voxels detected in the active datasets did not significantly depend on the filter for the 1-bin, 3-bin, and 5-bin strategy whereas for the 7-bin strategy the number of activated voxels was significantly decreased to 76 % by using the white-noise filter. For example, by using the 1-bin white-noise filter compared to the corresponding multiband filter, the number of activated voxels and false positives was reduced to 89 % and 54 %, respectively. Accordingly, the number of activated voxels per false positive was increased to 165 % (i.e. 89/54). Further results of the linear regression analysis are summarized in Table 3.5 for each n-bin filter. Except for the 3-bin filter, the percentage of activated voxels per detected false positive was significantly increased using the white-noise filter.

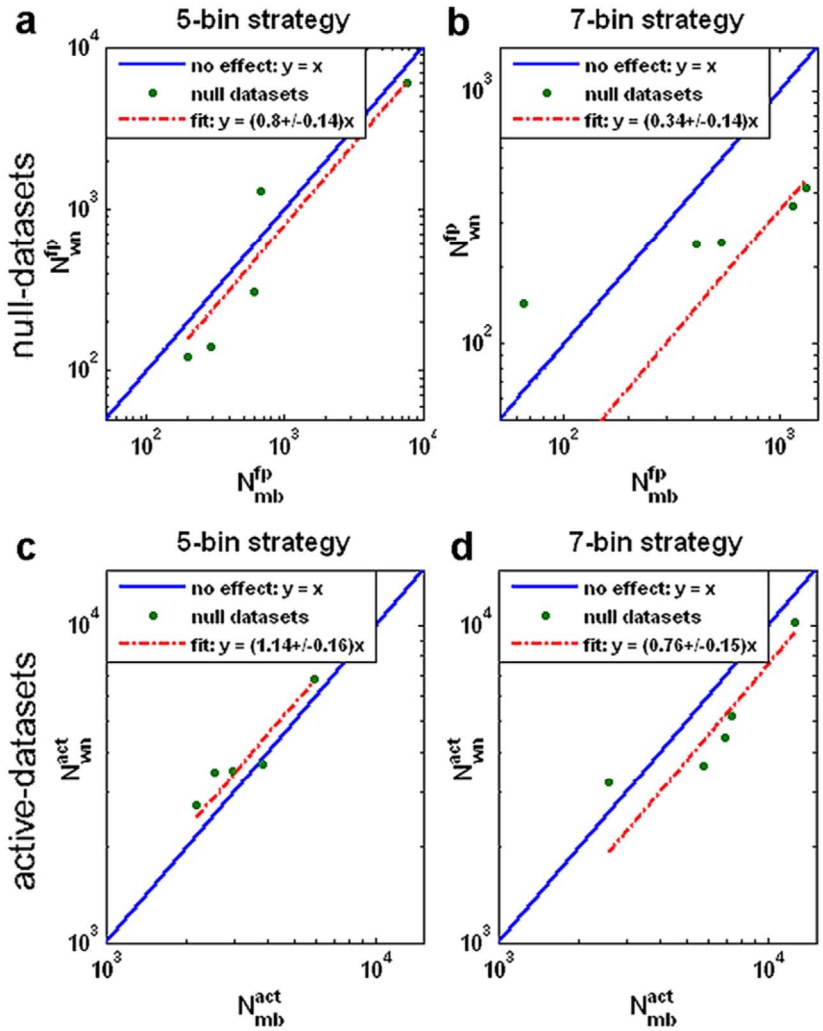

Figure 3.44 – Regression Analysis for the Multiband and the White-Noise Filter.
*Null-datasets: Total number of false positives (N^{fp}_{wn}) using the white-noise filter 5-bin (**a**) and 7-bin (**b**) versus the total number of false positives (N^{fp}_{wn}) using the respective white-noise filter. Active datasets: Total number of activated voxels (N^{act}_{wn}) using the white-noise filter 5-bin (**c**) and 7-bin (**d**) versus the total number of activated voxels (N^{act}_{mb}) using the respective multiband filter. The data was approximated by a linear fit, indicated by the red dashed line. For comparison, the angle bisector, which is the line of no effect, is indicated by the blue solid line. The fitting results and its 95 % confidence bounds are given in the legend of each graph. The number of significant voxels was counted at a significance level of p < 5 % (uncorrected). This analysis was performed for the 1-bin, 3-bin, 5-bin and the 7-bin strategy. For clarity, only the 5-bin and the 7-bin strategies are depicted.*

		1-bin	3-bin	5-bin	7-bin
a					
$N^{active}_{wn-filter} / N^{active}_{mb-filter}$	[%]	89 ± 23	81 ± 22	114 ± 16	76 ± 15
b					
$N^{falsepos.}_{wn-filter} / N^{falsepos.}_{mb-filter}$	[%]	54 ± 13	89 ± 6	80 ± 14	34 ± 14
c					
$\frac{N^{active}_{wn-filter} / N^{falsepos.}_{wn-filter}}{N^{active}_{mb-filter} / N^{falsepos.}_{mb-filter}}$	[%]	**165 ± 58**	**91 ± 25**	**143 ± 32**	**224 ± 102**

Table 3.5 – Statistical Inference using the Multiband and the White-Noise Filter.
*(**a**) Ratio of activated voxels (in the active datasets) using the n-bin white-noise and the corresponding multiband filter. (**b**) Ratio of false positives (in the null datasets) using the n-bin white-noise and the corresponding multiband filter. (**c**) Based on the ratios in the top and middle row, the ratio of activated voxels per false positive using the white-noise n-bin filter and the multiband filter n-bin, respectively. The errors in the bottom row were calculated according to the law of Gaussian error propagation.*

Receiver-Operator Characteristics

A more general overview of the filtering effects is provided by the modified receiver-operator characteristics (Figure 3.45). The mean number of activated voxels of all subjects was increased at any significance level for each n-bin case when the white-noise filtering approach was used. At a significance level of 5 %, the best improvement was achieved with the 1-bin white-noise filter compared to the 1-bin multiband filter increasing the number of activated voxels by 41 %. For the 3-bin, 5-bin, and 7-bin case, the number of activated voxels was increased by 5 %, 26 %, and 19 %, respectively. For the multiband and the white-noise filter, the highest performance was achieved with the 7-bin strategy. Comparing the multiband filter 1-bin to the 3-bin, 5-bin, and 7-bin strategy, the number of activated voxels was increased by 31 %, decreased by 33 % and increased by 113 %, respectively. Comparing the white-noise filter 1-bin to the 3-bin, 5-bin, and 7-bin strategy, the number of activated voxels was decreased by 8 % and 22 % and increased by 122 %, respectively.

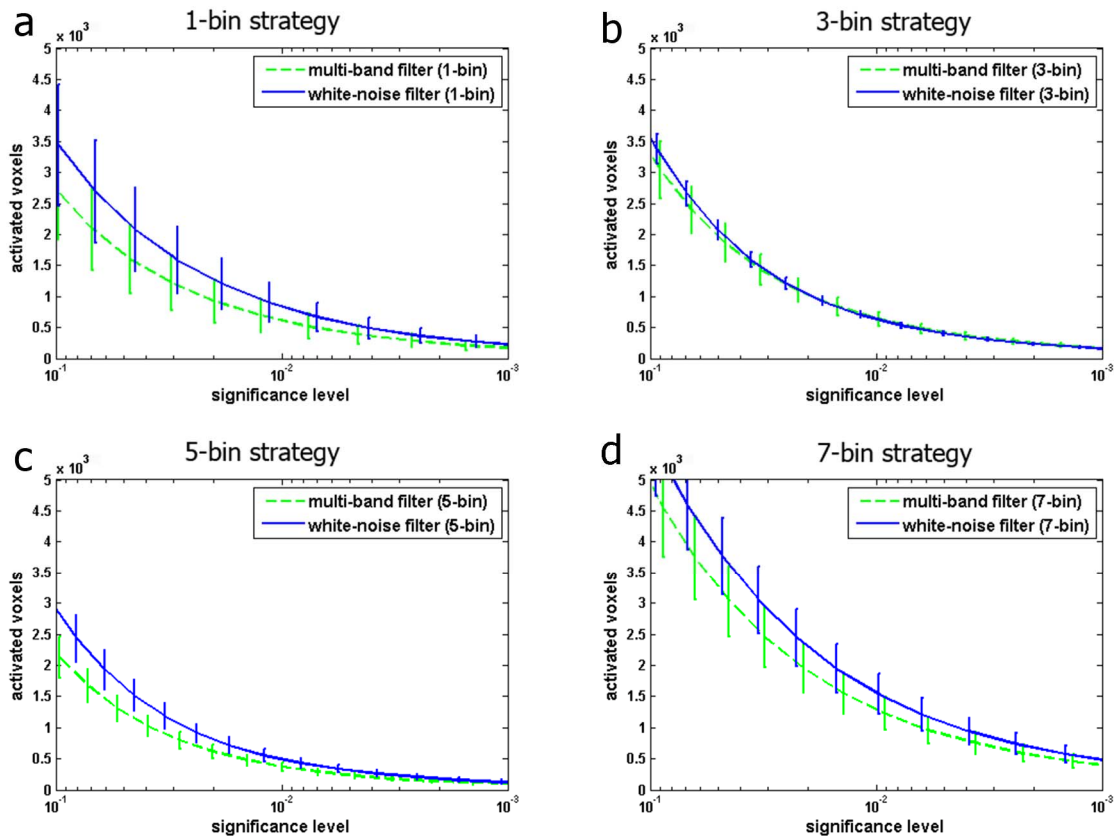

Figure 3.45 – Modified ROC for the Multiband and the White-Noise Filter.

Number of activated voxels found in the active datasets at significance levels in the range of $p \in [10^{-1}...10^{-3}]$ *shown for the 1-bin (**a**), 3-bin (**b**), 5-bin (**c**), and the 7-bin filter (**d**). The significance level corresponds to the number of false positives detected in the null-datasets divided by the total number of voxels inside the imaging volume. These values were obtained as the average of five healthy subjects. The error bars denote the standard deviation of the subjects.*

4 Discussion

Increasing BOLD Sensitivity using Slice-Dependent Echo Times

The goal of the present work was to demonstrate that the adjustment of echo times in single EPI slices improves BOLD sensitivity in the OFC. First, BOLD sensitivity simulations were performed to approximate optimal echo times for single EPI slices. Second, an EPI sequence with slice-dependent echo times was compared to an optimized EPI sequence with constant short echo time during an event-related fMRI experiment with focus on the OFC. Both, simulations and functional results indicate that BOLD sensitivity was increased when slice adjusted echo times are used.

In the inferior OFC, gradient strengths of more than 250 μTm^{-1} were observed, which is in agreement with the findings of DePanfilis and colleagues (2005). It was demonstrated that even moderate susceptibility gradients in the order of 150 μTm^{-1} shift the maximal BOLD sensitivity to echo times clearly below 30 ms. Both, BOLD sensitivity simulations and actual EPI measurements confirmed that a *TE* value of about 20 ms significantly reduces signal drop outs and increases BOLD sensitivity in inferior slices of the OFC. Further, it was observed that T_2*-relaxation times increase and field gradients decrease in foot to head direction. Therefore, short *TE* values of about 20 ms decrease the BOLD sensitivity in superior slices of the OFC. Accordingly, the numerically calculated optimal echo times averaged over all subjects increased with the slice number and were in the range of 17 ± 2 ms and 39 ± 2 ms. However, echo times below 20 ms are not realisable using an EPI sequence with standard imaging parameters (e.g. matrix size, bandwidth, Partial Fourier, PI factor, etc.). However, using a short *TE* value of 20 ms potentially preserves the BOLD sensitivity in the presence of strong in- and through-plane gradients of more than 300 μTm^{-1}. An important case-by-case analysis must be made with respect to the polarity of the in-plane gradients as described by Deichmann and colleagues (2002). The simulations performed in this work showed that a *TE* value of 22 ms is adequate to avoid signal loss caused by negative in-plane gradients of more than 300 μTm^{-1} whereas an echo time reduction is ineffective to recover signal loss due to positive in-plane gradients. Even moderate positive in-plane gradients of only 80 μTm^{-1} cannot be compensated via *TE* reduction because the gradient-echo is rapidly shifted outside the acquisition window with increasing gradient strengths. It was shown that an EPI with slice-dependent echo times between 22 ms and 37 ms significantly im-

proves statistical inference in the OFC on the single subject and on the group level compared to an optimized standard EPI with short *TE* of 27 ms.

The effectiveness of the modified EPI sequence might be further improved by changing the slice tilt to reduce in-plane gradients with positive signs as observed in the OFC. It has been previously shown that a tilt angle of 30° from the axial towards the coronal orientation yields the best choice to minimize signal drop outs in the OFC and thus to increase the BOLD sensitivity (Deichmann, et al. 2003). However, it should be noted that due to the shape of the brain, a transversal slice orientation yields time efficient volume coverage. The number of slices would potentially have to be increased when tilting the slices orientation away from a transversal toward a coronal orientation (Deichmann, et al. 2003) detrimental for the temporal resolution, which is particularly important in event-related fMRI studies. It has been experimentally demonstrated that the phase encoding scheme significantly affects susceptibility induced signal losses in EPI (De Panfilis and Schwarzbauer 2005). Hence, a slice-dependent change of the PE gradient additional to the *TE* variation could further improve fMRI in critical brain areas without affecting the temporal resolution.

It seems implausible that a reduction of *TE* in the standard EPI sequence could outweigh the benefits of using slice adjusted echo times. Using an echo time below 27 ms would mitigate susceptibility artifacts in inferior slices. But it has to be noted that activation detected with the modified EPI sequence was more robust in inferior and in superior slices acquired at echo times below and above 27 ms. As expected, the slices acquired at approximately 27 ms showed similar BOLD activation in both EPI datasets. It is very likely that this effect will occur for any fixed echo time. Moreover, most psychological studies require whole-brain coverage. For a shorter echo time, BOLD sensitivity would be non-optimal in cortical brain areas not affected by susceptibility gradients where robust activation is detected between 30-50 ms (Fera, et al. 2004). Parietal activation was seen in both EPI datasets whereas more significant voxels were found in superior slices scanned at *TE* values above 27 ms. This finding agrees well with the fact that parietal regions are not exposed to susceptibility gradients and therefore the BOLD peak should be above 30 ms.

It has to be discussed whether more detected activity equates to more accurate detection of neuronal activity. Large vessels (draining veins) in the vicinity of an activated region are a known source of false-positive voxels in gradient-echo fMRI where the BOLD signal consists of an intravascular and a dominating extravascular component. Duong

and colleagues (2003) reported that for high magnetic field strengths (i.e. 4 T and 7 T) the weak intravascular BOLD signal contribution of large vessels decreases with longer echo times. Whether this effect occurred at field strength of 3 T and whether it led to more false-positive voxels in inferior slices acquired with the modified EPI sequence only or in inferior slices acquired with both sequences remains unknown. However, in the context of research with several groups such as patients and controls this issue is of minor importance as effects of systematic errors like false-positive voxels cancel out. Yet, subtle differences might be detected more easily using a sequence more sensitive in the detection of signal change.

Despite a rather large variability of magnetic field gradients between different subjects, the simulation of optimal echo times in single slices showed consistent results over all subjects. Still, considering that susceptibility gradients will depend notably on the person's orientation inside the magnet, which cannot be identical from day to day, T_2*-fitting and gradient field mapping tools should be implemented on the MR scanner for individual echo time optimization directly before the fMRI experiment, as previously suggested by Stoecker and colleagues (2006). Individual gradient field maps could then additionally be used to remove EPI images distortions (Hutton, et al. 2002; Jezzard and Balaban 1995) to increase spatial accuracy especially in regions prone to susceptibility artefacts.

Besides echo time optimization in single EPI slices, multi-echo acquisition methods (Poser and Norris 2009; Poser, et al. 2006; Posse, et al. 1999; Speck and Hennig 1998; Weiskopf, et al. 2005) pose an alternative for whole-brain fMRI studies since the BOLD contrast is preserved in all areas. But it has to be noted that they compromise temporal resolution since the EPI readout train is prolonged. This lack of temporal resolution is detrimental for event-related fMRI studies and could only be compensated by decreasing spatial resolution since spatial coverage is indispensable in whole-brain fMRI. Recently, it has been shown that susceptibility induced BOLD signal dropouts and distortions are reduced when spatial resolution is increased in the EPI read out direction, which does not affect temporal resolution (Weiskopf, et al. 2007). Thus, this strategy could be combined with slice-dependent echo times to further reduce susceptibility artefacts in subcortical brain areas.

Improving Spatial Specificity in EPI using Parallel Imaging

In agreement with the *PSF*-simulations and the resolution-phantom measurements, the *in-vivo* images also showed that the in-plane resolution in EPI was continuously improved by increasing the matrix size (PI-factor) using a standard 12-channel head coil. To study whether the higher in-plane resolution is only a result from an increased spatial resolution in RO direction, EPI line profiles along the RO and the PE direction were compared to line profiles of a high-resolution T_2-weighted image. The comparison demonstrated an improvement of the spatial resolution in both directions.

Fingertapping Task – Single Subject Analysis

On the single subject level, the fingertapping experiment showed a trend to significantly decreased numbers of activated voxels and a mild reduction of the T^{max}-values when the matrix size (PI-factor) was increase. This finding is in consistence with the findings of Fellner and colleagues (2009). Considering the linear relationship between the *t*-values and the *SNR* (Parrish, et al. 2000), the significant reduction of the number of activated voxels is a consequence of the lower *SNR*. Previous studies (Frahm, et al. 1993; Moeller, et al. 2006; Newton, et al. 2012) suggest the decreased partial volume effect as the cause for the mild reduction in T^{max}. However, the BOLD spatial specificity was highly improved using e.g. the 192 x 192 (R = 4) compared to the 96 x 96 (R = 2) EPI protocol. Even though BOLD spatial specificity is limited by the blurring of the BOLD response itself (Shmuel, et al. 2007), draining veins (Olman, et al. 2007; Yacoub, et al. 2003), movement artifacts, and spatial smoothing, it was shown that the number of clusters and local maxima, detected at lower threshold levels, was significantly increased in the 192 x 192 (R = 4) compared to the 96 x 96 (R = 2) datasets.

The significant decreased number of activated voxels in single subjects for high matrix sizes suggests that the BOLD activation might be more separable as a consequence of fewer activated voxels. However, neither the number of clusters nor the number of local maxima in the low resolution datasets increased at higher statistical threshold levels. Hence, it is more likely that the superior separability of the BOLD activation observed at lower thresholds using increased matrix sizes (PI-factors) is in fact a consequence of the higher in-plane resolution which was observed. Moreover, a continuous decrease of the number of clusters and local maxima was seen in such a way that for higher thresholds approximately the same number of clusters and local maxima were detected in all datasets independent of the matrix size (PI-factor). This demonstrates that the most significant clusters and local maxima are detectable using a high-resolution EPI protocol

showing that detecting BOLD activation with high sensitivity does require sacrificing spatial resolution. In this aspect, it is important to note that using the 160 x 160 (R = 3) EPI protocol did not yield more separable BOLD activation compared to the 128 x 128 (R = 3) EPI protocol. This finding suggests two counteracting effects: On the one hand, activated clusters and local maxima are surpassingly more distinguishable at higher in-plane resolution. But on the other hand, the detection of clusters and local maxima requires robust BOLD activation in the first place which is significantly decreased at higher spatial resolution. Hence, the positive effects on BOLD separability gained by the increased in-plane resolution in the 160 x 160 (R = 3) dataset was most likely compensated by the reduced BOLD activation robustness compared to the 128 x 128 (R = 3) dataset. However, the fact that the BOLD activation in the 192 x 192 (R = 4) dataset was clearly more distinguishable compared to the 96 x 96 (R = 2) dataset shows that using higher in-plane resolutions improves the detection of activated clusters and local maxima in single subjects.

There was no trend of increased cluster edge-sharpness observable at higher in-plane resolutions. It was shown that the cluster edges in RO direction were sharper than in PE direction. This might reflect the higher resolution in RO direction due to the shorter signal read out compared to the PE direction and consequently decreased spatial blurring. In this aspect, it should be mentioned that the spatial specificity is generally compromised by spatial smoothing probably preventing increased cluster sharpness for high matrix sizes (PI-factor). However, spatial smoothing cannot be omitted in high-resolution fMRI because of the lower *SNR* inherently decreasing the robustness in the detection of BOLD activation, as observed in single subjects. Furthermore, at higher spatial resolutions physiological noise is less dominant compared to lower spatial resolutions. Thus, at higher spatial resolutions spatial smoothing is more effective to increase the *SNR* and therefore the BOLD sensitivity (Triantafyllou, et al. 2006). On the other hand conventional spatial smoothing can also decrease BOLD sensitivity if a few activated voxels are averaged with many non-activated voxels, which is particular prominent in small brain areas. To avoid this effect, Tabelow and colleagues (2009) proposed an ‘adaptive’ smoothing algorithm which iteratively averages only the activated voxels. In the context of high-resolution fMRI, adaptive smoothing should be rather used than conventional smoothing to increase BOLD sensitivity without sacrificing spatial specificity.

Fingertapping Task – Group Analysis

The significant loss of activated voxels observed on the single subject level between the 96 x 96 (R = 2) and the 128 x 128 (R = 3) datasets most likely caused the reduced T^{max}-value. However, the group analysis showed a trend of increasing T^{max}-values and numbers of activated voxels comparing the 128 x 128 (R = 3), 160 x 160 (R = 3), and the 192 x 192 (R = 4) datasets. The BOLD activation on the group level not only depends on the BOLD activation in single subjects but also on the inter-subject variability. Hence, the trend of increasing BOLD activation is expected to results from the reduced inter-subject variability of the BOLD activation apparent for increased matrix dimensions. Since the T^{max}-value and the number of activated voxels were significantly increased in the 192 x 192 (R = 4) compared to the 96 x 96 (R = 2) dataset, the reduced inter-subject variability of the BOLD activation should overcompensate the detrimental effects of the lower *SNR* in the datasets acquired at smaller voxel sizes and higher PI-factors.

The highest number of clusters was detected in the 192 x 192 (R = 4) dataset and the lowest number of clusters in the 96 x 96 (R = 2) dataset. However, in contrast to the single subject level, the spatial BOLD specificity is anticipated to suffer from more pronounced deterioration caused by additionally blurring due to anatomical differences between different subjects (Crinion, et al. 2007). Hence, the positive effects on the detectability of activated clusters and local maxima at higher in-plane resolutions should be weaker on the group level. Therefore, it is reasonable to hypothesize that the significant increase of activated clusters in the 192 x 192 (R = 4) compared to the 96 x 96 (R = 2) dataset is not only related to the higher spatial resolution but also to the higher number of activated voxels. In support of this hypothesis, the lowest numbers of activated voxels was observed in the 128 x 128 (R = 3) datasets also revealing the lowest number of local maxima at nearly all threshold levels. An “optimal” threshold level was observed using the 128 x 128 (R = 3) EPI protocol, where the significantly highest numbers of local maxima was detected. Nonetheless, the single subject and the group analysis data presented in this work generally show that the BOLD activation separability either remains the same or improves by increasing the matrix size (PI-factor).

In contrast to the single subject results, significantly increased cluster sharpness was observed on the group level for larger matrix sizes (PI-factor). This suggests improved spatial alignment of the activated brain areas in different subjects. At field strength of 1.5 T, Fellner and colleagues have shown for EPI with standard voxels size and without

PI, that geometric distortions due to field inhomogeneities are in the order of a few millimetres even within a relatively homogeneous brain area as the precentral gyrus (Fellner, et al. 2009) which the SMC is part of. Furthermore, their data show that such geometric distortions highly vary between different subjects. Hence, on the group level, geometric distortions should compromise spatial overlaps of activated brain areas causing extra functional blurring. It was also shown that either increasing the PI-factors or the spatial resolution independently significantly reduces such geometric distortions by up to 1.5 mm. In the present 3 T study, where geometric distortions are more pronounced, both the PI-factor and the spatial resolution were increased simultaneously which potentially reduces geometric distortions even more effectively. A distortion reduction in the order of 1-2 mm may considerably improve spatial overlaps of activated brain areas in different subjects, considering the spatial resolution of 1-2 mm. Reduced geometric distortions are a potential source for the increasing T^{max}-values, the increasing numbers of activated voxels and the increased cluster sharpness observed in the group analysis. Moreover, considering that geometric distortions highly vary between subjects, reduced distortions might even explain the reduced inter-subject variability of the number of activated voxels which was observed on the single subject level. Standard unwarping methods were previously proposed to reduce such geometric distortions in fMRI. A single field map is usually acquired at the beginning of an fMRI session to estimate the dynamic field changes due to subject movements from the image realignment parameters. However, the spatial accuracy of these standard methods is limited to the order of 2 mm (Jezzard and Balaban 1995). More advanced distortion correction methods have been developed to increase the spatial accuracy e.g. by using a dual echo EPI updating the field map with each EPI scan (Hutton, et al. 2002) or by using a phase labeling algorithm (Xiang and Ye 2007). However, both methods either compromise temporal resolution crucial to detect transient signal modulations in event-related fMRI studies or require sophisticated sequence programming. Hence, besides the general benefits of higher spatial resolutions, increasing the matrix size in combination with the parallel imaging factor might be more eligible to reduce geometric distortions in EPI.

Motivation-Task Study

In the presented motivation-task study, it was demonstrated that robust fMRI using EPI at high in-plane resolution is also feasible in a sophisticated experimental design. The in-plane resolution was clearly improved by increasing the matrix size (PI-factor) from 96 x 96 (R = 2) to 160 x 160 (R = 3) using the 32-channel head coil. In consistence with

the findings of the fingertapping study, slightly reduced T^{max}-values and significantly reduced numbers of activated voxels were observed in the NAcc on the single subject level when the matrix size (PI-factor) was increased. Also a reduced inter-subject variability of the BOLD activation was observed in the 160 x 160 (R = 3) dataset which probably led to the slightly increased T^{max}-value and the nearly compensated number of activated voxels in the group analysis. Considering similar BOLD activation robustness on the group level in both datasets and the increased numbers of clusters and local maxima in the 160 x 160 (R = 3) compared to the 96 x 96 (R = 2) dataset supports the finding that higher in-plane resolutions leads to more distinguishable BOLD activation indicating improved spatial specificity of BOLD activation.

Detecting distinguishable brain activations in small brain regions is of great importance in cognitive neuroscience. The target region of the motivation-task study was the NAcc, which is a major part of the ventral striatum and plays a central role in the mesolimbic reward circuit (Knutson, et al. 2001) and in the development and maintenance of addiction (Everitt and Robbins 2005). Animal work suggests that two components of the NAcc, namely the core and the shell, have differential functions (Everitt and Robbins 2005; Zahm 1999). Whereas the shell mediates the acute effects of primary reinforcers or unconditioned cues ("motivational valence"), the core seems to be more involved in evaluating the "motivational value" of conditioned cues or secondary reinforcers and is responsible for sensory motor integration and the regulation of goal-directed behaviour. In the high-resolution EPI data of the motivation task study, activation clusters appear more distinguishable and less blurred compared to the standard EPI data. This can be seen for example in the coronal slices of the group activation maps where the 96 x 96 (R = 2) datasets detected only one cluster in each hemisphere whereas the 160 x 160 (R = 3) datasets revealed two clusters with separable local maxima in each hemisphere. The lateral cluster might correspond to the NAcc core region and the medial cluster might be located in the NAcc shell region. However, in humans, the separation of shell and core is not as clear as in animals, on the histological as well as the functional level. At the moment, there is only one study in humans examining this topic using fMRI in pain processing (Aharon, et al. 2006). However, the authors suggest using higher field strength and a better spatial resolution in future studies. In this motivation task study, activation of the NAcc shell was expected since studies in rodents suggest the NAcc shell to be activated during reward anticipation (Ikemoto and Panksepp 1999). But NAcc core activation is also reasonable because participants viewed a cue announcing the secondary reinforcer money. The results of this motivation-task study indicate that

with the proposed 160 x 160 (R = 3) EPI protocol, small brain regions might be functionally more separable than with the standard 96 x 96 (R = 2) EPI protocol. Nevertheless, further studies should use experimental paradigms clearly activating the NAcc shell and core separately during different conditions.

Feasibility of fMRI at Ultra-High Spatiotemporal Resolution

It was sought to develop methods to facilitate fMRI at high spatiotemporal resolution. In a first step, a 2D-Multislice and a 3D Segmented EPI were implemented and tested in phantom measurements. Then a phase detrending algorithm was implemented to reduction temporal coherences between time series images detrimental for statistical analysis of fMRI signals. Finally, the feasibility of fMRI at sub-millimeter voxel size and high temporal resolution was demonstrated.

None of the studied sequences suffered from apparent image quality degradation caused by UNFOLD, if the aliasing peaks were completely removed. The *SNR* was significantly increased with 3D imaging instead of 2D-multislice for slab sizes typically used in fMRI to achieve sufficient spatial coverage. Since high *SNR* is essential for the detection of small BOLD signal variations, 3D imaging should be chosen over 2D. The resolution-phantom images showed no difference between the 3D type 1 (i.e. UNFOLD in one dimension) and type 2 (i.e. UNFOLD in two dimensions) sequences with respect to aliasing artifacts or spatial resolution. However, for a given acceleration factor, performing UNFOLD in two dimensions might be preferable because each dimension is less undersampled and therefore the image is less intensely folded along this particular dimension. The degree of spatial overlaps is irrelevant to unfold stationary signals. However, overlapping dynamic signal components are not recoverable with UNFOLD (see Section 2.3.2). If the BOLD activation is mainly concentrated in a single slice, which is typically the case for a fingertapping experiment with axial slice orientation, a high undersampling factor in only one dimension, e.g. the PE-direction, increases the chance that activated voxel overlap, preventing detection. Using UNFOLD in two dimensions reduces the risk of overlapping activation in this scenario, since the non-activated overlapping slices located above and below do not hamper the detection of BOLD activation. However, in more complex fMRI studies involving various activated brain areas, homogeneously distributed over the whole imaging volume, UNFOLD in two or one dimension is expected to perform comparable.

UNFOLD datasets show shifted and broadened aliasing peaks resulting from linear and quadratic phase drifts due to signal instability and scanner imperfections (Hu 2011). It

was demonstrated that the phase detrending algorithm developed in this work effectively narrowed the aliasing peaks in UNFOLD datasets decreasing the first side lobe of the temporal *PSF* (i.e. the impulse response function of the classical multiband filter used) by 66 % indicating highly decreased temporal coherence.

The results suggest that fMRI with event-related functional experiments at ultra high spatial and temporal resolution is feasible with a Cartesian T_2*-weighted acquisition sequence in combination with UNFOLD. It was shown that artifact-free high-resolution morphological images can be acquired using UNFOLD. Furthermore, it was demonstrated that activation can be reliably detected in the SMC associated with finger tapping even though event-related paradigms provide weaker BOLD contrast compared to conventional block design studies (Moeller, et al. 2006). In the presented study, periodic stimuli were used. Therefore, spectral components of an activated voxel can be easily separated from aliasing components allowing high acceleration factors with UNFOLD. In future work, this technique will be applied to more complex cognitive paradigms without a fixed stimulus frequency, which might require more sophisticated temporal filtering strategies to detect BOLD activation, despite the presence of UNFOLD aliasing peaks.

Increased Statistical Inference in UNFOLD fMRI with Novel Filter

The key objective was to demonstrate that the proposed filtering strategy reduces autocorrelated noise, decreases false positive rates, and increases the number of activated voxels. The simulations clearly indicated that deleting a number of frequency components and their harmonics (i.e. setting them to zero) of a Gaussian white-noise spectrum leads to increased side lobe peaks of the autocorrelation function. This effect gets more evident with a higher number of removed frequency components. With the white-noise n-bin filter, the side lobe peaks are significantly reduced and remain stable even for high n-bin strategies. Previous publications have shown that autocorrelations due to physiological fluctuations affect the probability of false positive voxels (Purdon and Weisskoff 1998; Smith, et al. 2007; Zarahn, et al. 1997). The simulations presented in this work showed the same effect for the auto-correlations introduced by standard multiband filtering. The width of the *t*-distribution of the null datasets increased in correlation with the number of removed frequency components when the multiband filter was used. The width of the *t*-distribution of the white-noise filtered null datasets was significantly smaller and also remained constant for an increasing number of removed frequency

components (i.e. n-bin strategies). In conclusion, the simulations showed that white-noise filtering reduces the number of false-positives at any given nominal threshold.

This finding was supported by the fMRI measurements, which contain significantly less false positive voxels at any given nominal threshold using the white-noise compared to the multiband filtering strategy. At the same time, the number of activated voxels detected in the active datasets was slightly but not significantly reduced with the white-noise filter. However, in fMRI studies the reduction of *SNR* and the associated loss of activation were insignificant probably due to the dominating physiological noise. In the simulation study without physiological noise, the difference was more prominent (not shown). However, the linear regression analysis clearly showed that the slightly decreased number of activated voxels in the fingertapping datasets was overcompensated by the clearly decreased number of false positives.

In accordance with the simulations, the mean ROC improved at any given significance level by using the white-noise n-bin filter compared to the corresponding multiband filter. However, for a false positive rate of 5 %, significant improvements using the white-noise filter were only observed for the 1-bin, 5-bin, and 7-bin cases. At this false positive rate, the number of activated voxels was not significantly improved when the 3-bin white-noise filter was used. Nonetheless, significance was shown for lower thresholds (i.e. $p > 5$ %).

The superiority of the white-noise was probably hampered by the low *SNR* caused by the small voxel size in combination with the high UNFOLD acceleration. If the *SNR* is too low, BOLD activation cannot be detected and thus the number of activated voxels in the active datasets approximates the number of false positives in the null dataset. Hence, the number of activated voxels per false positive converges to 1 for any kind of temporal filter used. Thus, the difference between the filtering strategies vanishes for low *SNR* levels. Accordingly, the white-noise filtering strategy is expected to outperform the multiband filtering strategy even more at higher *SNR* levels. The rather poor number of activated voxels detected in some subjects and thus the large variance between the subjects indicates that high UNFOLD acceleration factors are not recommendable at sub-millimeter voxel size. Although the white-noise filter technique showed clear improvement of fMRI results, clinical studies with an optimized paradigm and optimized acceleration factors should be performed to establish the benefit of this technique over existing clinical studies.

The simulations predict that the number of activated voxels detected at a given significance level decrease for the multiband n-bin and the white-noise n-bin filter when the parameter n is increased (i.e. more frequencies filtered out). There was no clear trend observed in the fMRI datasets, possibly because of low *SNR*, small sample size, and insufficient removal of the aliasing peaks for smaller n-bin strategies causing too much variance in the data. This assumption is supported by the fact that for the 1-bin and 3-bin multiband and white-noise filter, the images were severely affected by aliasing artifacts. However, there is no obvious reason why the number of activated voxels was again slightly decreased for the 5-bin case since aliasing was completely removed in the images. Surprisingly, the performance was significantly increased for the multiband 7-bin and the white-noise 7-bin filter. This could possibly be explained by the fact that compared to the 1-bin, 3-bin, and 5-bin filters, the 7-bin filter eliminated physiological noise located nearby the aliasing peaks (e.g. an aliased heart beat signal). With the presented results, it remained unclear which n-bin filter generally performs best but there is the indication that the aliasing peaks should rather broadly be removed ensuring the proper elimination of aliasing artifacts before statistical mapping of the activation is performed. However, more experiments are warranted to clarify this point.

As discussed before, it was demonstrated that the white-noise filtering strategy effectively reduces serial correlations and consequently increases statistical inference in fMRI datasets acquired with UNFOLD. It was shown that the noise estimation algorithm presented for the white-noise filtering strategy is robust with regard to the number of frequency bins used for the determination of the noise level. This finding is fundamental in the context of high UNFOLD acceleration factors in combination with a small number of time series images. In this case, the UNFOLD peaks are packed more densely in the power spectrum and only few noise components remain, which can be used for the noise estimation. The white-noise filter algorithm can potentially be further improved by e.g. locating and eliminating detrimental noise components resulting from physiological fluctuations biasing the noise estimation. Moreover, the algorithm replaces the aliasing peaks by Gaussian white noise which is justified since the Fourier transform of Gaussian noise in the time domain should also be Gaussian in the frequency domain. However, as stated by Marchini and Ripley (2000), the noise distribution in fMRI datasets is best described by a Gumbel distribution. Therefore, replacing the aliasing peaks with Gumbel distributed noise could have a positive effect on the remaining autocorrelation in the white-noise filtered datasets.

White-noise filtering would not outperform multiband filtering if the standard prewhitening AR(1) model would completely eliminating non-white noise related to multiband filtering. A basic assumption of the AR(1) model is that if the autocorrelation of the noise is exactly known there exists an invertible smoothing matrix than can be used to prewhiten the noise (Seber 1977). Even if the smoothing matrix is known, this linear operation would fail to recover the noise if the aliasing frequency components are zeroed. This is caused by the fact that the spatial aliasing caused by UNFOLD and the measurement noise cannot be discriminated at the given frequencies. Hence, a complete removal of the UNFOLD peaks is only possible, if the noise is cancelled out as well. The reason why the AR(1) model also failed when the white-noise filtering strategy was used has to do with the estimation of the autocorrelation of the noise. With the AR(1) model only the first coefficient of the autocorrelation function of the noise is used to create the smoothing matrix since for most cases only the first coefficient significantly differs from zero (Bullmore, et al. 1996). However, the simulation indicated that multiband and white-noise filtering create multiple significant autocorrelation side lobe peaks not considered for in the AR(1) model. It would be important to consider more coefficients or at least the coefficient of the side lobe peak to estimate the autocorrelation of the noise in the context of UNFOLD. Hence, an AR model of higher order in combination with the white-noise filtering strategy should yield superior results.

In conclusion, it was successfully shown that an EPI sequence with slice-dependent echo times yields superior statistical inference in the OFC compared to an optimized standard EPI sequence with a reduced echo time. With respect to BOLD spatial specificity, the 128 x 128 (R = 3) or the 160 x 160 (R = 3) EPI protocols might yield a good compromise between specificity and sensitivity on the single subject level and should therefore be suitable for clinical applications such as preoperative planning and neuronavigation (Sunaert 2006; Vlieger, et al. 2004; Wurm, et al. 2008) ideally requiring both, high spatial specificity and sensitivity. With focus on fMRI research studies targeting to make global inferences about groups of participants rather than single subjects, the presented fMRI results show for the first time that conventional matrix sizes (PI-factors) used in EPI at clinical field strength of 3 T are non-optimal sacrificing spatial BOLD specificity. It may be recommend using the proposed 192 x 192 (R = 4) EPI protocol, which turned out to be applicable in detecting more robust BOLD activation on the group level with higher spatial specificity. Combining the proposed high-resolution EPI protocols with slice-dependent echo times could be used to increase both, spatial

specificity and BOLD sensitivity. Using small echo times in the lower slices requires shorter signal read outs. The proposed 160 x 160 (R = 3) and the 192 x 192 (R = 4) EPI protocol use moderate bandwidths and no Partial Fourier. Thus, the read out duration could be easily adapted to shorter echo times by either increasing the bandwidths and/or by additionally using Partial Fourier. Another strategy to improve BOLD sensitivity is to increase the *SNR* by adapting the proposed high-resolution protocols to a 3D EPI sequence. Combined with an optimized coil setup (e.g. 32-channel head coil) facilitating higher PI-accelerations, larger matrix sizes could be acquired to further increase spatial specificity. Moreover, it was successfully demonstrated that combining a segmented EPI sequence with the UNFOLD method facilitates the robust detection of BOLD signals in fMRI on sub-millimeter scales with high temporal resolution and spatial coverage. Last but not least, it was shown that statistical inference using UNFOLD significantly improves with the proposed white-noise filtering strategy. Recently, the Multiplexed-EPI sequence using multibanded simultaneous slice excitation (Feinberg, et al. 2010; Moeller, et al. 2010) has been suggested and is considered to be a promising approach for substantially increasing the image acquisition speed as it enables significantly higher acceleration rates compared to conventional methods. The Multiplexed EPI has been successfully tested in fMRI at 7 T reaching acceleration factors up to R = 36 enabling whole-brain acquisition within 400-800 ms at 2.5 mm isotropic resolution. However, the multiplexing strategy has not been combined with a high-resolution segmented EPI technique, yet. This novel approach could potentially revolutionize fMRI at sub-millimeter spatial resolution allowing rapid whole-brain acquisitions within 1-2 s.

5 Summary and Outlook

Single-shot EPI is commonly used in fMRI due to the intrinsic T_2^*-contrast, high temporal resolution, and spatial coverage. However, major drawbacks using EPI are limited spatial specificity due to blurring and distortions as well as signal cancellation in areas affected by susceptibility gradients, such as the OFC. Segmented EPI techniques facilitate high spatial specificity but are rarely used in fMRI due to insufficient temporal resolution or spatial coverage. In the first part of this work, two independent strategies were developed to reduce signal loss and increase BOLD sensitivity in EPI with focus on the OFC and to improve BOLD spatial specificity throughout the brain. In the second part of this work, the main goal was to develop a high-resolution sequence to enable fMRI at sub-millimeter scales and high temporal resolution. The final objective was to improve statistical inference essential for the robust detection of BOLD activation at high spatiotemporal resolution.

To increase BOLD sensitivity in the OFC, an EPI with slice-dependent echo times was developed. Simulations were performed showing that optimal echo times in slice direction vary between 20 ms and 40 ms supporting the idea of separately adjusting the echo time for each slice. Furthermore, during an event-related fMRI experiment an EPI with slice-dependent echo times covering the OFC between 22 ms and 37 ms was compared to an optimized EPI sequence with a constant echo time of 27 ms. By using the EPI with slice-dependent echo times, the single subject results revealed that the number of activated voxels in the OFC was on average increased by a factor of 6.3 while the maximal *t*-value was also increased by a factor of 1.2. Furthermore, OFC activation was detected in all subjects using the modified EPI but only in 50 % of the subjects using the standard EPI sequence. In agreement, the group analysis results showed significantly improved BOLD activation in the OFC when slice-dependent echo times were used.

To improve the BOLD spatial specificity using EPI, the matrix size and the PI-factor were increased beyond conventional parameter settings used at the clinical field strength of 3 T. The EPI protocols were tested in two separate fMRI studies: A simple motor-task experiment using matrix sizes (PI-factors) between 96 x 96 (R = 2) and 192 x 192 (R = 4) and a sophisticated motivation-task study using a standard 96 x 96 (R = 2) and a high-resolution 160 x 160 (R = 3) EPI protocol. The phantom and the *in-vivo* images revealed clearly more structural details using the proposed high-resolution EPI protocols in combination with the standard 12-channel head-coil. As expected, the benefits using

larger matrix size (PI-factors) were even more pronounced using the optimized 32-channel head-coil. In congruence, the fMRI results suggest more distinguishable BOLD activation in terms of increased numbers of clusters and local maxima on the single subject and also on the group level when the matrix size (PI-factor) was increased: I.e. by using the 192 x 192 (R = 4) protocol, the number of clusters (local maxima) in the SMC was increased by a factor of 1.5 (1.7) on the single subject level and by a factor of 2.7 (1.4) on the group level compared to using the 96 x 96 (R = 2) protocol. Furthermore, the edge-sharpness of activated clusters, measured by the slope of the $t(x)$-profile, was increased by a factor of 2.0 (2.2) in PE (RO) direction. In agreement to the findings of the fingertapping study, the number of clusters (local maxima) in the NAcc detected in the group analysis of the motivation-task increased by a factor of 1.4 (1.2) by increasing the matrix size (PI-factor) from 96 x 96 (R = 2) to 160 x 160 (R = 3). In single subjects, it was observed that the T^{max}-values were slightly decreased and the number of activated voxels significantly decreased. Nonetheless, on the group level both fMRI experiments independently showed increased T^{max}-values and increased numbers of clusters and local maxima in the high-resolution datasets which indicates that the BOLD activation is more robust and spatially more distinguishable using the proposed high-resolution EPI protocols.

To facilitate fMRI at sub-millimeter spatial and high temporal resolution, a segmented EPI was combined with the UNFOLD acceleration technique. It was shown that the image quality was not affected by UNFOLD as long as the spectral aliasing peaks were broadly removed. However, temporal filtering required by the UNFOLD method induces serial coherences. A phase-detrending algorithm was implemented effectively narrowing the aliasing peaks. Thus, reduced temporal filtering was necessary to remove the aliasing energy introducing less temporal coherence which was indicated by a reduction of 66 % of the temporal *PSF* side lobe. Finally, the feasibility of fMRI at high spatiotemporal resolution was demonstrated in an event-related fingertapping experiment. It was shown that artifact-free high-resolution morphological images can be acquired at high UNFOLD acceleration (R = 8). Furthermore, it was demonstrated that robust BOLD activation can be detected in the SMC associated with a fingertapping task.

To improve the statistical inference in UNFOLD datasets, a novel filtering strategy, the "white-noise filter" was proposed which was compared to multiband filtering in a simple fingertapping fMRI experiment. It was shown that simple multiband filtering leads to temporal autocorrelations affecting the statistical modelling of fMRI signals. With the

proposed white-noise filter, temporal autocorrelations were reduced and thus statistical inference effectively increased. It was shown that a significant reduction of false positive activations at any given threshold outweighs a slight decrease in the number of activated voxels. At a fixed significance level of 5 %, the number of activated voxels could be increased by a factor of up to 1.4 when the white-noise filter was used.

In conclusion, it was successfully shown that an EPI sequence with slice-dependent echo times yields superior statistical inference in the OFC compared to an optimized standard EPI sequence with a reduced echo time. With respect to BOLD spatial specificity on the single subject level, the 128 x 128 (R = 3) or the 160 x 160 (R = 3) EPI protocols might yield a good compromise between BOLD spatial specificity and sensitivity and should therefore be suitable for clinical applications such as preoperative planning and neuronavigation (Sunaert 2006; Vlieger, et al. 2004; Wurm, et al. 2008) ideally requiring both, high spatial specificity and sensitivity (Vlieger, et al. 2004). With focus on fMRI research studies targeting to make global inferences about groups of participants rather than single subjects, the presented fMRI results show for the first time that conventional matrix sizes (PI-factors) used in EPI at the clinical field strength of 3 T are non-optimal sacrificing spatial specificity. It may be recommend using the proposed 192 x 192 (R = 4) EPI protocol, which turned out to be applicable in detecting more robust BOLD activation on the group level with higher spatial specificity. Combining the proposed high-resolution EPI protocols with slice-dependent echo times could be used to increase both, spatial specificity and BOLD sensitivity. Using small echo times in the lower slices requires shorter signal read outs. The proposed 160 x 160 (R = 3) and the 192 x 192 (R = 4) EPI protocol use moderate bandwidths and no Partial Fourier technique. Thus, the read out duration could be easily adapted to shorter echo times by either increasing the bandwidths and/or by using Partial Fourier. Another strategy to improve BOLD sensitivity is to increase the *SNR* by adapting the proposed high-resolution protocols to a 3D EPI sequence. Combined with an optimized coil setup (e.g. 32-channel head coil) facilitating higher PI-accelerations, larger matrix sizes could be acquired to further increase spatial specificity. Moreover, it was successfully demonstrated that rapid fMRI at ultra-high spatial resolution is feasible using a segmented EPI sequence in combination with high UNFOLD acceleration allowing half-brain coverage with sufficient temporal resolution to detect BOLD activation in an event-related fMRI study. Last but not least, it was demonstrated that statistical inference using UNFOLD significantly improves with the suggested white-noise filtering strategy. Recently, the

Multiplexed-EPI sequence using multibanded simultaneous slice excitation (Feinberg, et al. 2010; Moeller, et al. 2010) has been suggested and is considered to be a promising approach for substantially increasing the image acquisition speed as it enables significantly higher acceleration rates compared to conventional methods. The Multiplexed EPI has been successfully tested in fMRI at 7 T reaching acceleration factors up to R = 36 enabling whole-brain acquisition within 400-800 ms at 2.5 mm isotropic resolution. However, the multiplexing strategy has not been combined with a high-resolution segmented EPI technique, yet. This novel approach could potentially revolutionize fMRI at sub-millimeter spatial resolution allowing rapid whole-brain acquisitions within 1-2 s.

Bibliography

Abragam A. 1961. Principles of Nuclear Magnetism: Oxford University Press, New York.

Afacan O, Hoge S, Brooks DH, Morocz IA. 2009. Increasing temporal resolution in hybrid 3D EPI fMRI studies using unfold. Biomedical Imaging: From Nano to Macro:654-657.

Aguirre GK, Zarahn E, D'Esposito M. 1997. Empirical analyses of BOLD fMRI statistics. II. Spatially smoothed data collected under null-hypothesis and experimental conditions. Neuroimage 5(3):199-212.

Aharon I, Becerra L, Chabris CF, Borsook D. 2006. Noxious heat induces fMRI activation in two anatomically distinct clusters within the nucleus accumbens. Neurosci Lett 392(3):159-64.

Amaro E, Jr., Barker GJ. 2006. Study design in fMRI: basic principles. Brain Cogn 60(3):220-32.

Barth M, Reichenbach JR, Venkatesan R, Moser E, Haacke EM. 1999. High-resolution, multiple gradient-echo functional MRI at 1.5 T. Magn Reson Imaging 17(3):321-9.

Benson RR, FitzGerald DB, LeSueur LL, Kennedy DN, Kwong KK, Buchbinder BR, Davis TL, Weisskoff RM, Talavage TM, Logan WJ and others. 1999. Language dominance determined by whole brain functional MRI in patients with brain lesions. Neurology 52(4):798-809.

Birn RM, Bandettini PA, Cox RW, Shaker R. 1999. Event-related fMRI of tasks involving brief motion. Hum Brain Mapp 7(2):106-14.

Blaimer M, Breuer F, Mueller M, Heidemann RM, Griswold MA, Jakob PM. 2004. SMASH, SENSE, PILS, GRAPPA: how to choose the optimal method. Top Magn Reson Imaging 15(4):223-36.

Blueml S, Schad LR, Stepanow B, Lorentz WJ. 1993. Spin-Lattice Relaxation Time Measurements by Means of a TurboFLASH Technique. Magn. Reson. Med. 30:289–295.

Boxerman JL, Bandettini PA, Kwong KK, Baker JR, Davis TL, Rosen BR, Weisskoff RM. 1995. The intravascular contribution to fMRI signal change: Monte Carlo modeling and diffusion-weighted studies in vivo. Magn Reson Med 34(1):4-10.

Bracewell RN. 1999. The Fourier Transform And Its Applications. McGraw-Hill, Third. Edition.

Braver TS, Barch DM, Gray JR, Molfese DL, Snyder A. 2001. Anterior cingulate cortex and response conflict: effects of frequency, inhibition and errors. Cereb Cortex 11(9):825-36.

Brockway JP. 2000. Two functional magnetic resonance imaging f(MRI) tasks that may replace the gold standard, Wada testing, for language lateralization while giving additional localization information. Brain Cogn 43(1-3):57-9.

Buchanan TW, Lutz K, Mirzazade S, Specht K, Shah NJ, Zilles K, Jancke L. 2000. Recognition of emotional prosody and verbal components of spoken language: an fMRI study. Brain Res Cogn Brain Res 9(3):227-38.

Buhler M, Vollstadt-Klein S, Kobiella A, Budde H, Reed LJ, Braus DF, Buchel C, Smolka MN. 2010. Nicotine dependence is characterized by disordered reward processing in a network driving motivation. Biol Psychiatry 67(8):745-52.

Bullmore E, Brammer M, Williams SC, Rabe-Hesketh S, Janot N, David A, Mellers J, Howard R, Sham P. 1996. Statistical methods of estimation and inference for functional MR image analysis. Magn Reson Med 35(2):261-77.

Butts K, Riederer SJ, Ehman RL, Thompson RM, Jack CR. 1994. Interleaved echo planar imaging on a standard MRI system. Magn Reson Med 31(1):67-72.

Buxton RB. 2002. Introduction to Functional Magnetic Resonance Imaging: Cambridge University Press.

Buxton RB, Uludag K, Dubowitz DJ, Liu TT. 2004. Modeling the hemodynamic response to brain activation. Neuroimage 23 Suppl 1:S220-33.

Buxton RB, Wong EC, Frank LR, Siewert B, Warach S, Edelman RR. 1998. Dynamics of blood flow and axygenation changes during brain activation: the balloon model. Magn. Reson. Med. 39:855-864.

Carlson JW. 1987. An algorithm for NMR imaging reconstruction based on multiple RF receiver coils. Journal of Magnetic Resonance 74:376-380.

Cho ZH, Ro YM. 1992. Reduction of susceptibility artifact in gradient-echo imaging. Magn. Reson. Med. 23:193-200.

Collins DL, Mills SR, Brown ED, Kelly RL, Peters TM. 1993. 3D statistical neuroanatomical models from 305 MRI volumes. IEEE Conference Record:1813-17.

Constable RT, Spencer DD. 1999. Composite image formation in z-shimmed functional MR imaging. Magn. Reson. Med. 42:110-117.

Cools R, Clark L, Owen AM, Robbins TW. 2002. Defining the neural mechanisms of probabilistic reversal learning using event-related functional magnetic resonance imaging. J Neurosci 22(11):4563-7.

Crinion J, Ashburner J, Leff A, Brett M, Price C, Friston K. 2007. Spatial normalization of lesioned brains: performance evaluation and impact on fMRI analyses. Neuroimage 37(3):866-75.

Czervionke LF, Daniels DL, Wehrli FW, Mark LP, Hendrix LE, Strandt JA. 1988. Magnetic susceptibility artifacts in gradient-recalled echo MR imaging. Am. J. Neuroradiol. 9:1149-1155.

D'Esposito M, Zarahn E, Aguirre GK. 1999. Event-related functional MRI: implications for cognitive psychology. Psychol Bull 125(1):155-64.

Davis KD, Kwan CL, Crawley AP, Mikulis DJ. 1998. Functional MRI study of thalamic and cortical activations evoked by cutaneous heat, cold, and tactile stimuli. J Neurophysiol 80(3):1533-46.

De Panfilis C, Schwarzbauer C. 2005. Positive or negative blips? The effect of phase encoding scheme on susceptibility-induced signal losses in EPI. Neuroimage 25(1):112-21.

de Zwart JA, Ledden PJ, van Gelderen P, Bodurka J, Chu R, Duyn JH. 2004. Signal-to-noise ratio and parallel imaging performance of a 16-channel receive-only brain coil array at 3.0 Tesla. Magn Reson Med 51(1):22-6.

de Zwart JA, Silva AC, van Gelderen P, Kellman P, Fukunaga M, Chu R, Koretsky AP, Frank JA, Duyn JH. 2005. Temporal dynamics of the BOLD fMRI impulse response. Neuroimage 24(3):667--677.

Deichmann R, Gottfried JA, Hutton C, Turner R. 2003. Optimized EPI for fMRI studies of the orbitofrontal cortex. Neuroimage 19:430-441.

Deichmann R, Josephs CH, Corfield C, D.R, Turner R. 2002. Compensation of Susceptibility-Induced BOLD Sensitivity Losses in Echo-Planar fMRI Imaging. Neuroimage 15:120-135.

Diekhof EK, Falkai P, Gruber O. 2008. Functional neuroimaging of reward processing and decision-making: a review of aberrant motivational and affective processing in addiction and mood disorders. Brain Res Rev 59(1):164-84.

Domsch S, Heiler PM, Schad LR. 2011. Event-related functional MRI at high spatial and temporal resolution using UNFOLD. Proc. Intl. Soc. Mag. Reson. Med. 19:p. 3580.

Domsch S, Lemke A, Weingartner S, Schad LR. 2012. A novel temporal filtering strategy for functional MRI using UNFOLD. Neuroimage 62(1):59-66.

Domsch S, Linke J, Heiler PM, Kroll A, Flor H, Wessa M, Schad LR. 2013. Increased BOLD sensitivity in the orbitofrontal cortex using slice-dependent echo times at 3 T. Magn Reson Imaging 31(2):201-11.

Duong TQ, Yacoub E, Adriany G, Hu X, Ugurbil K, Kim SG. 2003. Microvascular BOLD contribution at 4 and 7 T in the human brain: gradient-echo and spin-echo fMRI with suppression of blood effects. Magn Reson Med 49(6):1019-27.

Engel SA, Glover GH, Wandell BA. 1997. Retinotopic organization in human visual cortex and the spatial precision of functional MRI. Cereb Cortex 7(2):181-92.

Ernst RR, Anderson E-J. 1966. Application of fourier transform spectroscopy to magentic resonance. Reviews of Scientific Instruments 37(1):93-102.

Everitt BJ, Robbins TW. 2005. Neural systems of reinforcement for drug addiction: from actions to habits to compulsion. Nat Neurosci 8(11):1481-9.

Evers EA, Cools R, Clark L, van der Veen FM, Jolles J, Sahakian BJ, Robbins TW. 2005. Serotonergic modulation of prefrontal cortex during negative feedback in probabilistic reversal learning. Neuropsychopharmacology 30(6):1138-47.

Feinberg DA, Moeller S, Smith SM, Auerbach E, Ramanna S, Glasser MF, Miller KL, Ugurbil K, Yacoub E. 2010. Multiplexed echo planar imaging for sub-second whole brain FMRI and fast diffusion imaging. PLoS One 5(12):e15710.

Fellner C, Doenitz C, Finkenzeller T, Jung EM, Rennert J, Schlaier J. 2009. Improving the spatial accuracy in functional magnetic resonance imaging (fMRI) based on the blood oxygenation level dependent (BOLD) effect: benefits from parallel imaging and a 32-channel head array coil at 1.5 Tesla. Clin Hemorheol Microcirc 43(1-2):71-82.

Fera F, Yongbi MN, van Gelderen P, Frank JA, Mattay VS, Duyn JH. 2004. EPI-BOLD fMRI of human motor cortex at 1.5 T and 3.0 T: sensitivity dependence on echo time and acquisition bandwidth. J Magn Reson Imaging 19(1):19-26.

Fox PT, Raichle ME. 1986. Focal physiological uncoupling of cerebral blood flow and oxidative metabolism during somatosensory stimulation in human subjects. Proc Natl Acad Sci U S A 83(4):1140-4.

Frahm J, Krüger G, Merboldt KD, Kleinschmidt A. 1996. Dynamic uncupling and recoupling of perfusion and oxidative metabolism during focal brain activation in man. Magn. Reson. Med. 35:3143-148.

Frahm J, Merboldt KD, Hanicke W. 1993. Functional MRI of human brain activation at high spatial resolution. Magn Reson Med 29(1):139-44.

Frahm J, Merboldt KD, Hänicke W. 1988. Direct flash MR imaging of magnetic field imhomogeneities by gradient compensation. Magn. Reson. Med. 6:474-480.

Friston JK. 1996. Introduction - Experimental design and Statistical Parametric Mapping: The Wellcome Dept. of Cognitive Neurology, University College, London.

Friston KJ, Holmes AP, Poline JB, Grasby PJ, Williams SC, Frackowiak RS, Turner R. 1995. Analysis of fMRI time-series revisited. Neuroimage 2(1):45-53.

Friston KJ, Zarahn E, Josephs O, Henson RN, Dale AM. 1999. Stochastic designs in event-related fMRI. Neuroimage 10(5):607-19.

Gati JS, Menon RS, Ugurbil K, Rutt BK. 1997. Experimental determination of the BOLD field strength dependence in vessels and tissue. Magn Reson Med 38(2):296--302.

Gelman N, Gorell JM, Barker PB, Savage RM, Spickler EM, Windham JP, Knight RA. 1999. MR imaging of human brain at 3.0 T: preliminary report on transverse relaxation rates and relation to estimated iron content. Radiology 210(3):759-67.

Glover GH. 1999a. 3D Z-shim method for reduction of susceptibility effects in BOLD fMRI. Magn. Reson. Med. 42:290-299.

Glover GH. 1999b. Deconvolution of impulse response in event-related BOLD fMRI. Neuroimage 9(4):416-29.

Golay X, Pruessmann KP, Weiger M, Crelier GR, Folkers PJ, Kollias SS, Boesiger P. 2000. PRESTO-SENSE: an ultrafast whole-brain fMRI technique. Magn Reson Med 43(6):779-86.

Grill-Spector K, Knouf N, Kanwisher N. 2004. The fusiform face area subserves face perception, not generic within-category identification. Nat Neurosci 7(5):555-62.

Griswold MA, Jakob PM, Heidemann RM, Nittka M, Jellus V, Wang J, Kiefer B, Haase A. 2002. Generalized autocalibrating partially parallel acquisitions (GRAPPA). Magn Reson Med 47(6):1202-10.

Grubb RL, Jr., Raichle ME, Eichling JO, Ter-Pogossian MM. 1974. The effects of changes in PaCO2 on cerebral blood volume, blood flow, and vascular mean transit time. Stroke 5(5):630-9.

Haase A, Frahm J, Matthaei D, Haenicke W, Merboldt K-D. 1986. FLASH imaging, rapid NMR imaging using low flip-angle pulses. J. Magn. Reson., 67(2):258-266.

Hahn EL. 1950. Spin Echoes. Phys. Rev., 80:580–594.

Haken H, Wolf HC. 2003. Atom- und Quantenphysik: Springer, Berlin Heidelberg New York.

Heiler PM. 2011. ^{23}NA Chemical Shift Magnetic Resonance Imaging: T_2*-Relaxometry after Cerebral Stroke: Heidelberg University.

Heiler PM, Schmitter S, Schad LR. 2010. Artifact free T2*-weighted imaging at high spatial resolution using segmented EPI sequences. Z Med Phys 20(3):166-74.

Hoge RD, Atkinson J, Gill B, Crelier GR, Marrett S, Pike GB. 1999. Investigation of BOLD signal dependence on cerebral blood flow and oxygen consumption: The deoxyhemoglobin dilution model. Magnetic Resonance in Medicine 42(5):849-863.

Hoogenraad FG, Hofman MB, Pouwels PJ, Reichenbach JR, Rombouts SA, Haacke EM. 1999. Sub-millimeter fMRI at 1.5 Tesla: correlation of high resolution with low resolution measurements. J Magn Reson Imaging 9(3):475-82.

Hoogenraad FG, Pouwels PJ, Hofman MB, Rombouts SA, Lavini C, Leach MO, Haacke EM. 2000. High-resolution segmented EPI in a motor task fMRI study. Magn Reson Imaging 18(4):405-9.

Hu Y. 2011. Detrending phase drift: a preprocessing step to improve the effectiveness of the UNFOLD technique. J Magn Reson Imaging 33(3):742-7.

Hu Y, Glover GH. 2009. Increasing spatial coverage for high-resolution functional MRI. Magn Reson Med 61(3):716-22.

Hutchinson M, Raff U. 1988. Fast MRI data acquisition using multiple detectors. Magn Reson Med 6(1):87-91.

Hutton C, Bork A, Josephs O, Deichmann R, Ashburner J, Turner R. 2002. Image disstortion correction in fMRI: a quantitative evaluation. Neuroimage 16:217-240.

Ikemoto S, Panksepp J. 1999. The role of nucleus accumbens dopamine in motivated behavior: a unifying interpretation with special reference to reward-seeking. Brain Res Brain Res Rev 31(1):6-41.

Jezzard P, Balaban RS. 1995. Correction for geometric distortion in echo planar images from B0 field variations. Magn. Reson. Med. 34:65-73.

Jezzard P, Matthews PM, Smith SM. 2001. Functional MRI - an introduction to methods.: Oxford University Press.

Josephs O, Turner R, Friston K. 1997. Event-related f MRI. Hum Brain Mapp 5(4):243-8.

Kelton JR, Magin RL, Wright SM. 1989. An algorithm for rapid image acquisition using multiple receiver coils. Proceedings of the SMRM 8th Annual Meeting, Amsterdam:p.1172.

Kiehl KA, Liddle PF, Hopfinger JB. 2000. Error processing and the rostral anterior cingulate: an event-related fMRI study. Psychophysiology 37(2):216-23.

Kleinschmidt A, Nitschke MF, Frahm J. 1997. Somatotopy in the human motor cortex hand area. A high-resolution functional MRI study. Eur J Neurosci 9(10):2178-86.

Knutson B, Adams C, Fong G, Walker J, Hommer D. 2001. Parametric fMRI confirms selective recruitment of nucleus accumbens during anticipation of monetary reward. Neuroimage:430.

Konstandin S, Heiler PM, Scharf J, Schad LR. 2011. Comparison of selective arterial spin labeling using 1D and 2D tagging RF pulses. Z Med Phys 21(1):26-32.

Kroll A. 2004. Quantifizierung der Perfusion mit Arterial Spin-Labeling Techniken in der Magnetresonanz-Tomographie an Hand eines Perfusionsphantoms: Ruprecht-Karls-Universität Heidelberg.

Kruger G, A K, Gh G. 2001. Neuroimaging at 1.5 T and 3.0 T: comparison of oxygenation-sensitive magnetic resonance imaging. Magn. Reson. Med., 45:595-604.

Kruggel F, von Cramon DY. 1999a. Modeling the hemodynamic response in single-trial functional MRI experiments. Magn Reson Med 42(4):787-97.

Kruggel F, von Cramon DY. 1999b. Temporal properties of the hemodynamic response in functional MRI. Hum Brain Mapp 8(4):259-71.

Lauterbur PC. 1973. Image Formation by Induced Local Interactions: Examples Employing Nuclear Magnetic Resonance. Nature, 242:190-191.

Law CS, Glover GH. 2009. Interleaved spiral-in/out with application to functional MRI (fMRI). Magn Reson Med 62(3):829-34.

Linke J, Kirsch P, King AV, Gass A, Hennerici MG, Bongers A, Wessa M. 2010. Motivational orientation modulates the neural response to reward. Neuroimage 49(3):2618-25.

Lipschutz B, Friston KJ, Ashburner J, Turner R, Price CJ. 2001. Assessing study-specific regional variations in fMRI signal. Neuroimage 13(2):392-8.

Loubinoux I, Carel C, Alary F, Boulanouar K, Viallard G, Manelfe C, Rascol O, Celsis P, Chollet F. 2001. Within-session and between-session reproducibility of cerebral sensorimotor activation: a test--retest effect evidenced with functional magnetic resonance imaging. J Cereb Blood Flow Metab 21(5):592-607.

Madore B, Glover GH, Pelc NJ. 1999. Unaliasing by fourier-encoding the overlaps using the temporal dimension (UNFOLD), applied to cardiac imaging and fMRI. Magn Reson Med 42(5):813-28.

Malonek D, Dirnagl U, Lindauer U, Yamada K, Kanno I, Grinvald A. 1997. Vascular imprints of neuronal activity: relationships between the dynamics of cortical blood flow, oxygenation, and volume changes following sensory stimulation. Proc Natl Acad Sci U S A 94(26):14826-31.

Mansfield P. 1977. Multi-planar image formation using NMR spin echoes. Journal of Physics C: Solid State Physics 10:L55-L58.

Marchini JL, Ripley BD. 2000. A new statistical approach to detecting significant activation in functional MRI. Neuroimage 12(4):366-80.

Marota JJA, Mandeville JB, Weisskoff RM, Moskowitz MA, Rosen BR, Kosofsky BE. 2000. Cocaine activation discriminates dopaminergic projections by temporal responce: an fMRI study in Rat. Neuroimage 11:13-23.

Matthews PM, Jezzard P. 2004. Functional magnetic resonance imaging. J Neurol Neurosurg Psychiatry 75(1):6-12.

McKinnon GC. 1993. Ultrafast interleaved gradient-echo-planar imaging on a standard scanner. Magn Reson Med 30(5):609-16.

Moeller S, Van de Moortele PF, Goerke U, Adriany G, Ugurbil K. 2006. Application of parallel imaging to fMRI at 7 Tesla utilizing a high 1D reduction factor. Magn Reson Med 56(1):118-29.

Moeller S, Yacoub E, Olman CA, Auerbach E, Strupp J, Harel N, Ugurbil K. 2010. Multiband multislice GE-EPI at 7 tesla, with 16-fold acceleration using partial parallel imaging with application to high spatial and temporal whole-brain fMRI. Magn Reson Med 63(5):1144-53.

Morawetz C, Holz P, Lange C, Baudewig J, Weniger G, Irle E, Dechent P. 2008. Improved functional mapping of the human amygdala using a standard functional magnetic resonance imaging sequence with simple modifications. Magn Reson Imaging 26(1):45-53.

Muller JL, Roder CH, Schuierer G, Klein H. 2002. Motor-induced brain activation in cortical, subcortical and cerebellar regions in schizophrenic inpatients. A whole brain fMRI fingertapping study. Prog Neuropsychopharmacol Biol Psychiatry 26(3):421-6.

Nagel AM, Laun FB, Weber MA, Matthies C, Semmler W, Schad LR. 2009. Sodium MRI using a density-adapted 3D radial acquisition technique. Magn Reson Med 62(6):1565-73.

Newton AT, Rogers BP, Gore JC, Morgan VL. 2012. Improving measurement of functional connectivity through decreasing partial volume effects at 7 T. Neuroimage 59(3):2511-7.

Nielsen FA, Hansen LK. 2002. Automatic anatomical labelling of Talairach coordinates and generation of volumes of interest via BrainMap database. NeuroImage 16(2):Presented at the 8th International Conference on Functional Mapping of the Human Brain, June 2-6, 2002 Sendai, Japan, Available on CD-Rom.

Norris GD. 2006. Principles of Magnetic Resonance Assessment of Brain Function. J. Magn. Reson. Imaging, 23:794-807.

Ogawa S, Lee TM, Kay AR, Tank DW. 1990a. Brain magnetic resonance imaging with contrast dependent on blood oxygenation. Proc Natl Acad Sci U S A 87(24):9868-72.

Ogawa S, Lee TM, Nayak AS, Glynn P. 1990b. Oxygenation-sensitive contrast in magnetic resonance image of rodent brain at high magnetic fields. Magn Reson Med 14(1):68-78.

Ogawa S, Menon RS, Tank DW. 1993. Functional brain mapping by blood oxygenation level-dependent contrast magnetic-resonance-imaging - a comparison of signal characteristics with a biophysical model. Biophys. J. 64:803-812.

Olman CA, Inati S, Heeger DJ. 2007. The effect of large veins on spatial localization with GE BOLD at 3 T: Displacement, not blurring. Neuroimage 34(3):1126-35.

Ordridge RJ, Gorell JM, Deniau JC, Knight RA, Helpern JA. 1994. Assessment of relative brain iron concentration using T2-weighted and T2*-weighted MRI at 3 Tesla. Magn. Reson. Med. 32:335-341

Parrish TB, Gitelman DR, LaBar KS, Mesulam MM. 2000. Impact of signal-to-noise on functional MRI. Magn Reson Med 44(6):925-32.

Pauling L, Coryell CD. 1936. The Magnetic Properties and Structure of Hemoglobin, Oxyhemoglobin and Carbonmonoxyhemoglobin. Proc. Natl. Acad. Sci. USA 22(4):210-6.

Peters AM, Brookes MJ, Hoogenraad FG, Gowland PA, Francis ST, Morris PG, Bowtell R. 2007. T2* measurements in human brain at 1.5, 3 and 7 T. Magn Reson. Imaging 25:748-753.

Poser BA, Norris DG. 2009. Investigating the benefits of multi-echo EPI for fMRI at 7 T. Neuroimage 45(4):1162-72.

Poser BA, Versluis MJ, Hoogduin JM, Norris DG. 2006. BOLD contrast sensitivity enhancement and artifact reduction with multiecho EPI: parallel-acquired inhomogeneity-desensitized fMRI. Magn Reson Med 55(6):1227-35.

Posse S, Wiese S, Gembris D, Mathiak K, Kessler C, Grosse-Ruyken ML, Elghahwagi B, Richards T, Dager SR, Kiselev VG. 1999. Enhancement of BOLD-contrast sensitivity by single-shot multi-echo functional MR imaging. Magn Reson Med 42(1):87-97.

Preibisch C, Pilatus U, Bunke J, Hoogenraad F, Zanella F, Lanfermann H. 2003. Functional MRI using sensitivity-encoded echo planar imaging (SENSE-EPI). Neuroimage 19(2 Pt 1):412-21.

Preibisch C, Wallenhorst T, Heidemann R, Zanella FE, Lanfermann H. 2008. Comparison of parallel acquisition techniques generalized autocalibrating partially parallel acquisitions (GRAPPA) and modified sensitivity encoding (mSENSE) in functional MRI (fMRI) at 3T. J Magn Reson Imaging 27(3):590-8.

Preston AR, Thomas ME, Ochsner KN, Cooper JC, Glover GH. 2004. Comparison of spiral-in/out and spiral-out BOLD fMRI at 1.5 and 3 T. Neuroimage 21:291-301.

Pruessmann KP, Weiger M, Scheidegger MB, Boesiger P. 1999. SENSE: sensitivity encoding for fast MRI. Magn Reson Med 42(5):952-62.

Purdon PL, Weisskoff RM. 1998. Effect of temporal autocorrelation due to physiological noise and stimulus paradigm on voxel-level false-positive rates in fMRI. Hum Brain Mapp 6(4):239-49.

Ramsey NF, Hoogduin H, Jansma JM. 2002. Functional MRI experiments: acquisition, analysis and interpretation of data. Eur Neuropsychopharmacol 12(6):517-26.

Riedel E. 2004. Anorganische Chemie. De Gruyter.

Robitaille P-M, Berliner L. 2006. Ultra High Field Magnetic Resonance Imaging. Springer-Verlag.

Roemer PB, Edelstein WA, Hayes CE, Souza SP, Mueller OM. 1990. The NMR phased array. Magn Reson Med 16(2):192-225.

Rosen BR, Buckner RL, Dale AM. 1998. Event-related functional MRI: past, present, and future. Proc Natl Acad Sci U S A 95(3):773-80.

Schacter DL, Buckner RL, Koutstaal W, Dale AM, Rosen BR. 1997. Late onset of anterior prefrontal activity during true and false recognition: an event-related fMRI study. Neuroimage 6(4):259-69.

Schmitter S. 2008. Entwicklung von geräuscharmen Bildgebungstechniken für die funktionelle Magnetresonanztomographie: Ruprecht-Karls-Universität Heidelberg.

Schweizer R, Voit D, Frahm J. 2008. Finger representations in human primary somatosensory cortex as revealed by high-resolution functional MRI of tactile stimulation. Neuroimage 42(1):28-35.

Seber G. 1977. Linear Regression analysis. Wiley, New York.

Shmuel A, Yacoub E, Chaimow D, Logothetis NK, Ugurbil K. 2007. Spatio-temporal point-spread function of fMRI signal in human gray matter at 7 Tesla. Neuroimage 35(2):539-52.

Smith AT, Singh KD, Balsters JH. 2007. A comment on the severity of the effects of non-white noise in fMRI time-series. Neuroimage 36(2):282-8.

Sodickson DK, Griswold MA, Jakob PM, Edelman RR, Manning WJ. 1999. Signal-to-noise ratio and signal-to-noise efficiency in SMASH imaging. Magn Reson Med 41(5):1009-22.

Sodickson DK, Manning WJ. 1997. Simultaneous acquisition of spatial harmonics (SMASH): fast imaging with radiofrequency coil arrays. Magn Reson Med 38(4):591-603.

Speck O, Hennig J. 1998. Functional imaging by I0- and T2*-parameter mapping using multi-image EPI. Magn Reson Med 40(2):243-8.

Speck O, Stadler J, Zaitsev M. 2008. High resolution single-shot EPI at 7T. MAGMA 21(1-2):73-86.

Stenger VA, Boada FE, Noll DC. 2000. Three-dimensional tailored RF pulses for the reduction of susceptibility artifacts in T2*-weighted Functional MRI. Magn. Reson. Med. 44:525-531.

Stocker T, Kellermann T, Schneider F, Habel U, Amunts K, Pieperhoff P, Zilles K, Shah NJ. 2006. Dependence of amygdala activation on echo time: results from olfactory fMRI experiments. Neuroimage 30(1):151-9.

Sunaert S. 2006. Presurgical planning for tumor resectioning. J Magn Reson Imaging 23(6):887-905.

Tabelow K, Piech V, Polzehl J, Voss HU. 2009. High-resolution fMRI: overcoming the signal-to-noise problem. J Neurosci Methods 178(2):357-65.

Talairach J, Tournoux P. 1988. Co-planar stereotaxic atlas of the human brain. Thieme, New York.

TheMathWorksInc. 2008. Stastistical Parameter Mapping.

Thews G, editor. 1997. "Atemgastransport und Säure-Basen-Status des Blutes". In: Schmidt, R.F., Thews, G. (publisher), "Physiologie des Menschen", Vol. 27, p. 604-622, Springer-Verlag, Berlin, 1997.

Thulborn KR, Brady TJ. 1989. Iron in magnetic resonance imaging of cerebral hemorrhage. Magn Reson Q 5(1):23-38.

Triantafyllou C, Hoge RD, Wald LL. 2006. Effect of spatial smoothing on physiological noise in high-resolution fMRI. Neuroimage 32(2):551-7.

Villringer A, Dirnagl U. 1995. Coupling of brain activity and cerebral blood flow: basis of functional neuroimaging. Cerebrovasc Brain Metab Rev 7(3):240-76.

Vlieger EJ, Majoie CB, Leenstra S, Den Heeten GJ. 2004. Functional magnetic resonance imaging for neurosurgical planning in neurooncology. Eur. Radiol. 14:1143-1153.

Voit D, Frahm J. 2005. Echo train shifted multi-echo FLASH for functional MRI of the human brain at ultra-high spatial resolution. NMR Biomed 18(8):481-8.

Vollstadt-Klein S, Wichert S, Rabinstein J, Buhler M, Klein O, Ende G, Hermann D, Mann K. 2010. Initial, habitual and compulsive alcohol use is characterized by a shift of cue processing from ventral to dorsal striatum. Addiction 105(10):1741-9.

Weiskopf N, Hotton C, Josephs O, Turner R, Deichmann R. 2007. Optimized EPI for fMRI studies of the orbitofrontal cortex: compensation of susceptibility-induced gradients in the readout direction. Magn. Reson. Mater. Phy. 20:39-49.

Weiskopf N, Klose U, Birbaumer N, Mathiak K. 2005. Single-shot compensation of image distortions and BOLD contrast optimization using multi-echo EPI for real-time fMRI. Neuroimage 24(4):1068-79.

Williams LM, Phillips ML, Brammer MJ, Skerrett D, Lagopoulos J, Rennie C, Bahramali H, Olivieri G, David AS, Peduto A and others. 2001. Arousal dissociates amygdala and hippocampal fear responses: evidence from simultaneous fMRI and skin conductance recording. Neuroimage 14(5):1070-9.

Windischberger C, Robinson S, Rauscher A, Barth M, Moser E. 2004. Robust field map generation using a triple-echo acquisition. J. Magn. Reson. Imaging 20:730-734.

Woolrich MW, Ripley BD, Brady M, Smith SM. 2001. Temporal autocorrelation in univariate linear modeling of FMRI data. Neuroimage 14(6):1370-86.

Worsley KJ, Friston KJ. 1995. Analysis of fMRI time-series revisited--again. Neuroimage 2(3):173-81.

Wurm G, Schnizer M, Fellner C. 2008. The impact of fMRI on multimodal navigation in surgery of cerebral lesions: four years of clinical experience. Int. J. CARS 3:191-199.

Xiang QS, Ye FQ. 2007. Correction for geometric distortion and N/2 ghosting in EPI by phase labeling for additional coordinate encoding (PLACE). Magn Reson Med 57(4):731-41.

Yacoub E, Duong TQ, Van De Moortele PF, Lindquist M, Adriany G, Kim SG, Ugurbil K, Hu X. 2003. Spin-echo fMRI in humans using high spatial resolutions and high magnetic fields. Magn Reson Med 49(4):655-64.

Zahm DS. 1999. Functional-anatomical implications of the nucleus accumbens core and shell subterritories. Ann N Y Acad Sci 877:113-28.

Zarahn E, Aguirre GK, D'Esposito M. 1997. Empirical analyses of BOLD fMRI statistics. I. Spatially unsmoothed data collected under null-hypothesis conditions. Neuroimage 5(3):179-97.

Danksagung

An dieser Stelle möchte ich mich bei allen bedanken, die zum Gelingen dieser Arbeit beigetragen haben. Mein besonderer Dank gilt:

- Lothar Schad, der mir die Durchführung dieser Arbeit in seiner Arbeitsgruppe ermöglicht hat. Ausserdem bedanke ich mich für seine uneingeschränkte Unterstützung während der gesamten Arbeit und die Vermittlung zahlreicher interessanter Projekte.
- Wolfgang Schlegel für die Begutachtung dieser Arbeit.
- Jascha Zapp, Andreas Lemke, Patrick Heiler und Sebastian Weingärtner für fruchtbare Diskussionen und die exzellente Zusammenarbeit.
- Dieter Kleinböhl, Julia Linke, Alexander Kroll, Herta Flor, Michèle Wessa, Fraue Nees, Holger Hill, Derik Herrmann, Karl Mann, Michael Rieß, Damian Karl, die die experimentelle Anwendung in diversen Projekten ermöglicht haben.
- Frank Zölner für die schnelle Hilfe bei sämtlichen Computerproblemen.
- Michaela Ruttorf, Domimique Corteville und Sabine Vollstädt-Klein für das Korrekturlesen dieser Arbeit und die vielen konstruktiven Gespräche, die mir wichtige Ideen geliefert haben.
- Allen Teilnehmern lang andauernder fMRT Studien.
- Raffi Kalayciyan, Asmund Kjorstad, Moritz Mie, Friedrich Wetterling, Sebastian Baier, Philipp Krämer, Melanie Heilmann, Julia Serwane, Simon Konstandin, Mathias Davids, Nadja Meßner und dem gesamten CKM Team für interessante Gespräche und eine angenehme Büroatmosphäre.

Vielen Dank!

Erklärung

Ich erkläre hiermit, dass ich die vorgelegte Dissertation selbst verfasst und mich dabei keiner anderen als den von mir ausdrücklich bezeichneten Quellen und Hilfen bedient habe.

Mannheim, den 26. März 2013

.....

(Sebastian Domsch)